

**ANALYZING THE EFFECT OF ENERGY DISSIPATION ON THERMO-
MECHANICAL RESPONSES OF VISCOELASTIC FIBER REINFORCED
COMPOSITE USING FINITE ELEMENT METHOD**

A Thesis

by

MAXIMILIAN D. LY

Submitted to the Office of Graduate and Professional Studies of
Texas A&M University
in partial fulfillment of the requirements for the degree of

MASTER OF SCIENCE

Chair of Committee,
Committee Members,

Head of Department,

Anastasia Muliana
Miladin Radovic
Philip Park
Andreas Polycarpou

May 2017

Major Subject: Mechanical Engineering

Copyright 2017 Maximilian D. Ly

ABSTRACT

Carbon fiber reinforced composites (CFRCs) are preferred materials used in the aerospace industry for high performance load bearing applications. The polymer matrix in CFRC is a viscoelastic material and its mechanical properties vary with time, temperature and applied external loads. Experimental work suggests that CFRCs, subjected to high-frequency cyclic loading, generate enormous amount of heat from the energy dissipation which softens the polymer and accelerates failure. Current research efforts on cyclic response in CFRP focus on understanding macroscopic (overall) performance of composites, i.e., number of cycle to failure for a given frequency and loading amplitude. A systematic understanding on the formation of heat generation and its effect on the mechanical properties of the constituents in composites, and microscopic responses of composite is currently lacking. Changes in the micromechanical field variables (strain, stress, temperature) of CFRCs during cyclic loading can be crucial in understanding failure in composites. This study attempts to provide a detailed understanding on the effect of energy dissipation due to the viscoelastic nature of polymer on the overall mechanical responses of CFRP composites subjected to cyclic loading. Finite element (FE) analyses on the deformations of CFRP composites under various boundary conditions and loading histories are presented. A thermo-mechanical viscoelastic constitutive model is used for the polymer which is defined using a material subroutine, developed by K. Khan and A. Muliana. The material subroutine is implemented in ABAQUS FE code. In addition, voids are added to the CFRC models to account for manufacturing imperfections and their influence on the field variables and macroscopic behaviors are investigated.

ACKNOWLEDGEMENTS

I would like to thank my advisor Dr. Muliana for her guidance and encouragement to successfully complete my research. In addition, I would like to thank my committee members, Dr. Park and Dr. Radovic for taking the time to serve on my committee and kindly supporting my research.

In addition, I would like to thank Dr. Khan for allowing me to use his finite element material subroutine code. Without his prior research and hard work, my research would have not been possible. I appreciate the time you took to guide me through the code and patiently answering all my questions. While his name is not listed on the title page, I would like to acknowledge his role as a committee member by special appointment.

I will also need to acknowledge the great contribution by the staff at Texas A&M University High Performance Research Computing for allowing me to use the computational resources available to conduct this research.

While not directly involved with the research, I will give thanks to Dr. William S. Klug, my undergraduate advisor at UCLA, for encouraging me to pursue graduate school and getting me interested in solid mechanics. He was a kind and supportive advisor who passed away at the age of 39.

At last, I would like to thank my parents and my two siblings, Susanna and Ina for supporting me through these two years of graduate school. I am eternally grateful for your support and love you all. This is for you.

CONTRIBUTORS AND FUNDING SOURCES

Contributors

This thesis was supported by a thesis committee consisting of my advisor Professor A. Muliana. In addition, the committee members were Professor P. Park of the Civil Engineering Department and Professor M. Radovic of the Material Science Department. All supervised my thesis work and peer reviewed it.

Professor K. Khan contributed to the research by previously developing the ABAQUS material subroutine that was used for the research. Furthermore he peer-reviewed my work extensively.

The work for the thesis was completed by student, under the advisement of Professor Muliana of the Department of Mechanical Engineering.

Funding Sources

Graduate study was supported by a Graduate Teaching Assistant appointment from Texas A&M University, Department of Mechanical Engineering.

TABLE OF CONTENTS

	Page
ABSTRACT	ii
ACKNOWLEDGEMENTS	iii
CONTRIBUTORS AND FUNDING SOURCES.....	iv
TABLE OF CONTENTS	v
LIST OF FIGURES.....	vii
LIST OF TABLES	xii
1 INTRODUCTION.....	1
1.1 Motivation and Research Objective	6
2 CONSTITUTIVE EQUATIONS	8
2.1 Viscoelastic Material ABAQUS Subroutine.....	8
3 MODEL CREATION – MATERIAL PROPERTIES – LOAD CASES.....	13
3.1 3D Finite Element Creation.....	13
3.2 Material Properties	15
3.3 3D Finite Element Load Case	18
3.4 Convergence Study	22
4 LONGITUDINAL LOADING – HOMOGENIZED VS. MICROSTRUCTURAL RESPONSE.....	26
5 THE EFFECT OF CYCLIC FREQUENCY ON POLYMER SOFTENING.....	38
6 THE EFFECT OF LOADING DIRECTION ON TEMPERATURE CHANGE (PRISTINE MODELS)	46
6.1 Shear Loading of Pristine Fiber Volume Models.....	46
6.2 Transverse Loading of Pristine Composite Models	58

	Page
7 THE EFFECT OF VOIDS ON MATRIX DEFORMATION AND TEMPERATURE CHANGE	68
7.1 Longitudinal Loading of Void Fiber Configuration Models	68
7.2 Shear Loading of Void Fiber Configuration Samples	79
7.3 Transverse Loading of Void Fiber Models	91
8 SUMMARY AND CONCLUSION	102
REFERENCES	106
APPENDIX A	110
APPENDIX B	147

LIST OF FIGURES

	Page
Figure 1 Finite Element Model with Voids.....	14
Figure 2 Coordinate System Front View.....	18
Figure 3 Coordinate System Back View	19
Figure 4 Stiffness vs. Mesh Density - Convergence Study	25
Figure 5 40% Fiber Volume - Homogenized Hysteresis Response	26
Figure 6 50% Fiber Volume - Homogenized Hysteresis Response	27
Figure 7 60% Fiber Volume - Homogenized Hysteresis Response	27
Figure 8 40% Fiber Volume – Longitudinal Loading – 3/60 Hz – Max Principal Strain -1.9 minutes.....	29
Figure 9 40% Fiber Volume - Longitudinal - 3/60 Hz - Max Principal Strain	29
Figure 10 40% Fiber Volume – Longitudinal Loading- Hysteresis – Fiber/Matrix	30
Figure 11 Principal Strain a) 50% Fiber Volume – 0.4 minutes b) 60% Fiber Volume – 19.9 minutes.....	31
Figure 12 Hysteresis Response a) 50% Fiber Volume b) 60% Fiber Volume.....	31
Figure 13 50% Fiber Volume - 2/60 Hz - 0.02 Disp. - Max Principal Strain – 20 minutes.....	33
Figure 14 50% Fiber Volume Principal Strain a) Matrix 1 Location b) Matrix 2 Location	34
Figure 15 Longitudinal Loading Temperature Change a) 40% Fiber b) 50% Fiber c) 60% Fiber.....	35
Figure 16 60% Fiber Volume - Temperature - Displacement Boundary Comparison	36
Figure 17 Max Principal Strain vs. Temperature - Longitudinal Loading – 2/60 Hz - a) 40% Fiber Volume b) 50% Fiber Volume c) 60% Fiber Volume.....	37
Figure 18 40% Fiber Volume - Frequency Model	38
Figure 19 40% Fiber Volume – 5/60 Hz – Max Principal Strain – 6.4 minutes	39

	Page
Figure 20 40% Fiber Volume – 5/60 Hz - Max Principal Strain – a) Fiber/Matrix b) Matrix	40
Figure 21 40% Fiber Volume – 5/60 Hz - Hysteresis – a) Fiber/Matrix b) Matrix	41
Figure 22 40% Fiber Volume – 10/60 Hz – Max Principal Strain – 6.85 minutes	42
Figure 23 40% Fiber Volume – 10/60 Hz - Max Principal Strain – a) Matrix/Fiber b) Matrix	42
Figure 24 40% Fiber Volume - 10/60 Hz - Hysteresis – Matrix.....	43
Figure 25 40% Fiber Volume - Frequency Study – Temperature	44
Figure 26 40% Fiber Volume - Max Principal Strain vs. Temperature - a) 5/60 Hz b) 10/60 Hz.....	45
Figure 27 40% Fiber Volume - Pristine - Shear Loading - Max Principal Stress - 3.5 minutes.....	47
Figure 28 40% Fiber Volume - Pristine - Shear Loading - Max Principal Strain a) Matrix/Fiber b) Matrix 1 c) Matrix 2.....	48
Figure 29 40% Fiber Volume - Pristine - Shear Loading – Hysteresis	49
Figure 30 50% Fiber Volume - Pristine - Shear Loading - Max Principal Strains a) Matrix 1 b) Matrix/Fiber c) Matrix 2.....	51
Figure 31 50% Fiber Volume - Pristine - Shear Loading - Hysteresis a) Matrix/Fiber b) Matrix 1 c) Matrix 2	52
Figure 32 60% Fiber Volume - Pristine - Shear Loading - Max Principal Strains a) Matrix 1 b) Matrix 2 c) Matrix/Fiber.....	53
Figure 33 60% Fiber Volume - Pristine - Shear Loading – Hysteresis a) Matrix 1 b) Matrix 2 c) Matrix/Fiber	54
Figure 34 Pristine - Shear Loading – Temperature	55
Figure 35 Max Principal Strain vs. Temperature – Shear Loading – Pristine - a) 40% Fiber Volume – Matrix/Fiber b) 40% Fiber Volume – Matrix 2 c) 50% Fiber Volume – Matrix/Fiber d) 50% Fiber Volume – Matrix 2 e) 60% Fiber Volume Matrix/Fiber f) 60% Fiber Volume – Matrix 2	56

	Page
Figure 36 40% Fiber Volume - Pristine - Material Orientation	58
Figure 37 40% Fiber Volume - Transverse – Maximum Principal Strain - 1.1 minute...	59
Figure 38 40% Fiber Volume - Transverse - Max Principal Strain – Matrix	60
Figure 39 40% Fiber Volume - Transverse - Max Principal Strain a) Matrix/Fiber 1 b) Matrix/Fiber 2.....	60
Figure 40 50% Fiber Volume - Pristine - Transverse - Principal Strain	61
Figure 41 50% Fiber Volume - Pristine - Transverse Loading - Max Principal Strain - Matrix/Fiber.....	61
Figure 42 60% Fiber Volume - Pristine - Transverse Loading - Max Principal Strain - Matrix/Fiber 1.....	62
Figure 43 Pristine Configurations - Transverse - Hysteresis Plots a) 40% Fiber Volume b) 50% Fiber Volume c) 60% Fiber Volume.....	63
Figure 44 Pristine Configurations - Transverse Loading – Temperature.....	65
Figure 45 Max Principal Strain vs. Temperature – Transverse Loading – Pristine - a) 40% Fiber Volume Matrix/Fiber 2 b) 40% Fiber Volume Matrix c) 50% Fiber Volume Matrix/Fiber d) 50% Fiber Volume Matrix e) 60% Fiber Volume Matrix/Fiber 2	66
Figure 46 40% Fiber Volume - Longitudinal - Max Principal Stress – 0.400 minutes ...	69
Figure 47 40% Fiber Volume - Longitudinal - Max Principal Strain a) Matrix/Fiber b) Matrix/Void and	70
Figure 48 40% Fiber Volume - Longitudinal - Hysteresis a) Matrix/Void b) Matrix/Edge	70
Figure 49 40% Fiber Volume - Longitudinal - Hysteresis – Matrix/Fiber	71
Figure 50 50% Fiber Volume – Void – Longitudinal -2/60 Hz- 20 minutes - Max Principal Strain	72
Figure 51 50% Fiber Volume - Void- Longitudinal- Principal Strain a) Matrix/Void b) Matrix	72

	Page
Figure 52 60% Fiber Volume - Void – Longitudinal Loading - Principal Strain - 18.9 minutes.....	73
Figure 53 60% Fiber Volume - Void - Longitudinal - Max Principal Strain a) Matrix/Fiber b) Matrix/Void.....	75
Figure 54 60% Fiber Volume - Void - Longitudinal - Hysteresis a) Matrix/Fiber b) Matrix/Void	75
Figure 55 Void Models - Longitudinal – Temperature	76
Figure 56 Max Principal Strain vs. Temperature – Longitudinal Loading – Void - a) 40% Fiber Volume Matrix/Fiber b) 40% Fiber Volume Matrix/Void c) 50% Fiber Volume Matrix/Fiber d) 50% Fiber Volume Matrix/Void e) 60% Fiber Volume Matrix/Fiber f) 60% Fiber Volume Matrix/Void	77
Figure 57 50% Fiber Volume - Void - Shear Loading - Max Principal Strain - 14.50 Minutes	79
Figure 58 50% Fiber Volume - Void - Shear - Max Principal Strain – a) Matrix/Void b) Matrix/Fiber.....	80
Figure 59 50% Fiber Volume - Void - Shear - Hysteresis – a) Matrix/Fiber b) Matrix/Void	81
Figure 60 40% Fiber Volume - Void - Shear - Principal Strain a) Matrix/Fiber b) Matrix/Void c) Matrix	82
Figure 61 40% Fiber Volume - Void - Shear - Shear Hysteresis - Matrix/Fiber	83
Figure 62 40% Fiber Volume - Void - Shear - Hysteresis - a) Matrix/Fiber b) Matrix/Void c) Matrix	84
Figure 63 60% Fiber Volume - Void - Shear Loading - Max Principal Stress - 3 minutes.....	85
Figure 64 60% Fiber Volume - Void - Shear Loading - Principal Strain a) Matrix/Void b) Matrix/Fiber c) Matrix.....	86
Figure 65 60% Fiber Volume - Void - Shear Loading a) Matrix/Void b) Matrix/Fiber c) Matrix	87
Figure 66 Void Models - Shear Loading – Temperature	88

	Page
Figure 67 Max Principal Strain vs. Temperature – Shear Loading – Void - a) 40% Fiber Volume Matrix/Fiber b) 40% Fiber Volume Matrix/Void c) 50% Fiber Volume Matrix/Fiber d) 50% Fiber Volume Matrix-Void e) 60% Fiber Volume Matrix/Fiber f) 60% Fiber Volume Matrix/Void	89
Figure 68 40% Fiber Volume - Void – Transverse	91
Figure 69 40% Fiber Volume - Void - Transverse - Max Principal Strain - 29.3 minutes.....	92
Figure 70 40% Fiber Volume - Void - Transverse - Max Principal Strain a) Matrix/Fiber b) Matrix/Void.....	92
Figure 71 40% Fiber Volume - Void - Transverse – Shear Hysteresis a) Matrix/Fiber b) Matrix/Void.....	93
Figure 72 40% Fiber Volume - Void - Transverse – Hysteresis a) Matrix/Fiber b) Matrix/Void	94
Figure 73 50% Fiber Volume - Void - Transverse Loading - Max Principal Strain – a) Matrix/Fiber b) Matrix/Void	95
Figure 74 50% Fiber Volume - Void - Transverse Loading - y-direction Hysteresis a) Matrix/Fiber b) Matrix/Void	96
Figure 75 60% Fiber Volume - Void - Transverse - Max Principal Strain - a) Matrix/Fiber b) Matrix/Void.....	97
Figure 76 60% Fiber Volume - Void - Transverse – Hysteresis a) Matrix/Fiber b) Matrix/Void	98
Figure 77 Void - Transverse Loading – Temperature	98
Figure 78 Max Principal Strain vs. Temperature – Transverse Loading – Void a) 40% Fiber Volume Matrix/Fiber b) 40% Fiber Volume Matrix/Fiber c) 50% Fiber Volume Matrix/Fiber d) 50% Fiber Volume Matrix/Void e) 60% Fiber Volume Matrix/Fiber f) 60% Fiber Volume Matrix/Void	100

LIST OF TABLES

	Page
Table 1 Void Geometry Parameters	14
Table 2 AS4 Carbon Fiber Properties	16
Table 3 FM73 Material Properties	17
Table 4 Convergence Study - Mesh Configuration.....	22
Table 5 Convergence Study - Effective Stiffness	24
Table 6 Max/Min Stress - Homogenized Response	28
Table 7 Hysteresis Response - 50% Fiber Volume - 60% Fiber Volume.....	32
Table 8 Max Principal Strain vs. Temperature - Pristine Models - Shear Loading	57
Table 9 Pristine Fiber Models - Transverse Loading - Hysteresis Stresses and Strains	63
Table 10 Max Principal Strain vs. Temperature - Pristine - Transverse Loading.....	67
Table 11 Max Principal Strain vs. Temperature - Void - Longitudinal Loading	78
Table 12 Max Principal Strain vs. Temperature - Void - Shear Loading	90
Table 13 Max Principal Strain vs. Temperature - Void - Transverse Loading.....	101

1 INTRODUCTION

Carbon fiber reinforced composites (CFRC) are becoming the preferred structural material in the aerospace/defense industry as lightweight alternative to traditional metals like aluminums. For load-bearing structures such as wings, fatigue is a primary failure mechanism when the structure is subjected to millions of loading cycles during the aircraft/spacecraft's lifecycle. CFRC are complex to analyze because its mechanical and thermal properties are orthotropic and vary significantly with respect to spatial location. As an example, large stress and strain gradients exist within the composite and the polymer matrix' mechanical properties, commonly used in CFRCs, are sensitive to the local temperature. To reduce complexity in structural analysis, design engineers and structural analysts treat CFRCs as a homogenized medium. However, in contrast to metal failure, which is well understood and has been extensively analyzed, the failure and fatigue damage is complex and CFRC's failure mechanisms include fiber-matrix debondings, fiber fracture, matrix cracking, to ply delamination. The initiation of failure occurs at the micromechanical level and cannot be accurately described using homogenization principles. To design more efficient load carrying structures for the aerospace, automobile and naval industry, one has to understand the failure mechanisms of CFRC. In order to observe and to understand these failure mechanisms, it is necessary to investigate the micromechanical field variables because failure initiates on the micromechanical level.

Understanding the mechanical properties, i.e. elastic modulus, of composites has been extensively researched. In the field of micromechanics, Eshelby [1] proposes the average field theory by assuming the strain of an ellipsoidal particle within a composite material is constant. Using the average field theory, one can determine the average stress and strain of a unit cell and determine the homogenized mechanical response of a heterogeneous material. Hashin [2] utilizes the self-consistent method to determine the effective bulk and shear moduli of a composite with spherical inclusions. The average field theory and the self-consistent method allow us to find exact analytical solutions in

determining the mechanical response of a heterogeneous materials. Advancing from determining the compliance and modulus of a composite, the prediction of crack onset in fiber reinforced composite has also been researched both experimentally and analytically. Stinchomb and Reifsnider [3] review experimental composite fatigue work and highlight that crack initiation in the matrix can occur during the first load cycle. They suggest that the anisotropy of thermal expansion coefficients can create thermal residual stresses during the curing process which would induce initial cracks in weaker plies. Highsmith and Reifsnider [4] tested $[0_m^\circ/90_n^\circ]$ scotchply reinforced plastics and correlated the reduction of the stiffness tensor to the transverse direction crack density. Using the variational method, Hashin [5] derived an analytical approach to predict crack onset and stiffness reduction in $[0_m^\circ/90_n^\circ]$ glass fiber composites. Hashin and Vinogradov [6] expanded the variational approach to include angled cracks in $[0_m^\circ/90_n^\circ]$ glass fiber composites. Both approaches were verified with experimental data and predicted stiffness reduction agreed well with the data. However, Hashin's and Vinogradov's approaches assumed perfect bonding between fiber/matrix interface, the absence of voids and manufacturing flaws and neglected temperature effects. According to Talreja [7], D. Krajcinovic advanced the field of Continuum Damage Mechanics (CDM) by advocating for the introduction of internal variables [8]. The field of Continuum Damage Mechanics assumes that a homogenized continua contains voids and cracks which constitute the damage to the media. The "damage" can be described by internal state variables which contain information of measurable quantities such as crack density and residual stiffness. However, the limitations of Hashin's and Vinogradov's variational methods are that it considers simple geometry and cannot account for manufacturing defects in the form of voids. Furthermore, CDM uses a homogenization approach and therefore does not observe the actual micromechanical behavior of the structure. To address the shortcomings of homogenization principles and average field theory, the method of cells (MOC) and its extension, the generalized method of cells (GMC), use repeating unit cells (RUCs) to determine the microstructural properties of a composite [9]. A RUC represents the composite's microstructure and can be divided into subsections to account for

fiber/particle and matrix. The GMC uses RUC and imposes traction and displacement continuity conditions to solve the boundary problems. The advantage of GMC is that it allows the researcher to study the microstructural properties such as interface stresses and strains in greater details. Furthermore, if the RUC is a representative volume element (RVE), i.e. it statistically represents the overall response of the whole composite, the homogenized composite properties can be extrapolated by using volume averages. The GMC relies on defining concentration tensors which relate local strain to global (homogenized) strain fields.

Regarding the fatigue performance of CFRCs, cyclic loading has shown that cyclic loading induces large temperature increases in the composite because the polymer is a viscoelastic material which dissipates energy during cyclic loading. It has been shown that energy dissipated by the hysteresis degrades the polymer's structural performance ([10], [11]). Rittel [12] studied the hysteretic dissipation behavior of polymethylmethacrylate (PMMA) and polycarbonate (PC) subjected to cyclic compressive loading. Maximum temperature changes of up to 70°C were observed after approximately 4000 cycles of loading and at strain amplitudes up to 0.45. Holmes and Chu [13] observed frictional heating of fiber-reinforced ceramics. They postulated that the energy dissipation and corresponding temperature increase was caused by fiber slippage along debonded interfaces. Temperature rises of 30 Kelvin were observed for cross-ply carbon fiber and silicon carbide composites cycled at 85 Hz with stress limits varying from 250 MPa to 10 MPa. Furthermore they suspected that the local temperature rise in the ceramic matrix may differ from the bulk temperature rise because of the low thermal conductivity of ceramic matrix. Toubal et al. [14] observed the damage evolution in a woven composite laminate using infrared thermography. The composite system tested was a composite fabric HR 285/G803 and epoxy resin. The tested specimens were plates and contained a hole at the center. The material was cyclic loaded at 10 Hz frequency and the maximum stress levels applied ranged from 102 to 119 MPa. The infrared thermography showed a temperature hotspot at the hole, suggesting that the inclusion of a hole influenced the dissipation behavior of the viscoelastic matrix. Of interest is that the rate of temperature change is not

constant and can be divided into three distinct regions. First, the temperature increases rapidly to a local maximum. Once the local maximum is reached, thermoelastic heating is dominant and the rate of temperature increase is lower than the initial rate of temperature change. The third region is again characterized by a large temperature increase until the composite fails due to fatigue. Laferie-Frenot et al. [10] investigated the detrimental temperature effects of brittle-matrix composite (carbon/epoxy T300/914) when subjected to both mechanical and thermo-mechanical cycles. They concluded that the thermal cycles were more damaging than pure mechanical fatigue cycles. Due to heating, the matrix softened which led to a loss in stiffness and faster matrix failure. Bellenger et al. [11] confirmed heat generation when they tested glass fiber/PA66 composite at 2 Hz and 10 Hz load frequency with a full load reversal cycles. Induced strains varied between 0.0116 and 0.0223. Surface temperatures increased up to 100°C after the samples were cycled at 10 Hz and maximum strain. Mivehchi and Varvani-Ferahni [15] developed a semi-empirical temperature dependent damage model for fiber reinforced composites under fatigue loading. The damage model was verified using six sets of damage data extracted from the literature. The model and experimental data were in good agreement. Furthermore, Mivehchi and Varvani-Ferahni stated that the temperature effects were most pronounced on 90° plies and layups. Higher temperatures lead to a reduction in stiffness and ultimate strength of the fiber reinforced composite. Bureau and Denault [16] conducted fatigue resistance of continuous glass fiber (CGF) composites with both polypropylene (thermoplastic) and polyester (thermoset) resin systems at -40°C, 23°C and 50°C. The thermoplastic resin softens at higher temperature and shows a greater reduction in flexural modulus in contrast to the thermoset. However, its greater ductility gave the thermoplastic superior strength and corresponding greater fatigue resistance. Both Laferie-Frenot and Bellenger et al. described the process of matrix softening, the onset of matrix cracks and propagation of the cracks perpendicular to the load direction.

To reduce the reliance on experimental testing, researchers use the finite element method (FEM) to investigate the viscoelastic micromechanical behavior of the polymer during loading. Using the GMC and concentration tensors proposed by Aboudi [9], Li and

Zhang [17] introduced a linear viscoelastic model for CFRPs and integrated their material model into ABAQUS to describe the microscopic field variables of a single fiber finite element model. Burks et al. [18] utilized FEM to investigate the micromechanics of fatigue failure of Glass Fiber Composites (GFC) and Carbon Fiber Composites (CFC). Using Representative Volume Elements (RVEs) and meshing two configurations, square-packed and hexagonal packing, they investigated stress concentrations between neighboring fibers after aging the composite. At same loading conditions, it was determined that the stress levels in GFC's matrix were higher than the stress levels in CFC's matrix. This was attributed to the carbon fiber's higher stiffness and corresponding higher load bearing capability. Maligno et al. [19] used the FEM to investigate the effect of fiber spacing on local damage onset. By varying spacing between glass fibers, it was demonstrated that reducing fiber spacing increased stress concentrations in the composite matrix which led to localized damage onset and subsequent matrix failure. The work of Burks et al. and Maligno et al. address the issue relevant to composite manufacturing process in which variations in fiber spacing and imperfections including voids cannot be avoided. Analytical methods would not be able to predict stress risers easily because they are limited to simpler fiber geometries and regular fiber patterns.

Currently, the majority of FE material models do model the viscoelastic response of the polymer matrix but neglect to account for the coupled thermo-mechanical response of the matrix under cyclic loading. Experimental results have demonstrated that cyclic loading induces heating in the polymer matrix of CFRC which is detrimental to the load carrying ability. Developing and integrating a FEM material subroutine that will model the nonlinear, thermo-mechanical and viscoelastic response of polymer will enable researchers to correlate experimental results and computational modeling. Accurately modeling the polymer matrix' response in a CFRC under cyclic loading would greatly reduce development and testing cost for companies that rely on composites as load carrying structures.

1.1 Motivation and Research Objective

Early experimental investigations have shown the significant effect of temperatures on the mechanical behaviors of polymers and FRP composites. In addition, continuous cyclic loading, particularly at high frequencies, lead to quite significant temperature generation that might influence the fatigue failure in the material. However, investigating the formation of heat generation during cyclic loading and its effect on the performance of composites is currently lacking. The goal of this research is to examine the effect of energy dissipation from the viscoelastic responses of polymeric matrix on the microscopic and macroscopic mechanical performance of CFRPs. From experimental evidence, we hypothesize that the micromechanical response of the polymeric matrix varies throughout the CFRP and is strongly influenced by the fiber geometry, voids and temperature changes.

To investigate the hypothesis, a 3D constitutive material model which accounts for both the viscoelastic and thermal effects is considered for the polymeric matrix. This constitutive model is implemented in 3D continuum (FE), following the previous work by Khan and Muliana ([20], [21]). Schapery's [22] non-linear viscoelastic constitutive model was modified to include temperature-dependent and stress-dependent properties. Microscopic models of CFRPs that include fiber geometries randomly distributed in matrix domain are generated and implemented in FE. The fiber, in this study carbon fiber is used, is modeled as a linear elastic orthotropic material. The composite is subjected to cyclic mechanical loading at the macroscopic scale, and the variations in the field variables (stress, strain, temperature) at the microscopic scale are examined. This study is organized in five separate sections.

Section 2 introduces the constitutive equations, based on Khan and Muliana's work [20], utilized for the material subroutine in ABAQUS. Section 3 summarizes the MATLAB and Python scripts utilized to create the carbon fiber reinforced geometry and disperse the voids and fibers randomly through the matrix. The specific load cases including longitudinal, shear and transverse loadings are discussed. Boundary conditions including traction, displacement and thermal boundary conditions for the FEM are

reviewed. Furthermore, the material parameters used in the analyses are explained in detail.

Section 4 discusses the overall response of 40%, 50% and 60% fiber volume models subjected to cyclic loading along their fiber direction. Emphasis is placed on describing stress and strain concentrations which are normally found along the fiber-to-matrix interface. The goal of this chapter is to identify if strain risers occur at fiber-to-matrix interfaces and to possibly quantify the strain amplitudes. Furthermore, consideration is also given to identify large polymer matrix deformations within the fiber volume samples.

Section 5 is dedicated to investigating the cyclic frequency effect on a CRFC's field variables including strain, stress and temperature when the cyclic frequency is increased. Section 6 and Section 7 investigate the effect of load direction on thermo-mechanical response of the CRFC. In fact, Section 6 investigates pristine fiber volume samples (without voids) while Section 7 introduces void fiber volume samples. These void fiber volume samples have ellipsoidal voids which are dispersed randomly through the fiber geometries. The section investigates the effect of voids on polymer softening and straining and compares the results to the pristine fiber volume's results. Section 8 is the summary and discussion section of the results.

2 CONSTITUTIVE EQUATIONS

2.1 Viscoelastic Material ABAQUS Subroutine

It is assumed that the model undergoes relatively slow loading, within quasi-static loading. Within a quasi-static loading, inertial effects are negligible. In the absence of body forces and couples, the divergence of the Cauchy stress tensor, which is an equilibrium equation is

$$\text{div}(\bar{\sigma}) = 0 \quad (1)$$

Through the conservation of the angular momentum, the Cauchy stress tensor is symmetric.

$$\sigma_{ij} = \sigma_{ji} \quad (2)$$

Based on Khan and Muliana, the material subroutine uses the generalized three-dimensional visco-elastic constitutive model by Schapery [22] which accounts for stress and temperature-dependent behavior of the material. It is assumed that the material is non-aging. The 3D constitutive equations for an isotropic material is given as follows:

$$\varepsilon_{ij}^t = e_{ij}^t + \frac{1}{3} \varepsilon_{kk}^t \delta_{ij} + \alpha_{ij}^t (T^t - T_0) \quad (3)$$

$$\varepsilon_{ij}^{M,t} = e_{ij}^t + \frac{1}{3} \varepsilon_{kk}^t \delta_{ij} \quad (4)$$

$$\varepsilon_{ij}^{T,t} = \alpha_{ij}^t (T^t - T_0) \quad (5)$$

Equation (3) is the total strain while equation (4) and equation (5) are the mechanical and thermal strains respectively. Furthermore, $e_{ij}^t, \varepsilon_{kk}^t$ refer to the deviatoric and volumetric strain components, respectively. T^t is the temperature at current time t and T_0 is the initial temperature. The superscript t indicates that the variables are taken at current time t . Relating the strain tensor to the stress tensor, and the constitutive relations for viscoelastic materials are:

$$e_{ij}^t = \frac{1}{2} g_0(\bar{\sigma}^t, T^t) J_0 S_{ij}^t + \frac{1}{2} g_1(\bar{\sigma}^t, T^t) \int_0^t dJ(\psi^t - \psi^\tau) \frac{d[g_2(\bar{\sigma}^\tau, T^\tau) S_{ij}^\tau]}{d\tau} d\tau \quad (6)$$

$$\varepsilon'_{kk} = \frac{1}{3} g_0(\bar{\sigma}', T') B_0 \sigma'_{kk} + \frac{1}{3} g_1(\bar{\sigma}', T') \int_0^t dB(\psi' - \psi^\tau) \frac{d[g_2(\bar{\sigma}^\tau, T^\tau) \sigma^\tau_{kk}]}{d\tau} d\tau \quad (7)$$

S'_{ij}, σ'_{kk} refer to the deviatoric and spherical stress components respectively. J_0, B_0 are the instantaneous shear and bulk compliances while dJ is the time-dependent shear compliance. dB is the time-dependent bulk compliance. The integral terms in both equations are the history terms since the strain/stress output of a viscoelastic material depends on its history of loading. ψ' is the reduced-time and is defined as:

$$\psi' = \psi(t) = \int_0^t \frac{d\xi}{a_T^\xi a_\sigma^\xi} \quad (8)$$

and

$$\psi^\tau = \psi(\tau) = \int_0^\tau \frac{d\xi}{a_T^\xi a_\sigma^\xi} \quad (9)$$

For a thermorheologically simple material, a_T and a_σ are temperature and stress-dependent functions. Furthermore the functions g_0, g_1, g_2 are non-linear functions and depend on both the current stress tensor $\bar{\sigma}'$ and current temperature T' . According to Khan and Muliana [21], these material functions are determined through a series of creep and relaxation tests. Furthermore, it is assumed that the corresponding Poisson's ratio remains constant throughout the load history. Therefore the instantaneous bulk compliance is related to instantaneous elastic compliance D_0 as

$$J_0 = 2(1 + \nu) D_0 \quad (10)$$

Likewise, the bulk compliance can be related to the instantaneous elastic compliance D_0

$$B_0 = 3(1 - 2\nu) D_0 \quad (11)$$

The transient shear compliance and bulk compliance terms are described with equation

$$dJ^{\psi'} = 2(1 + \nu) dD^{\psi'} \quad (12)$$

$$dB^{\psi'} = 3(1 - 2\nu) dD^{\psi'} \quad (13)$$

where $dD^{\psi'}$ is the transient elastic compliance and is defined as

$$dD^{\psi^t} = \sum_{n=1}^N D_n (1 - \exp[-\lambda_n \psi^t]) \quad (14)$$

D_n is a compliance term with units MPa^{-1} while λ_n is a time term. The transient compliance can be determined experimentally.

In order to account for the energy dissipation effect, Schapery [23] expressed the Gibbs free energy in terms of stress, temperature and internal state variables (ISVs).

The first law of thermodynamics in Gibbs free energy is expressed

$$\dot{G} + \dot{T}\eta + T\dot{\eta} + \varepsilon_{ij}\dot{\sigma}_{ij} + q_{i,i} = 0 \quad (15)$$

In terms of heat conduction and rate of dissipative work, the first law of thermodynamics can be rewritten as

$$T\dot{\eta} = -T \frac{\partial}{\partial t} \left\{ \frac{\partial G}{\partial T} \right\} = -q_{i,i} + \dot{w}_{dis}^t \quad (16)$$

where $q_{i,i}$ are the heat flux components and \dot{w}_{dis}^t is rate of work dissipation.

The second law of thermodynamics is expressed as

$$T\dot{\gamma} \equiv -\dot{G} - \dot{T}\eta - \varepsilon_{ij}\dot{\sigma}_{ij} - \frac{q_i T_{,i}}{T} \geq 0 \quad (17)$$

$\dot{\gamma}, \eta$ and q_i are the entropy production rate per unit volume, the entropy per unit volume and the heat flux component. The derivative of the Gibbs free energy as

$$\dot{G} = \frac{\partial G}{\partial t} = \frac{\partial G}{\partial \sigma_{ij}} \dot{\sigma}_{ij} + \frac{\partial G}{\partial T} \dot{T} + \frac{\partial G}{\partial \xi_m} \dot{\xi}_m \quad (18)$$

Where ξ_m is a placeholder for internal state variables (ISV). Substituting equation (18) into the second law of thermodynamics equation, we obtain the equation for the rate of energy dissipation:

$$T\dot{\gamma} \equiv \left(-\varepsilon_{ij} - \frac{\partial G}{\partial \sigma_{ij}}\right) \dot{\sigma}_{ij} + \left(-\eta - \frac{\partial G}{\partial T}\right) \dot{T} - \frac{\partial G}{\partial \xi_m} \dot{\xi}_m - \frac{q_i T_{,i}}{T} \geq 0 \quad (19)$$

Equation (19) describes the entropy production rate per unit volume in terms of stresses, temperature and ISVs. The constitutive model and material subroutine should satisfy the

first and second laws of thermodynamics. Furthermore equation (19) must hold for arbitrary $\dot{\sigma}_{ij}$ and \dot{T} . In addition the strain and entropy are defined by:

$$\varepsilon_{ij} = -\frac{\partial G}{\partial \sigma_{ij}} \quad (20)$$

$$\eta = -\frac{\partial G}{\partial T} \quad (21)$$

For isotropic material, Khan and Muliana modified equation (16) by neglecting the coupling effect due to the transient components of thermal expansion and specific heat. Utilizing Fourier's law to express the heat flux, the energy equation was then expressed as

$$\begin{aligned} & \rho c_{\sigma}(T^t) \dot{T} + T^t \alpha(T^t) \dot{\sigma}_{kk}^t + T^t \frac{\partial \alpha(T^t)}{\partial T} \dot{T} \sigma_{kk}^t \\ & + T^t \frac{\partial \alpha(T^t)}{\partial T} \theta^t \dot{\sigma}_{kk}^t + T^t \frac{\partial g_0(\bar{\sigma}, T^t)}{\partial T} D_{ijkl}^{(0)} \dot{\sigma}_{ij}^t \sigma_{kl}^t = k(T^t) T_{,ii}^t \\ & + g_1(\bar{\sigma}^t, T^t) \sigma_{ij}^{vis,t} \left(\frac{d}{dt} \int_0^t dD_{ijkl}(\psi^t - \psi^{\tau}) \frac{d}{d\tau} (g_2(\bar{\sigma}^{\tau}, T^t) \sigma_{kl}^{\tau}) d\tau \right) \end{aligned} \quad (22)$$

$\theta^t = T^t - T_0$ and T_0 is the reference temperature. $\alpha(T^t)$ is the temperature dependent coefficient of thermal expansion. $c_{\sigma}(T^t)$, $k(T^t)$ and $D_{ijkl}^{(0)}$ are the temperature dependent specific heat, temperature dependent thermal conductivity and the instantaneous compliance of the material respectively. dD_{ijkl} is the time-dependent compliance and accounts for the viscoelastic behavior of the material. For a viscoelastic material, the energy generation is caused by the viscous stress $\sigma_{ij}^{vis,t}$. The viscous stress is expressed as

$$\sigma_{ij}^{vis,t} = g_2(\bar{\sigma}^t, T^t) \sigma_{ij}^t - \int_0^t \sum_{n=1}^N \{1 - \exp[-\lambda_n(\psi^t - \psi^{\tau})]\} \frac{d[g_2(\bar{\sigma}^{\tau}, T^t) \sigma_{ij}^{\tau}]}{d\tau} d\tau \quad (23)$$

The viscous stress is a function of time and effective stress parameters $g_2(\bar{\sigma}^t, T^t)$, current stress σ_{ij}^t and λ_n which the Prony Series terms. The Prony series terms were calibrated by Khan and Muliana [20]. The carbon fibers are modeled as linear elastic orthotropic materials.

The equations are incorporated into a FORTRAN ABAQUS UMAT material subroutine and implemented in the commercial finite element code. The full derivation of the equations and recursive method utilized in the finite element material subroutine are found in Khan and Muliana ([20],[21]).

3 MODEL CREATION – MATERIAL PROPERTIES – LOAD CASES

3.1 3D Finite Element Creation

ABAQUS models are created using MATLAB and Python scripts. The MATLAB script lays out the geometry based on fiber percentage, thickness of individual fiber strands and minimum fiber spacing. The Python script converts the corresponding text file into geometry in ABAQUS. Meshing, material assignments and load cases are assigned automatically using the Python script. The task of the scripts is to create composite models with specified fiber content and randomize the fiber placement throughout the geometry. In general, minimum fiber spacing varied between 2.5% and 10% of the fiber radius. This is necessary to prevent mesh distortion and to allow the finite elements to accurately capture stress and strain fields between adjacent fibers. Hexagonal finite elements give reliable results when the aspect ratio does not exceed 10-to-1 and internal angles within the element are between 70° to 120° . If possible, three elements should be placed between fibers to improve accuracy. However, this increases the computational time. In addition, to study the effects of voids on the strain and stress field of a carbon fiber-epoxy composite, ellipsoidal voids are added to the matrix. The previously mentioned MATLAB script is expanded to disperse a preset number of voids throughout the composites. The size of the voids is a percentage value of the fiber radius. In the model, the fiber tow diameter is 7.1 microns. Therefore, the maximum major void radius would be 0.15×3.55 microns. Table 1 shows the respective void geometry parameters as a percentage of the fiber diameter dimension.

Table 1 Void Geometry Parameters

	Maximum (%)	Minimum (%)
Major Radius	15	1
Minor Radius	15	1
Spacing to next fiber or void	N/A	8

The placement and dimension of the voids are randomized. The void geometric parameters can be computed by multiplying the percent value with the fiber radius. Overall, 40%, 50% and 60% fiber volume samples are created. Figure 1 shows a finite element model with voids dispersed throughout the model. Initially, each fiber model configuration contains 12 fibers. However, the number of elements required to obtain an accurate mesh increases when 12 fibers are placed. As a tradeoff, reducing the number of elements to decrease the computational time can affect the accuracy of the results. Therefore, to reduce computational cost, only microstructural models with four fibers per configuration are considered.

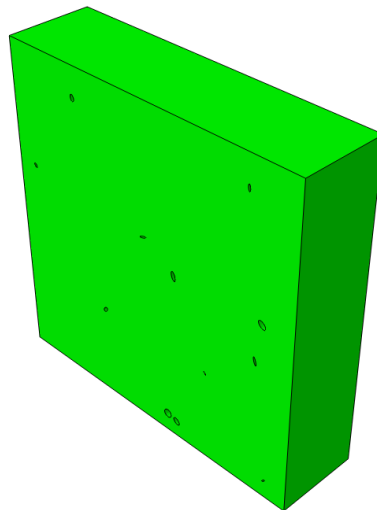


Figure 1 Finite Element Model with Voids

Unless otherwise stated, the finite elements used are C3D8T elements which are 3D hexagonal, fully integrated and displacement-mechanical coupled finite elements. In certain load cases, reduced integration elements are used to reduce the size of the output database.

3.2 Material Properties

The carbon reinforced polymer composites use Hexcel AS4 and FM73 polymer properties. AS4 carbon fiber is selected because it is a commercially common aerospace grade carbon fiber. A 12,000 filament tow is selected which has a tow diameter of 7.1 microns. Elastic modulus in the longitudinal direction and thermal properties are available from Hexcel AS4 [24] but remaining material properties are supplemented by Hexcel IM7 fiber properties taken from Hu and Sun [25]. It is noted in this study FM73 polymer is considered for the matrix mainly because the thermo-viscoelastic material parameters for this material are available, which have been completely summarized in Muliana and Khan [26]. The instantaneous elastic modulus and Poisson's ratio of the studied FM73 are comparable to those of typical polymeric matrix in CFRPs. Table 2 presents Hexcel AS4 Carbon fiber material properties.

Table 2 AS4 Carbon Fiber Properties

Hexcel AS4 Carbon Fiber	
E11	231 GPa
E22	14.6 GPa
E33	14.6 GPa
v12	0.25
v13	0.25
v23	0.30
G12	55.66 GPa
G13	55.66 GPa
G23	5.64 GPa
Specific Heat c_p	0.27 cal/g-°C
Coefficient of Thermal Expansion (CTE)	-0.63 ppm/°C
Thermal Conductivity	6.83 W/m-°K
Density	1.79e-6 10 ³ kg/mm ³
Fiber Diameter (12k tow)	0.7818 mm

Peretz and Weitsman ([27], [28]) characterized FM73 adhesive polymer by performing a 15 min creep test followed by a 15 min recovery test. Furthermore, the material was tested under uniaxial stresses ranging from 10 – 30 MPa and temperatures ranging from 30 - 60°C. The nonlinear stress and temperature response is fitted using the following three material parameters:

$$g_0 = (1 + 0.15 \frac{\sigma}{50})(1 + 0.91 \frac{T - T_0}{T_0}) \quad (24)$$

$$g_1 = (1 + 1.435(\frac{\sigma}{50})^{2.4})(\exp[-8.5 \frac{T - T_0}{T_0}]) \quad (25)$$

$$g_2 = (1 + 0.75(\frac{\sigma}{50})^2)(\exp[12.12 \frac{T - T_0}{T_0}]) \quad (26)$$

where σ is the stress, T is the temperature and T_0 is the reference temperature. Peretz and Weitsman set the reference temperature at 303 Kelvin. In addition, the time-dependent material properties of FM73 are captured using a six term Prony series. Muliana and Khan [29] make extensive use of the same material properties. Table 3 represents the FM73 material properties.

Table 3 FM73 Material Properties

FM73 Material Properties	
E	2710 MPa
ν	0.35
Specific Heat c_p	1300 J/kg °K
Thermal Conductivity k	0.2 W/m °K
Coefficient of Thermal Expansion (CTE)	66 ppm/°C
Density	980e-6 10 ³ kg/mm ³
FM73 Viscoelastic Response Properties	
MPa^{-1}	τ_R (minutes)
21.00×10^{-6}	60
21.60×10^{-6}	6
11.84×10^{-6}	0.6
15.88×10^{-6}	0.06
21.58×10^{-6}	0.006
21.05×10^{-6}	0.0006

3.3 3D Finite Element Load Case

For all load cases, the models utilize the fully-coupled thermo-mechanical nonlinear viscoelastic material subroutine developed by Khan and Muliana. The FM73 polymer is assumed to be a thermorheologically simply material. Carbon fibers are modeled as linear-elastic orthotropic material. Perfect bonding is assumed between fiber and polymer matrix.

There are three primary load configurations: Longitudinal loading, shear loading and transverse loading. All models were analyzed in longitudinal, shear and transverse loading. To establish a standard coordinate system, we refer to the longitudinal as 3-direction or z-axis. The 1-direction is aligned with the x-axis and 2-direction is aligned with the y-direction. In the study, we will refer to the front face and back face of the model. Figure 2 shows the general coordinate system and designates both the front face and back face. Figure 3 shows the back view of a general model.

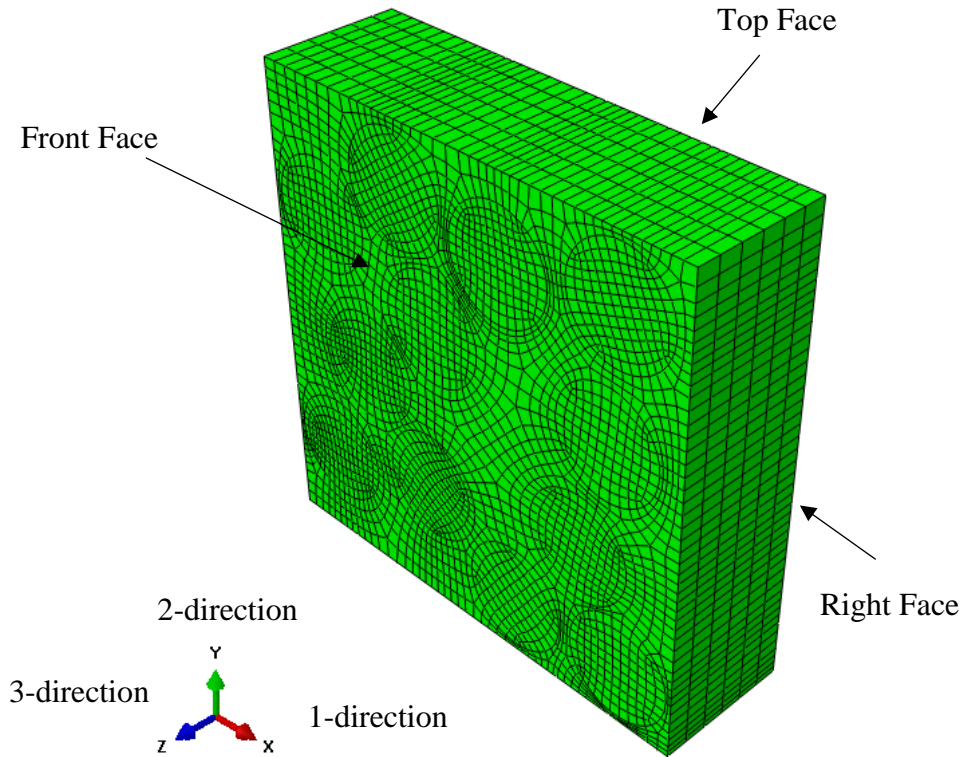


Figure 2 Coordinate System Front View

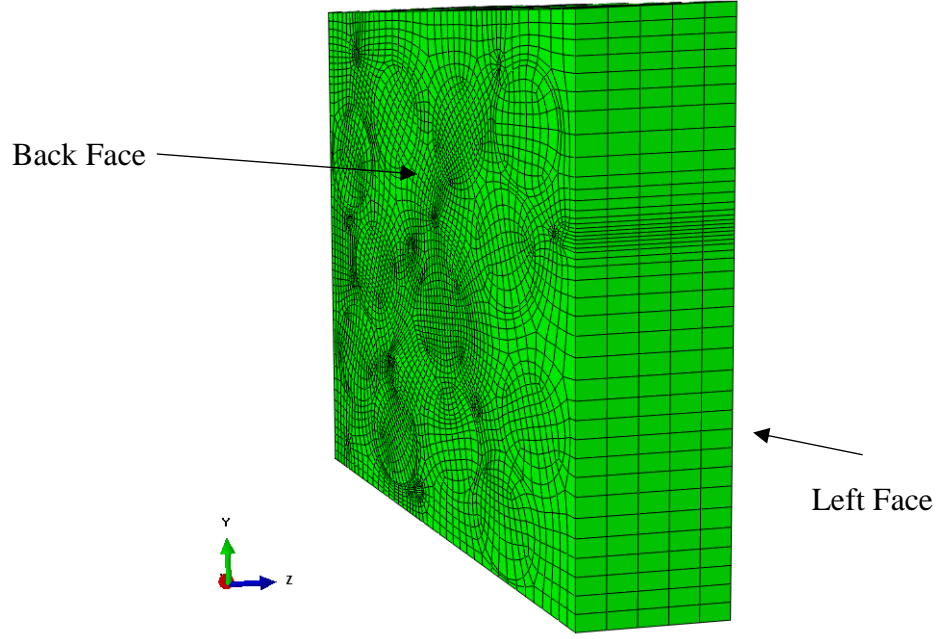


Figure 3 Coordinate System Back View

For both the longitudinal and transverse load cases, periodic boundary conditions are used. This indicates that nodes of the back face are restrained along the 3-direction. The right face nodes are restrained along the 1-direction and the top face nodes are fixed along the 2-direction. Constraints are imposed in order to maintain uniform displacements. For example, tying the nodes on the front face with an equation will force all nodes on the front face to displace uniformly along the 3-direction. Using equations in ABAQUS, the left face nodes are tied to displace uniformly along the 1-direction while the bottom face nodes are tied to move uniformly along the 2-direction. Equation (27) describes the periodic boundary condition imposed on the 3D finite element models.

$$\begin{aligned}
 u_1(w, x_2, x_3, t) &= 0 \\
 u_2(x_1, h, x_3, t) &= 0 \\
 u_3(x_1, x_2, d, t) &= 0
 \end{aligned} \tag{27}$$

u_i is the displacement, where $i = 1, 2, 3$ and refers to the three faces. W refers to the width, h refers to the height and d refers to the depth of the model. t is the time. The fiber configurations are loaded along three directions individually: Longitudinal, transverse and shear. The goal is to investigate the energy dissipation of the fiber configuration under cyclic loading and to compare both the macroscopic and microscopic responses of the composites. The microscopic response refers to the internal field variables including stress, strain and temperature near the fibers and in the polymer matrix. For the longitudinal loading, a node is selected on the front face (with the face normal vector pointing along the 3-direction) and the node is forced to displace by 0.01 mm to 0.03 mm. A displacement boundary condition instead of a traction boundary condition is selected to be able to instantly calculate the longitudinal strain. Similarly, for the transverse loading, a node on the left face of bottom face is selected and displaced along the 1-direction or 2-direction respectively. For shear loading, the models are subjected to simple shear. The back face is constrained in both 3-direction and 1-direction. The top face is constrained in the 2-direction only. A node on the front face is selected and a displacement is applied along the 1-direction.

The fiber configurations are cycled with a sinusoidal varying displacement amplitude to simulate repeated loading of a load bearing structure such as an aircraft wing. The simulated cyclic loading duration varies from six minutes up to 30 minutes. The cyclic frequencies vary from 2/60 Hz up to 10/60 Hz. The frequencies are selected randomly but are small to simulate quasi-static loading and to reduce the computational times. As mentioned in the introduction section, experimental work has demonstrated that fiber-polymer composites heat up when subjected to cyclic fatigue loading. Furthermore, the fracture and corresponding failure mechanisms change when the polymer matrix undergoes a temperature change. To impose the worst-case heating onto the polymer matrix, adiabatic boundary conditions are enforced on all faces of the sample. This ensures that highest temperature increase. Equation (28) describes the thermal boundary conditions across the respective boundaries.

$$\begin{aligned}
\frac{\partial T(0, x_2, x_3, t)}{\partial x_1} &= \frac{\partial T(w, x_2, x_3, t)}{\partial x_1} = 0; 0 \leq x_2 \leq h, 0 \leq x_3 \leq d \\
\frac{\partial T(x_1, 0, x_3, t)}{\partial x_2} &= \frac{\partial T(x_1, h, x_3, t)}{\partial x_2} = 0; 0 \leq x_1 \leq l, 0 \leq x_3 \leq d \\
\frac{\partial T(x_1, x_2, 0, t)}{\partial x_3} &= \frac{\partial T(x_1, x_2, d, t)}{\partial x_3} = 0; 0 \leq x_1 \leq l, 0 \leq x_2 \leq h \\
t &\geq 0
\end{aligned} \tag{28}$$

Equation (28) indicates that the heat flux across boundaries is zero. All nodes in the sample are set to an initial starting temperature of either 298 Kelvin or 303 Kelvin. Since the coupled thermo-mechanical constitutive equations are highly nonlinear, the fixed time increment is set at 0.01 min.

3.4 Convergence Study

Three 40% models are meshed with three mesh densities to study mesh convergence. The models are loaded in both longitudinal and transverse direction. Hexagonal C3D8RT elements are chosen and approximate element length of the models are 0.08 mm, 0.065 mm and 0.060 mm. The models are labeled as coarse, fine and extra fine. Mesh convergence is achieved when the calculated compliance of the model reaches a steady-state value, i.e. the homogenized compliance of the extra fine mesh compared to the homogenized compliance of the fine mesh differs by a few percentages only. In longitudinal loading, the displacement boundary is 0.02 mm and is applied on the front face of the model. The length along the load direction is 1 mm. Therefore the 0.02 mm displacement amplitude corresponds to 2% longitudinal strain. Cyclic frequency for longitudinal loading is 2/60 Hz and the models are cycled for 1 minute. The goal is to reduce the number of elements required to achieve convergence and minimize computational times. Table 4 shows the number of C3D8T elements and nodes in the individual configurations.

Table 4 Convergence Study - Mesh Configuration

Mesh Density	Mesh Density (Approx. element length)	Number of Elements	Number of Nodes
Coarse	0.08	41067	45570
Fine	0.065	55590	61056
Very Fine	0.060	88944	96462

For a linear-elastic material undergoing axial loading along its longitudinal loading, the relationship between the homogenized stress and strain is given as

$$\sigma_{33} = E \varepsilon_{33} \quad (29)$$

where σ_{33} is the average normal stress along the 3-direction and ε_{33} is the average normal strain along the 3-direction. E is the effective stiffness of the fiber model along its longitudinal or 3-axis. The average normal stress is computed through

$$\sigma_{33} = \frac{RF_3}{A} \quad (30)$$

where RF_3 is the total reaction force in the 3-direction. A is the area of the load surface where the traction load is applied. For the 40% fiber volume model, the area A is 14.394 mm^2 . In this case, the total reaction force in the 3-direction is obtained by summing the individual reaction forces of the nodes. The average normal strain ε_{33} is given as

$$\varepsilon_{33} = \frac{\Delta L}{L_0} \quad (31)$$

ΔL is the change of length of the model along its longitudinal direction. L_0 is the original depth dimension of the fiber model. The stiffness is computed at two separate time steps, 0.100 minutes and 0.400 minutes. Table 5 summarizes the effective stiffness response of the three finite element models with different mesh densities.

Table 5 Convergence Study - Effective Stiffness

	Step time = 0.100 minutes			Step time = 0.400 minutes		
Mesh Density	Average Strain ϵ_{33}	Average Stress σ_{33} (MPa)	Effective Stiffness (MPa)	Average Strain ϵ_{33}	Average Stress σ_{33} (MPa)	Effective Stiffness (MPa)
Coarse	1.9021e-02	137.21	7213.84	-1.9021e-02	-139.57	7213.84
Fine	1.9021e-02	137.42	7224.83	-1.9021e-02	-139.78	7348.72
Finest	1.9021e-02	137.47	7227.38	-1.9021e-02	-139.83	7351.32

Plotting the stiffness against stiffness and computing the percent difference, it appears that the coarse model is refined enough to accurately capture the longitudinal response of the 40% fiber volume finite element model. Figure 4 shows the stiffness of the fiber models as a function of the mesh density, measured in number of elements through the thickness. In addition, the graph shows the stiffness for both 0.100 minute timestep and 0.400 minute timestep. From the figure, refining the mesh density does not substantially change the stiffness response of the 40% fiber model.

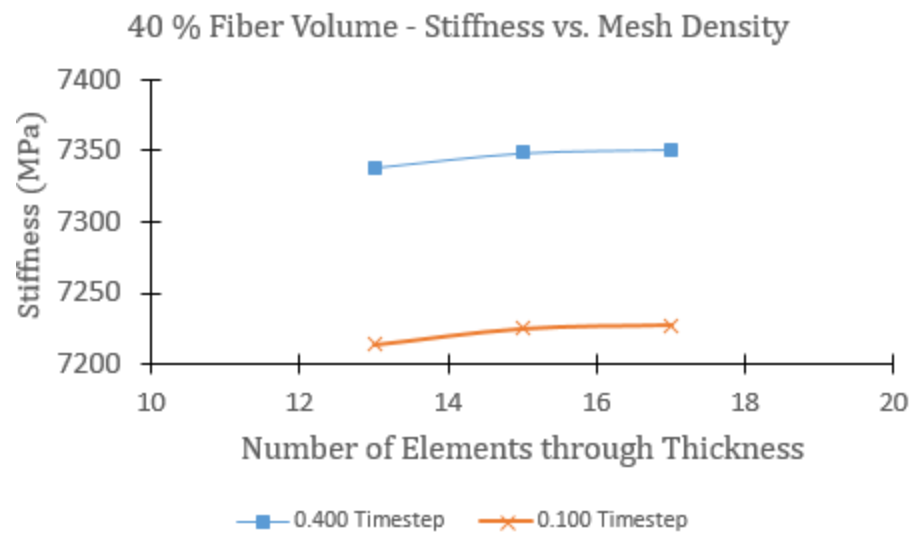


Figure 4 Stiffness vs. Mesh Density - Convergence Study

4 LONGITUDINAL LOADING – HOMOGENIZED VS. MICROSTRUCTURAL RESPONSE

Heating and accompanying temperature increase are observed in all fiber configurations when they were cycled at frequency 2/60 Hz and 3/60 Hz. The displacement amplitude applied to the model is 0.02 mm in the longitudinal direction, which corresponds to 2% longitudinal strain. The homogenized hysteresis response is obtained by plotting the average longitudinal stress versus average longitudinal strain. The average longitudinal stress is obtained by dividing the reaction forces at the boundary nodes with the traction area. The average longitudinal strain is computed by dividing change in longitudinal length through the original length. Figure 5 illustrates the homogenized (macroscopic) hysteresis response for the 40% fiber volume configuration. The blue trace is the response under frequency 3/60 Hz and the orange trace is the response under frequency 2/60 Hz.

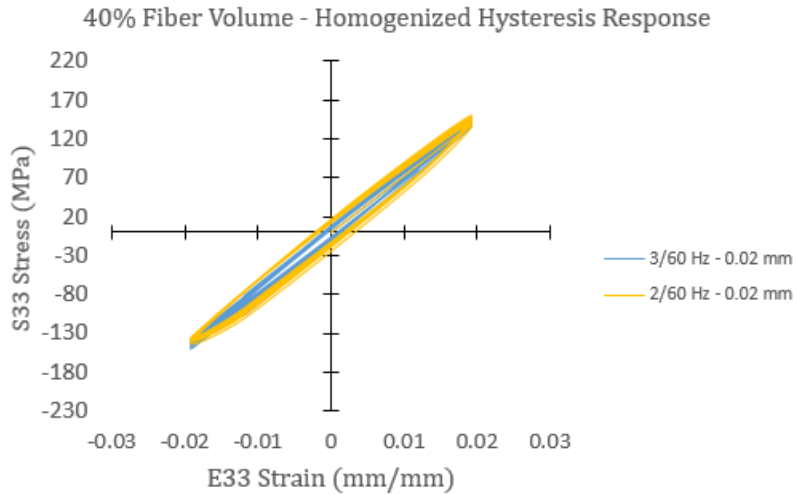


Figure 5 40% Fiber Volume - Homogenized Hysteresis Response

Similarly, Figure 6 and Figure 7 are the homogenized hysteresis response for both the 50% fiber volume and 60% fiber volume homogenized hysteresis response.

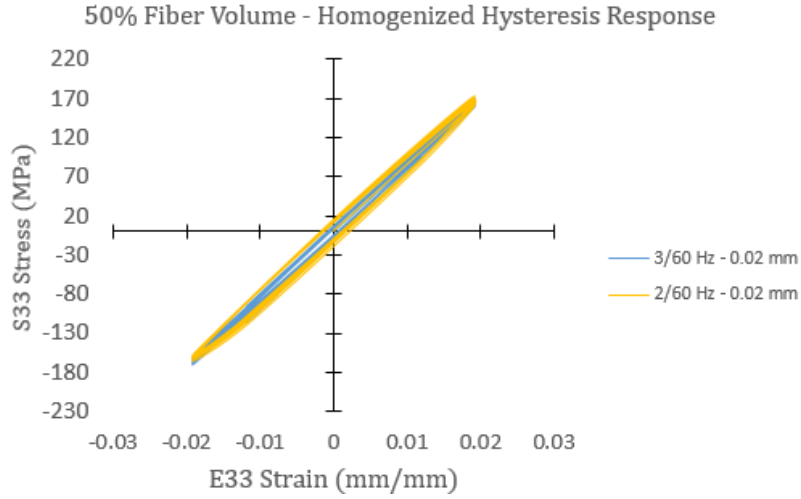


Figure 6 50% Fiber Volume - Homogenized Hysteresis Response

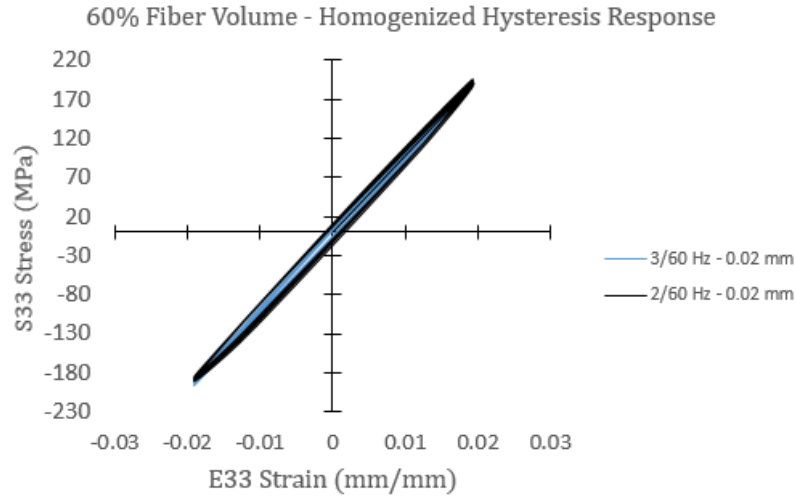


Figure 7 60% Fiber Volume - Homogenized Hysteresis Response

Within the same fiber configurations, changing the cyclic frequency only minimally affects the homogenized stress amplitudes. Furthermore, the hysteresis loops do not exhibit large nonlinear behavior, the loops are eccentric. For all homogenized hysteresis loops, the homogenized longitudinal strain cycles between -2% and +2%. Table 6 summarizes the maximum and minimum longitudinal stresses in the homogenized response. As expected, increasing the fiber content increases the longitudinal stiffness. As

a result, with the same displacement amplitude applied, the maximum and minimum stress magnitudes increase with increasing fiber content.

Table 6 Max/Min Stress - Homogenized Response

Frequency	2/60 Hz	3/60 Hz
Fiber Volume	Max/Min Stress (MPa)	Max/Min Stress (MPa)
40%	150.24/-139.41	146.85/-149.25
50%	171.19/-162.99	168.26/-170.28
60%	194.85/-187.96	192.19/-194.22

Although the homogenized hysteresis response shows a close to linear-elastic behavior with relatively small dissipation, the microscopic field variables are highly non-linear and include significant dissipation effect, which will be shown later. Observing the axial strain E33 contour plot for all three fiber configurations, strain risers are noticeable in the polymer matrix near fibers. The strain risers become pronounced when the polymer matrix neighbors two adjacent fibers. For nomenclature reasons, we shall refer to the location as matrix/fiber location. Figure 8 is the maximum principal strain contour plot of the 40% fiber volume configuration, cycled at frequency 3/60 Hz. The maximum principal strain contour plot is taken at 1.9 minutes after loading starts and the principal strain is 3.67%. Plotting the principal strain at this specific location versus time, Figure 9 shows that the principal strain for the 40% fiber volume configuration. The strain amplitude is at 3% initially but increases slightly to 3.8% throughout the 25 minute load period. The principal strain plot for the 50% fiber volume configuration and 60% fiber volume configuration are found in Figure A-1 and Figure A-2.

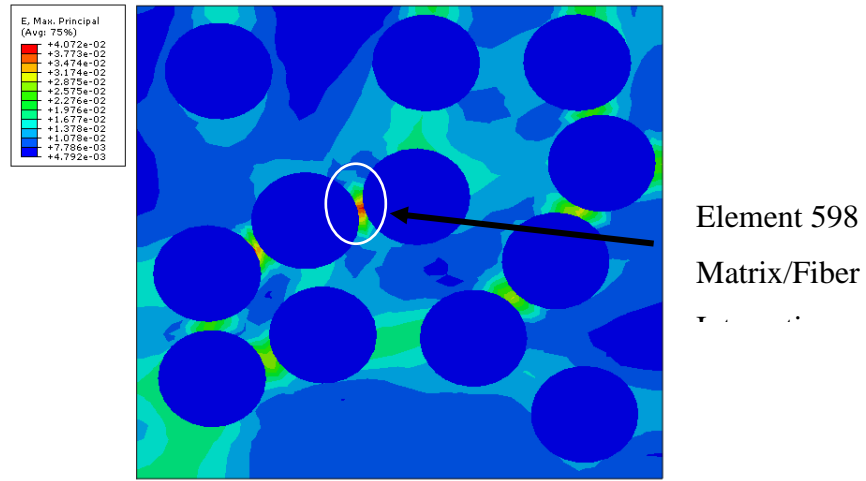


Figure 8 40% Fiber Volume – Longitudinal Loading – 3/60 Hz – Max Principal Strain -1.9 minutes

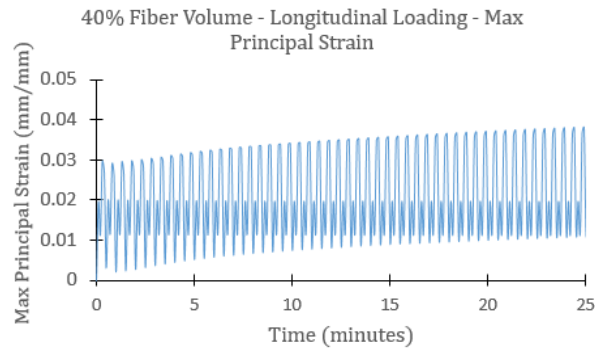


Figure 9 40% Fiber Volume - Longitudinal - 3/60 Hz - Max Principal Strain

In addition, plotting the localized hysteresis response, it is evident that the response is highly nonlinear and shows significant dissipation (Figure 10). Figure 10 is the localized hysteresis response for the 40% fiber volume matrix/fiber location, the green hysteresis trace refers to the frequency 3/60 Hz response and the blue trace refers to the frequency 2/60 Hz response. For the sample under 3/60 Hz cyclic frequency, the longitudinal stress oscillates between -45.38 MPa and 49.07 MPa. Similarly, for the 2/60 Hz frequency, the maximum longitudinal stress is 58.81 MPa and the minimum longitudinal stress is -50.57 MPa. Increasing the number of cycles by one cycle per minute does not affect the overall stress response. However, comparing the localized hysteresis response to the homogenized

hysteresis response, the longitudinal stresses are lower and the hysteresis loops are highly nonlinear.

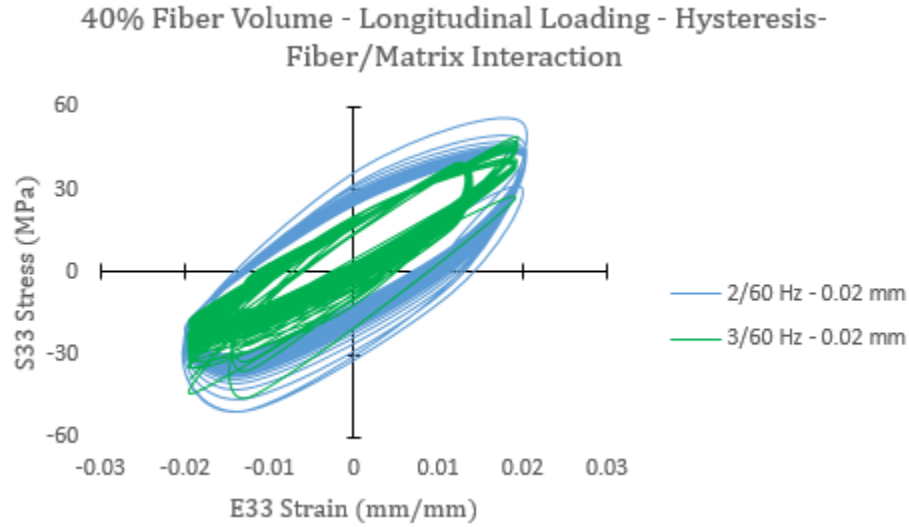


Figure 10 40% Fiber Volume – Longitudinal Loading- Hysteresis – Fiber/Matrix

Expanding the observations towards the 50% fiber volume configuration and the 60% fiber volume configuration, stress and strain risers are found in all polymer matrix adjacent to two neighboring fibers. Figure 11 are the principal strain contour plots for both 50% fiber volume and 60% fiber volume. In the pictures, the 50% fiber volume contour plot is taken at 0.4 minutes after beginning of loading and the 60% fiber volume configuration strain contour is taken at 19.9 minutes. Noteworthy is that in the 50% fiber volume's model, fibers are placed randomly in the sample while the 60% fiber volume's fibers were placed in a hexagonal pattern. From Figure 11 at the matrix/fiber location, the localized hysteresis responses are plotted in Figure 12 for both 50% and 60% fiber volume contents. Each plot also contains the response for frequency 2/60 Hz and 3/60 Hz.

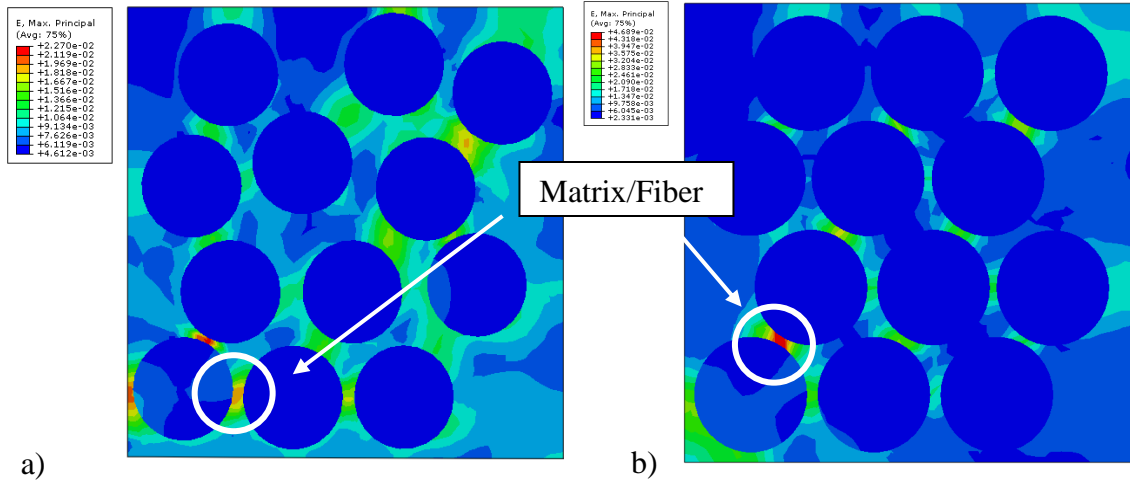


Figure 11 Principal Strain a) 50% Fiber Volume – 0.4 minutes b) 60% Fiber Volume – 19.9 minutes

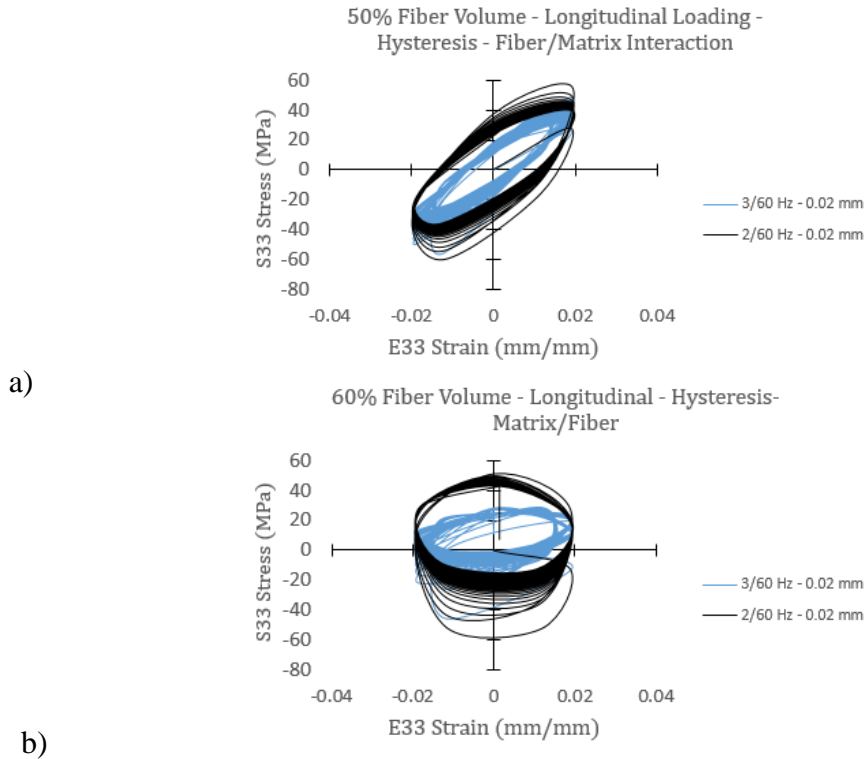


Figure 12 Hysteresis Response a) 50% Fiber Volume b) 60% Fiber Volume

The localized hysteresis responses maximum/minimum stresses and strains are summarized in Table 7. The longitudinal strains across all configurations differ minimally and vary from 1.93% to 1.97%. Furthermore, the maximum longitudinal stresses vary

from 29.08 MPa to 55.74 MPa. Comparing the localized hysteresis response to the homogenized hysteresis response, we conclude that longitudinal stresses are lower for the localized response but longitudinal strains are similar to the homogenized longitudinal strains. However, similar to the 40% fiber volume localized hysteresis response, the 50% fiber volume and 60% fiber volume hysteresis responses are also nonlinear.

Table 7 Hysteresis Response - 50% Fiber Volume - 60% Fiber Volume

Cyclic Frequency	2/60 Hz		3/60 Hz	
	Max/Min Longitudinal Stress (MPa)	Max/Min Longitudinal Strain (%)	Max/Min Longitudinal Stress (MPa)	Max/Min Longitudinal Strain (%)
50% Fiber Volume	55.74/-60.51	1.97/-1.92	49.17/-56.09	1.93/-1.93
60% Fiber Volume	51.40/-52.47	1.93/-1.89	29.08/-46.29	1.93/-1.95

Observing the polymer matrix of the 50% fiber volume model, the polymer matrix undergoes significant softening at the end of the 20-minute load cycle. Figure 13 is the principal strain contour plot of the 50% fiber volume model, cycled at 2/60 Hz and 0.02 mm displacement boundary conditions. At the end of the 20-minute cycle, the polymer regions at the sample's edges show large strains. To delineate the two different regions of interest, we refer to the locations as Matrix 1 and Matrix 2 location respectively. At 20 minutes, the principal strain at Matrix 1 location is 3.42% and the principal strain at Matrix 2 location to 2.01%. However, the majority of the polymer matrix is at 0.29% strain. Furthermore, plotting the principal strain versus time, it is evident that the existence of the residual stresses causes the polymer matrix to creep even after the cyclic load is removed. Figure 14 contains the principal strain plots for both Matrix 1 and Matrix 2 locations. The figures highlight that the residual stresses cause the material to creep at 20 minutes. At the

Matrix 1 location, the principal strain increases from 3.42% to 26.8%. Similar, at the Matrix 2 location, the principal strain increases from 2.01% to 17.10%. The corresponding principal stress history for Matrix 1 location is given in the appendix, Figure A-3. Matrix softening is also observed in the 40% fiber volume sample and a snapshot of the softened region can be found in the appendix, Figure A-4.

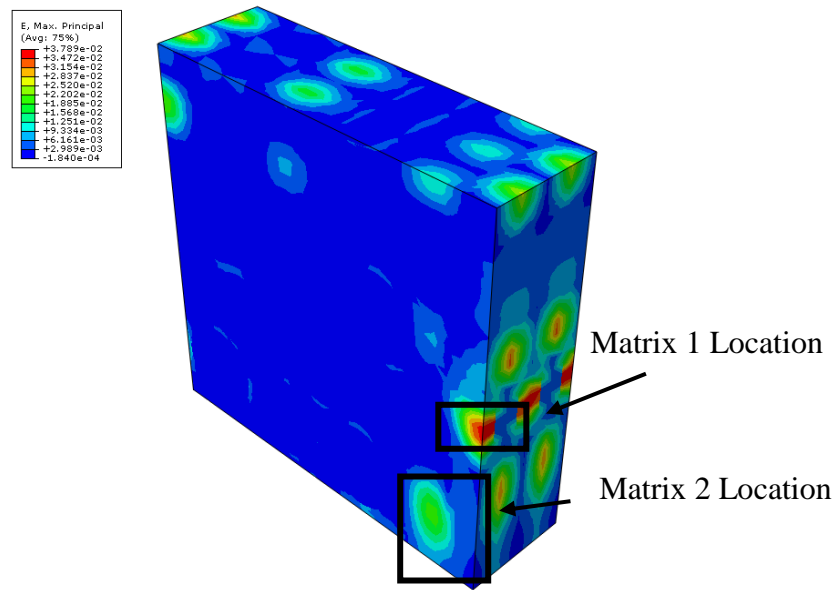


Figure 13 50% Fiber Volume - 2/60 Hz - 0.02 Disp. - Max Principal Strain – 20 minutes

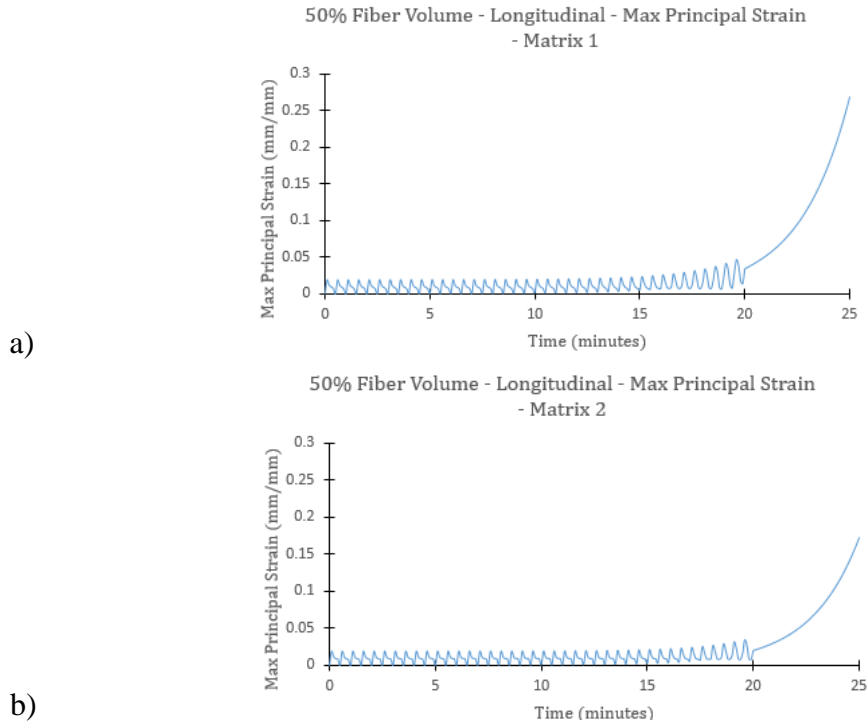


Figure 14 50% Fiber Volume Principal Strain a) Matrix 1 Location b) Matrix 2 Location

The temperature change for all three fiber configurations is significant. Initial temperature for the configurations is 303 Kelvin. At 20 minutes, the samples reached a temperature ranging from 332.24 Kelvin to 333.09 Kelvin. Within the same fiber configuration i.e. 40% fiber volume, the temperature change for 2/60 Hz cyclic frequency is higher than the 3/60 Hz frequency model. This trend is observed across all fiber configurations. Figure 15 shows the temperature rise for all three fiber configurations. The temperature distribution throughout the models is uniform at the individual time steps because of the slow rate of loading and that heat conduction is permitted across the fiber/matrix interface. Contour plots of the temperature for the 40% fiber volume model can be found in Figure A-5 through Figure A-8.

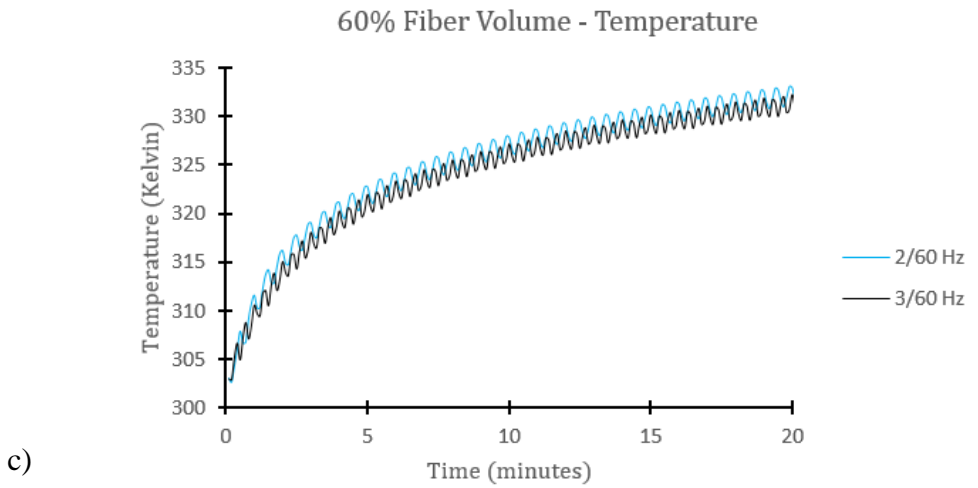
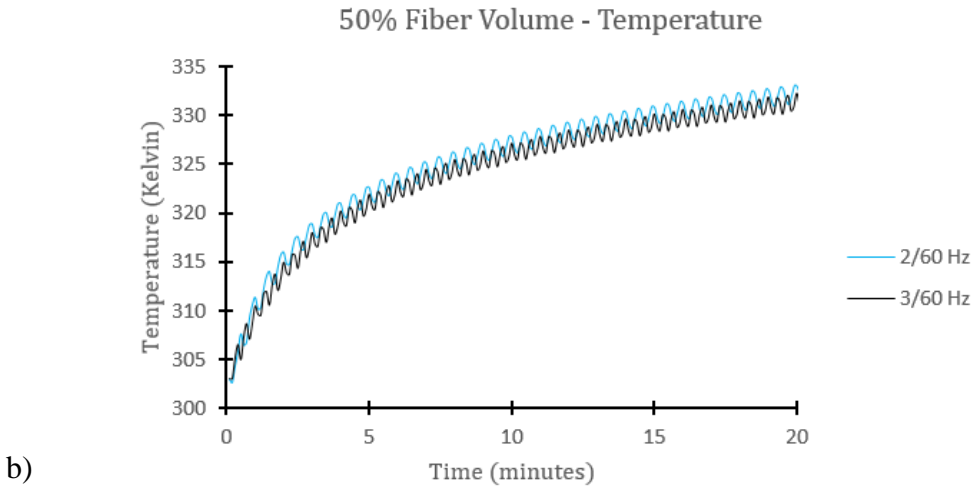
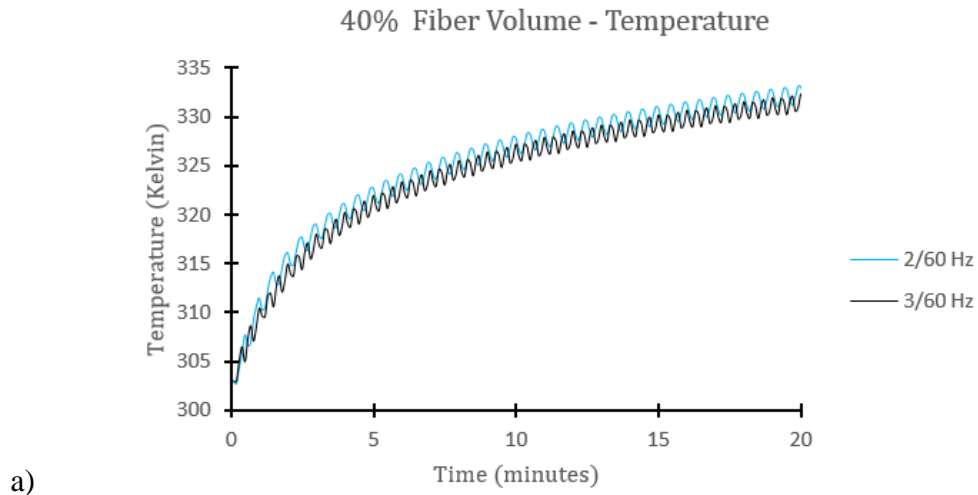


Figure 15 Longitudinal Loading Temperature Change a) 40% Fiber b) 50% Fiber c) 60% Fiber

The temperature change for the three fiber configurations is similar in magnitude and the fiber content and frequency have a negligible effect on the temperature change. However, the 60% fiber volume is also simulated with a 0.03 mm displacement amplitude instead of the standard 0.02 mm displacement amplitude. Figure 16 is the temperature plot for the 60% fiber volume configuration at 3/60 Hz cyclic frequency. The graph shows the temperature change for both 0.02 mm and 0.03 mm displacement. At 20 minutes, the 0.02 mm displacement simulation is at 332.24 Kelvin and the fiber configuration, simulated at 0.03 mm displacement, is at 336.83 Kelvin. This demonstrates that changing the applied displacement induces a greater temperature in the model than changing the frequency by 1/60 Hz. Furthermore, an additional hysteresis plot for the 60% fiber volume configuration is shown in Figure A-9 and is located in the appendix.

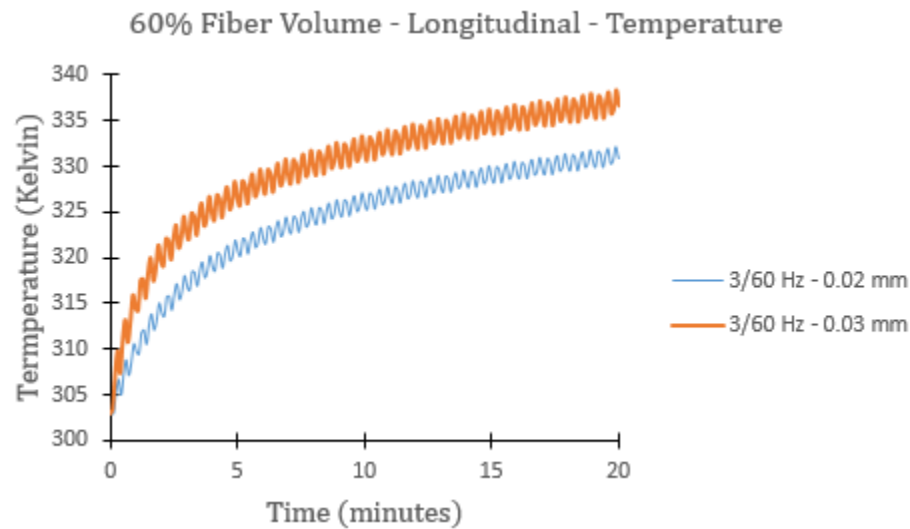


Figure 16 60% Fiber Volume - Temperature - Displacement Boundary Comparison

The repeated cycling increases the temperature of the model which affects the principal strains. To correlate the principal strain to the respective temperature, Figure 17 plots the principal strains for each fiber volume model against the respective temperature. The load case is 0.02 mm and 2/60 Hz cyclic frequency. The regions of interest for all three fiber volume models are at the fiber/matrix interface. For the matrix/fiber interface, the principal strain begins to increase at approximately 320 Kelvin. At 320 Kelvin, the

40% fiber content model has a maximum principal strain of 3.10%. The 50% fiber content model has a maximum principal strain of 2.75% and the 60% fiber content model has a maximum principal strain of 4.49%. All the principal strains increase to 3.49%, 2.97% and 4.82% at 330 Kelvin. In general, the maximum principal strains increase gradually throughout the load cycle.

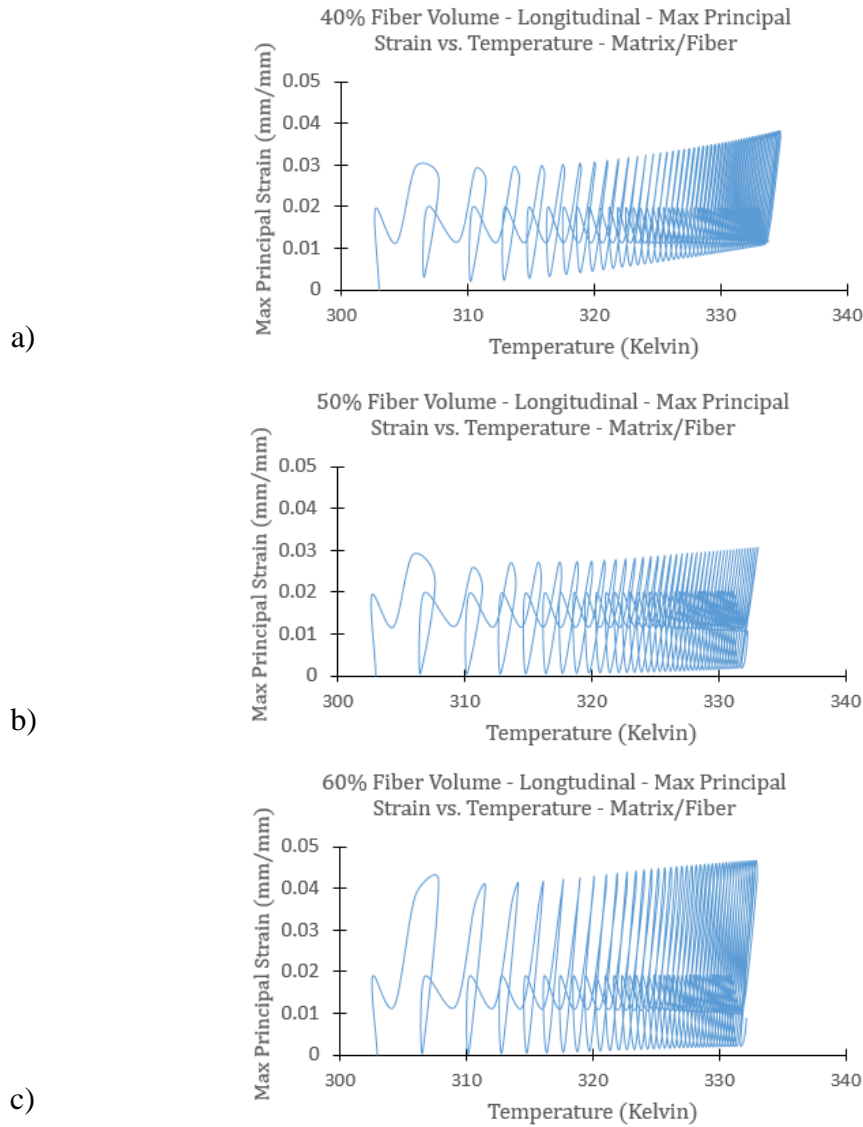


Figure 17 Max Principal Strain vs. Temperature - Longitudinal Loading – 2/60 Hz - a) 40% Fiber Volume
b) 50% Fiber Volume c) 60% Fiber Volume

5 THE EFFECT OF CYCLIC FREQUENCY ON POLYMER SOFTENING

To investigate the effect of cyclic frequency on heat generation and constitutive response of the carbon-reinforced composite, a 40% fiber volume model is cycled at an increased cyclic frequency. The chosen frequencies are 5/60 Hz and 10/60 Hz. The number of fibers is reduced from 12 fibers to 4 fibers and C3D8RT thermo-displacement reduced elements are used to minimize computational time and reduce convergence errors. A displacement amplitude of 0.0075 mm, corresponding to 0.75% longitudinal strain, is applied along the longitudinal (fiber) direction of the carbon-reinforced composite. Figure 18 shows the 40% fiber volume finite element model. The respective loading directions are also indicated. The 5/60 Hz model runs for 6.4 minutes until the excessive deformation in the polymer matrix causes convergence issues. Figure 19 shows the maximum principal strain the 5/60 Hz model after 6.4 minutes of loading. The maximum principal strain is 71.80 %, indicating a highly nonlinear deformed region.

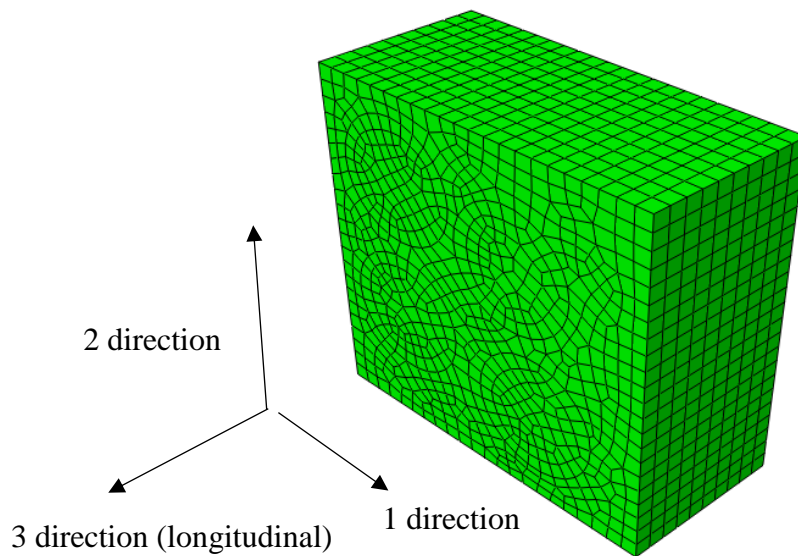


Figure 18 40% Fiber Volume - Frequency Model

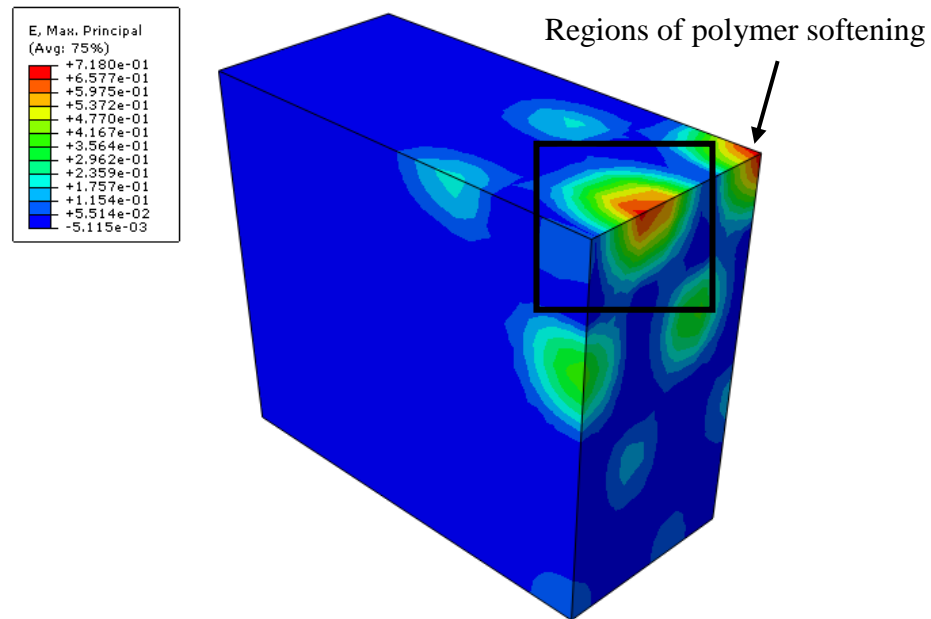


Figure 19 40% Fiber Volume – 5/60 Hz – Max Principal Strain – 6.4 minutes

FM73 is a brittle polymer and the principal strain exceeds 7%. Although the polymer matrix should fail, the material subroutine does not account for viscoplasticity or failure and does not model the initiation of cracks and subsequent failure accurately. An additional observation is that the fibers act as strain risers for neighboring polymer matrix. The principal strain near a matrix/fiber polymer element is 0.82% in contrast to polymer at a distance away from the fiber which is at 0.47% strain. A contour plot of the matrix/fiber strains is provided in the appendix, Figure A-10. Also, the locations of interests are shown in Figure A-10. The fiber to matrix interfaces have strain and stress risers, however, they also prevent excess deformation in the polymer matrix. Figure 19 demonstrates that the softening and nonlinear deformation occurs in the polymer matrix regions distant from the fibers and near the fiber volume's edges. Figure 20 shows the principal strains for the fiber/matrix element and matrix element. The fiber/matrix's strain value is initially 0.75% but increases steadily until it reaches a steady-state value of 1.1 % after six minutes. In contrast, the principal strain in the polymer region oscillates between 0% and 0.8% and rapidly rises starting at 4 minutes. After 6.4 minutes of loading, the

maximum principal strain in the polymer reaches 71.8 % which will certainly constitute strain failure in the polymer.

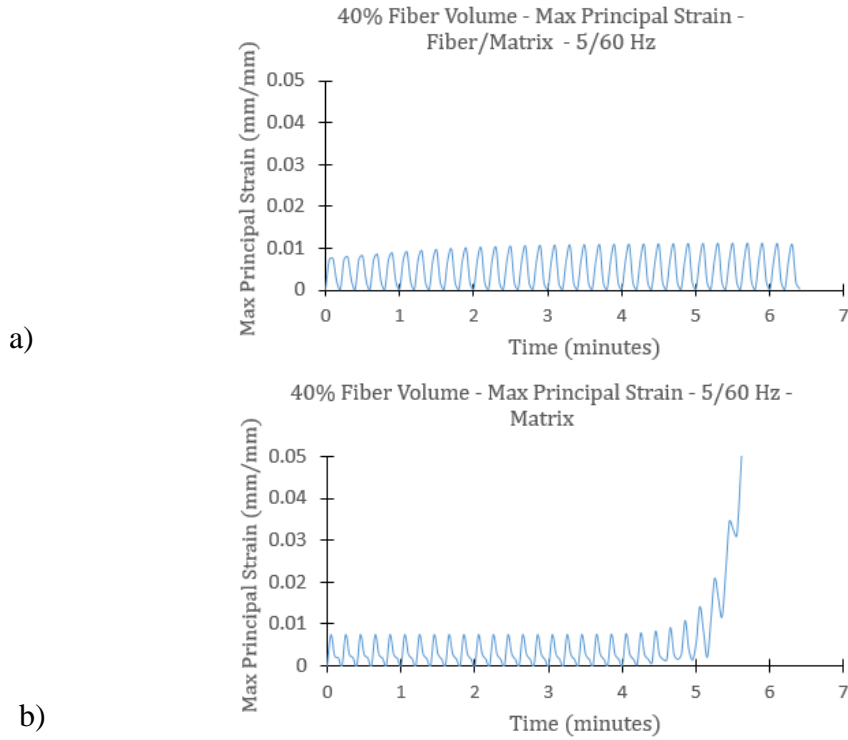


Figure 20 40% Fiber Volume – 5/60 Hz - Max Principal Strain – a) Fiber/Matrix b) Matrix

The hysteresis plots for both locations, matrix/fiber and matrix reflect the large deformations occurring in the matrix. Figure 21 are the hysteresis plots for both matrix/fiber and matrix. Both locations' E33 strains initially oscillates between 0.75% and -0.75% which is the displacement amplitude applied. The strain in the matrix/fiber remains bound within -1 and 1% but the normal strain in the matrix region increases rapidly at the 5-minute mark until the fiber volume model fails to converge.

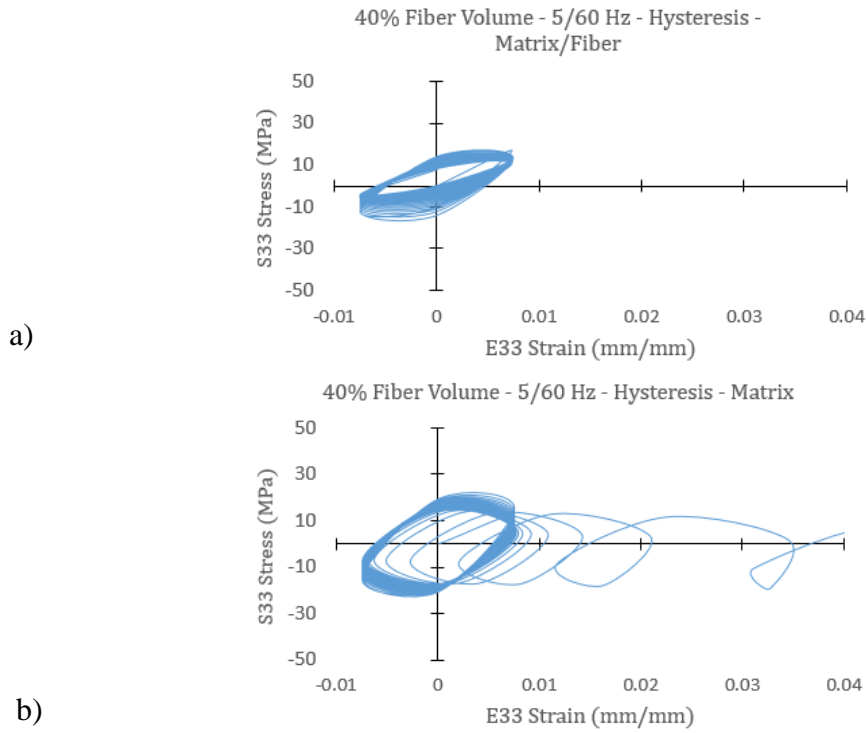


Figure 21 40% Fiber Volume – 5/60 Hz - Hysteresis – a) Fiber/Matrix b) Matrix

Similar to the case with frequency 5/60 Hz, the analysis under frequency 10/60 Hz failed to converge after 6.85 minutes of loading. Large deformations in the polymer regions are similar to the deformations in the 5/60 Hz polymer region. Figure 22 indicates large strain deformation in the polymer region. The maximum principal strain is 93.72%. The maximum principal strain vs. time plots for the 10/60 Hz cyclic loaded fiber model are given in Figure 23. In contrast to a case under frequency 5/60 Hz, the matrix/fiber strain is initially smaller (0.4% vs. 0.8%) and steadily increases through the load sequence. Also shown is the principal strain for the polymer matrix element. The maximum principal strain is less than 0.2% throughout the initial 5 minutes of loading. The strain increases rapidly after 5 minutes, reaching a maximum strain of 93.72 % after 6.85 minutes. We presume that the polymer matrix fails well before the 93.72% since customary strain failures are around 5-7% strain. From this analysis, it can be seen that high stress/strain localized within the microstructure of composites could initiate damage that leads to failure in composites.

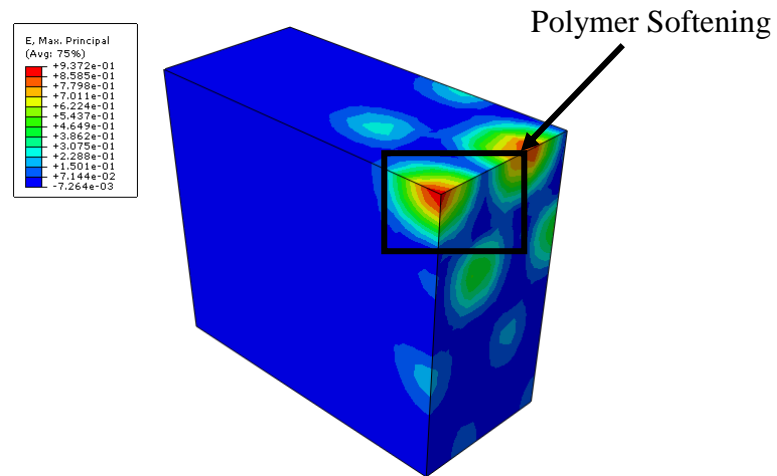


Figure 22 40% Fiber Volume – 10/60 Hz – Max Principal Strain – 6.85 minutes

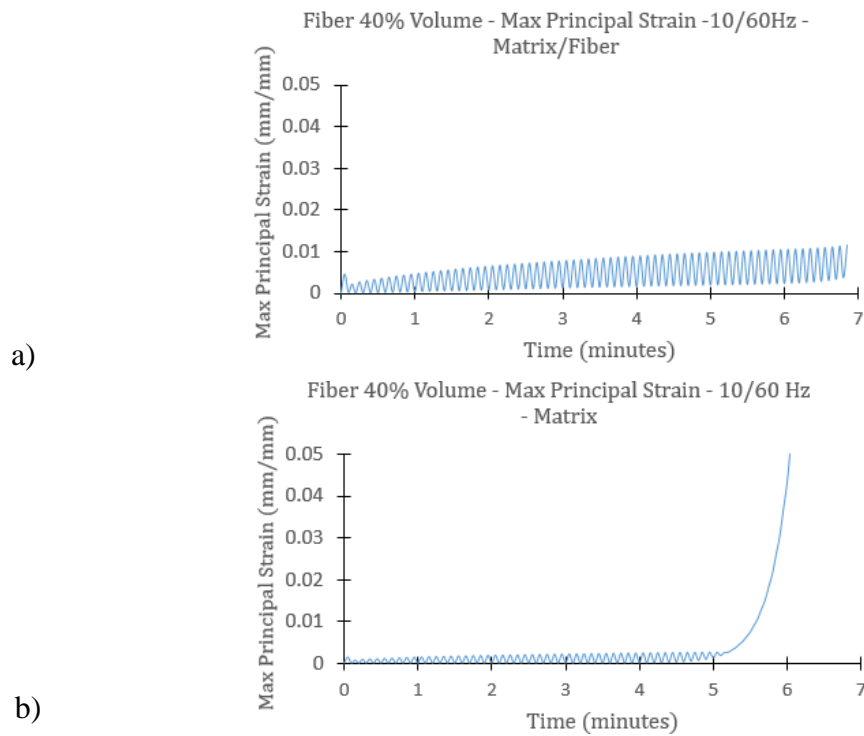


Figure 23 40% Fiber Volume – 10/60 Hz - Max Principal Strain – a) Matrix/Fiber b) Matrix

The loadings under frequency 5/60 Hz and 10/60 Hz are similar because the hysteresis behavior for the matrix are similar. Figure 24 is the hysteresis in the matrix region for the sample under 10/60 Hz frequency. The matrix' E33 strain continuously increases throughout the load cycle until the polymer matrix fails.

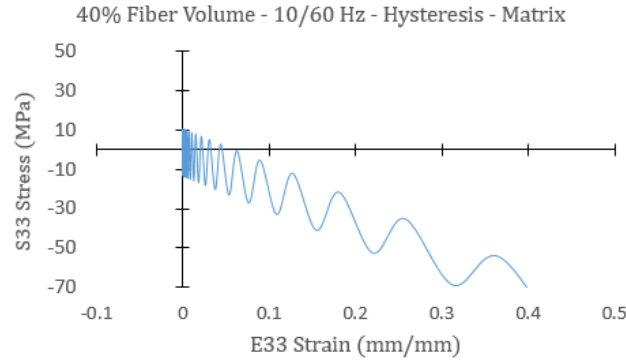


Figure 24 40% Fiber Volume - 10/60 Hz - Hysteresis – Matrix

Comparing the response due to 5/60 Hz and 10/60 Hz load sequence, both show that the arrangement of the fibers force matrix softening to occur in regions distance from fibers. Furthermore, the principal strains are initially higher in the matrix, bordering the fibers. However, the fibers also prevent excess nonlinear deformation at higher temperatures which is confirmed by Figure 20 and Figure 23. Comparing temperature increases within the models, the loading under frequency 10/60 Hz reaches higher temperatures after the same load duration. The case with 10/60 Hz reaches a maximum temperature of 323 K and the 5/60 Hz case reaches a maximum temperature of 319.7 K. Figure 25 shows the temperature vs. time plots for both analyses under frequency 5/60 Hz and 10/60 Hz.

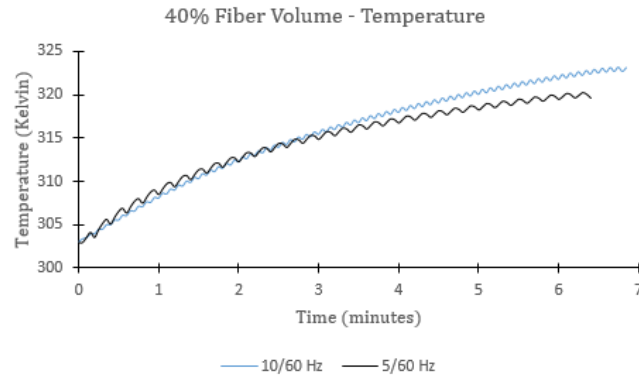


Figure 25 40% Fiber Volume - Frequency Study – Temperature

Figure 26 plots the maximum principal strain versus temperature for the composite model with 40% fiber content subjected to 5/60 Hz and 10/60 Hz cyclic frequency. For the model cycled at 5/60 Hz, the principal strain has an upper bound of 1.12% until the temperature reaches approximately 318 Kelvin. Subsequently, the strain rises and exceeds more than 5% at 320 Kelvin. In contrast, the principal strain for the fiber content model cycled at 10/60 Hz is at approximately 0.02% and is at steady state. At 323 Kelvin, the maximum principal strain increases rapidly to 5.17%. The models do not show the same strain rate behavior with respect to frequency even though they have the same geometry. Yet both models undergo large strain deformations at approximately 320 Kelvin. Comparing the max principal strain vs. temperature to the matrix/fiber location (shown in Figure 17), it is evident that the pure matrix regions' principal strains are more susceptible to temperature changes.

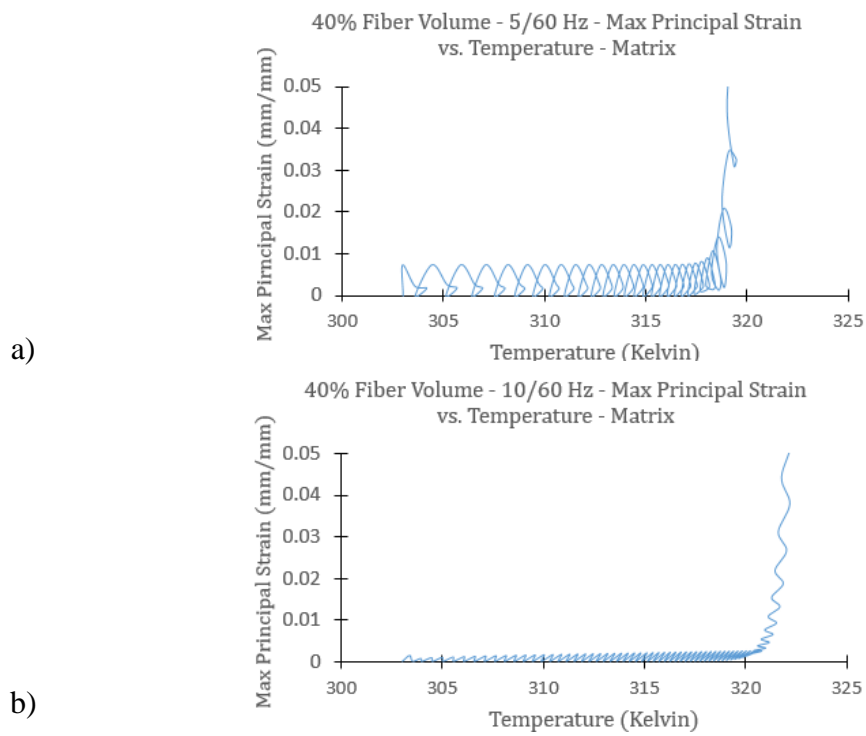


Figure 26 40% Fiber Volume - Max Principal Strain vs. Temperature - a) 5/60 Hz b) 10/60 Hz

6 THE EFFECT OF LOADING DIRECTION ON TEMPERATURE CHANGE (PRISTINE MODELS)

6.1 Shear Loading of Pristine Fiber Volume Models

The CFRC is most susceptible to polymer softening near locations where stress concentrations are pronounced such as the edges and small regions in the matrix between fibers. Polymer softening leads to large deformations which can contribute to damage/failure in composites. Within the numerical simulation, excessive matrix deformation is the source of divergence in the solutions. The strain deformation at the edges can be attributed to a combination of load direction and boundary condition. The 40% fiber volume, is cycled in simple shear with a 0.01 mm displacement amplitude applied to the front face of the model. This corresponds to 1% E13 shear strain. The direction of loading is along the 1-direction or x-axis. Additional details regarding load direction can be found in Section 3.3 which describes the load directions and boundary conditions. The cyclic frequency for the pristine shear models is 2/60 Hz. Figure 27 is the max principal stress plot for the 40% fiber volume sample. Visible are the fibers and stress concentrations around the respective fibers. Also, three regions namely Matrix/Fiber, Matrix 1 and Matrix 2 locations are investigated. The three locations of interest are found in Figure A-11 in the appendix. It should be noted that the locations of severe strains/stresses depend on the microstructural arrangements in addition to loading conditions.

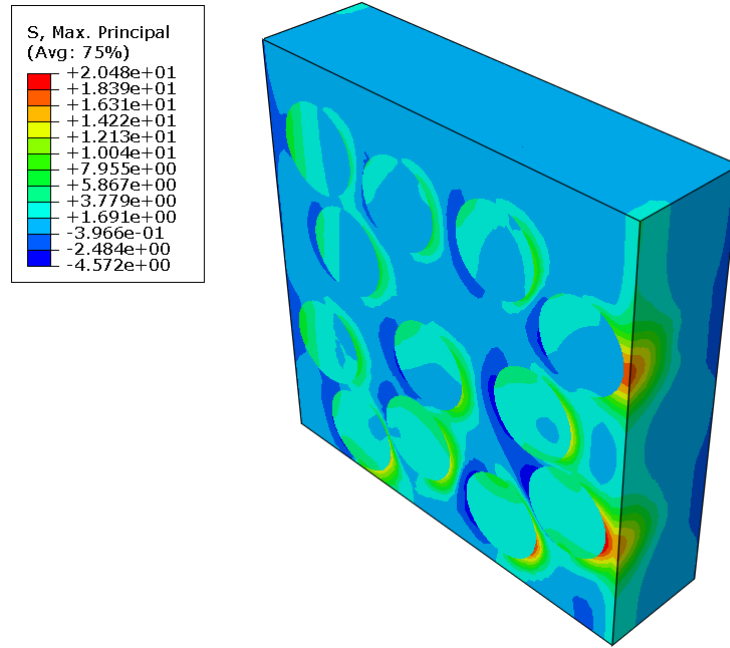


Figure 27 40% Fiber Volume - Pristine - Shear Loading - Max Principal Stress - 3.5 minutes

The principal strain plots for the three regions are shown in Figure 28. Principal strains for the matrix/fiber region are 2% and do not increase. The principal strain for matrix 1 is at 0.7% and the principal strain rises to 1.07% until the analysis fails to converge at 17 minutes and 30 seconds. Figure 28 c) is the principal strain plot for Matrix 2. Matrix 2, which is the polymer at the edge region undergoes the largest deformation. At 13.5 minutes, the principal strain is 10% and continues to increase until mesh distortion becomes too pronounced.

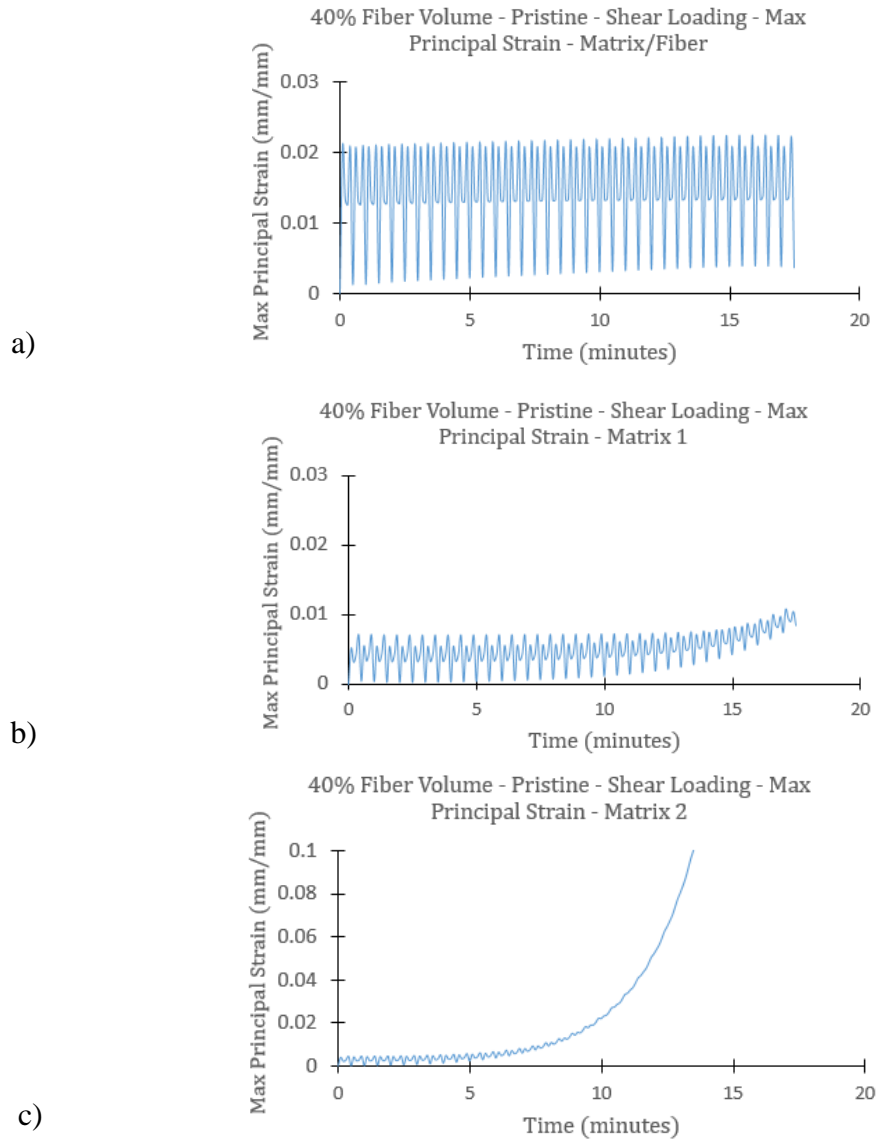


Figure 28 40% Fiber Volume - Pristine - Shear Loading - Max Principal Strain a) Matrix/Fiber b) Matrix 1 c) Matrix 2

The hysteresis response can be divided into a shear hysteresis response and a normal strain hysteresis response. The shear hysteresis response, which plots the shear strain E_{13} and shear stress S_{13} against each other shows linear-elastic behavior. The shear hysteresis response plots are attached to the Appendix, Figure A-12 through Figure A-14. However, evaluating the strain components individually, the hysteresis response has significant normal strains (E_{33}) and stresses (S_{33}). Figure 29 are the hysteresis plots for

the three locations. The matrix/fiber hysteresis trace is ellipsoidal and the normal strains vary between 0.5% and -0.5%. Furthermore, comparing the matrix/fiber's normal strains to Matrix 1's normal strains, they are greater in magnitude initially (see Figure A-11 for locations). In contrast to matrix/fiber hysteresis' fairly linear behavior, the normal strain in matrix 1 increases throughout the loading cycle and reaches 0.974% at 17 minutes and thirty seconds. Yet, the largest increases in strains occur in the matrix 2 location. In Figure 29 c), which is the matrix 2 hysteresis plot, the hysteresis trace does not form closed ellipsoids but the normal strain and normal stress continues to rise during the load cycle.

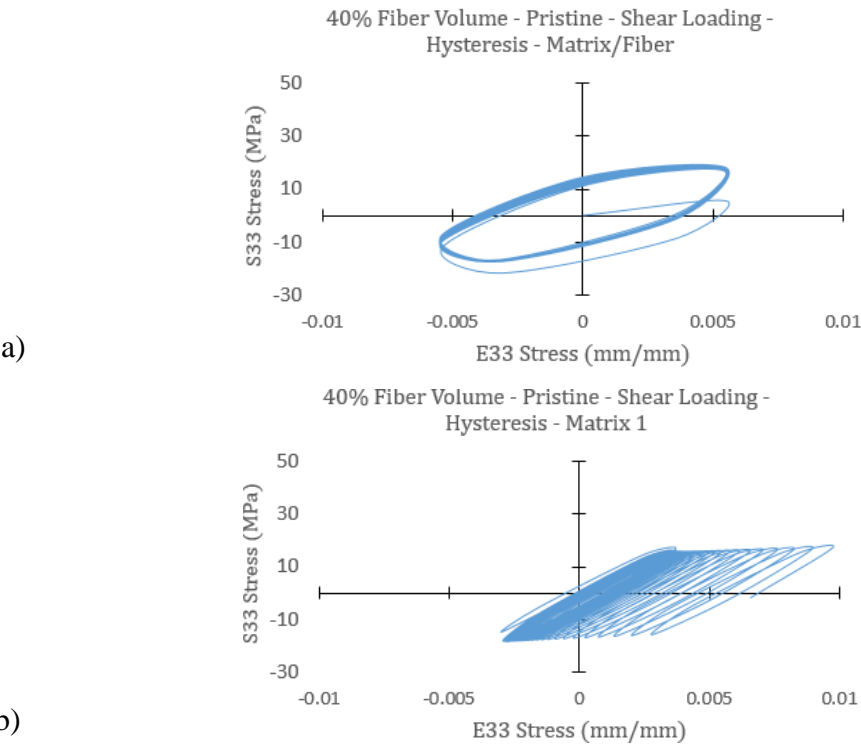


Figure 29 40% Fiber Volume - Pristine - Shear Loading – Hysteresis

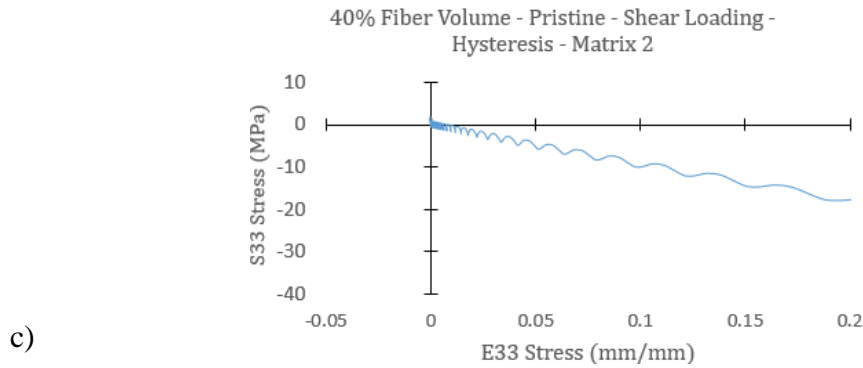


Figure 29 continued

The 50% fiber volume's microstructural field variables are dependent on the location in the 50% fiber volume sample. Figure A-15 in the appendix highlights the regions of interest. Principal strains are higher in the matrix/fiber region initially yet principal strains increase faster in the pure matrix 1 and matrix 2 region. The principal strain for the matrix fiber region reaches 0.99% at 20 minutes and reduces to 0.245% during the 5 minute recovery period. The principal strain in matrix 1 is at 0.625% and rises to 0.88% at 20 minutes. For the matrix 1 location, the 50% fiber volume model continues to creep during the recovery period. At last, the matrix 2 location has the highest change in principal strain: Principal strain increases from 0.686% to 1.25% at 20 minutes. The matrix 2 principal strain rises during the recovery period and reaches 2.41% at 25 minutes. Figure 30 are the principal strain plots for all three locations. For the hysteresis plots, the shear strain/stress hysteresis plots show linear viscoelastic dissipation behavior. . The shear strain hysteresis plots are found in the Appendix, Figure A-16 through Figure A-18.

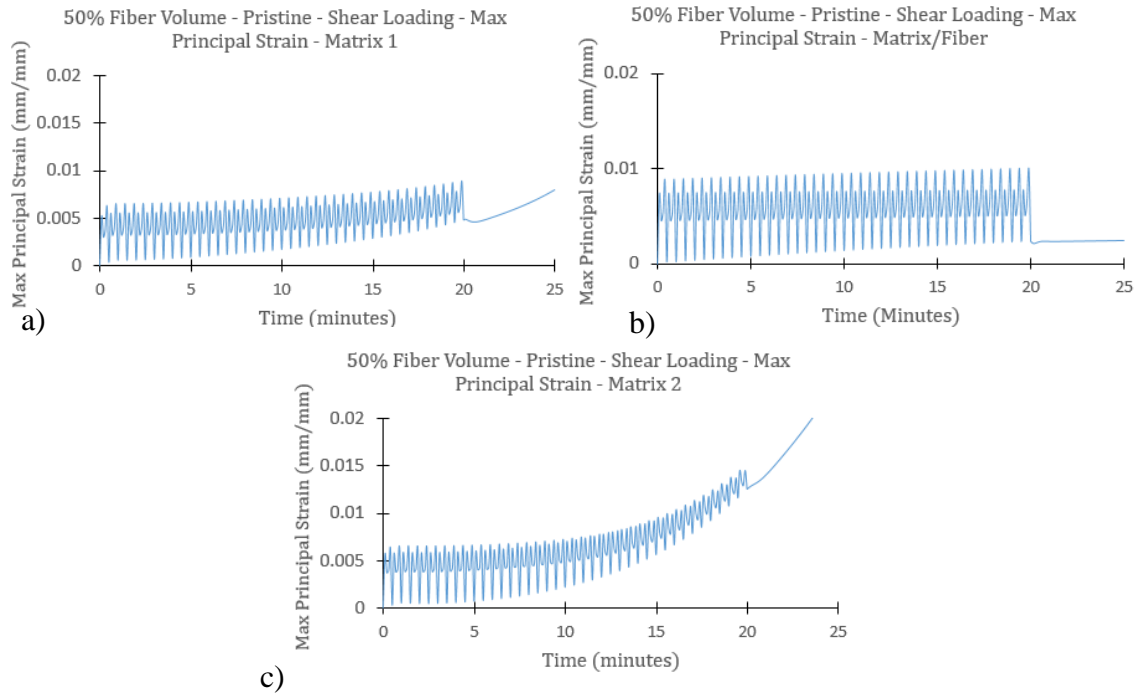


Figure 30 50% Fiber Volume - Pristine - Shear Loading - Max Principal Strains a) Matrix 1 b) Matrix/Fiber c) Matrix 2

The normal strain/stress hysteresis plots for all three locations, namely matrix/fiber, matrix 1 and matrix 2 are shown in Figure 31. Noteworthy is that the hysteresis plots have low stress amplitudes which vary between +5 and -5 MPa. Figure 31 b) and c) are the matrix 1 and matrix 2 hysteresis plots. In contrast to the matrix/fiber hysteresis plot, the normal strain levels continue to increase during loading, reaching 0.788% and 2.04% for matrix 1 and matrix 2 respectively.

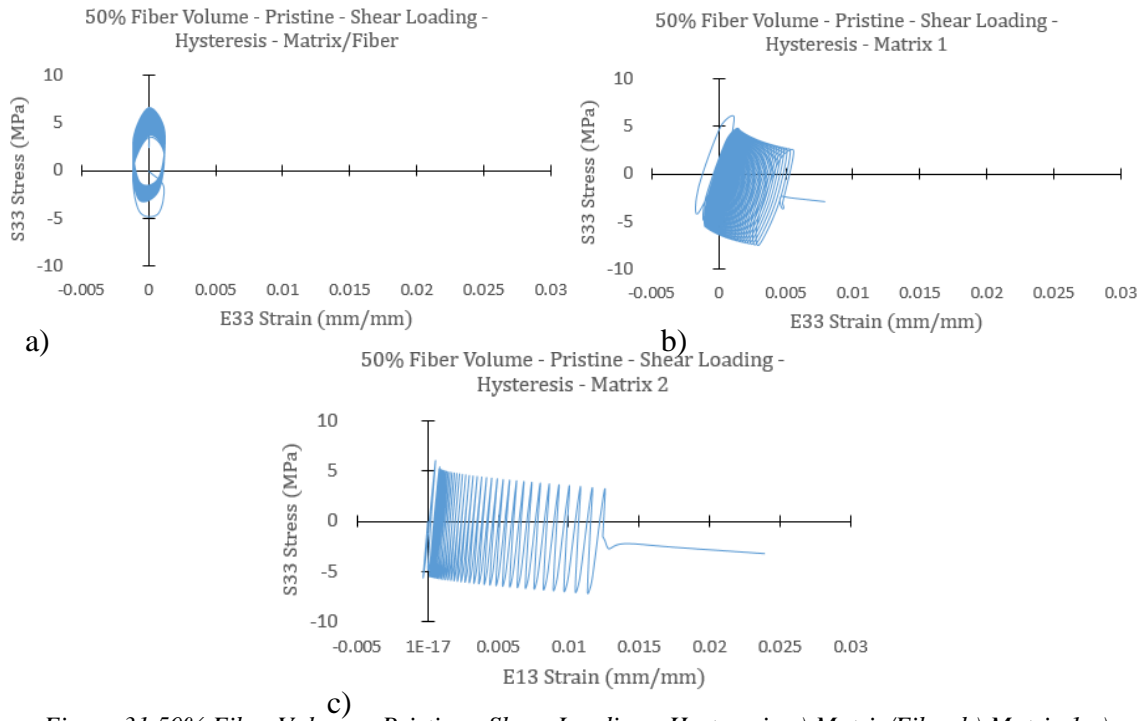


Figure 31 50% Fiber Volume - Pristine - Shear Loading - Hysteresis a) Matrix/Fiber b) Matrix 1 c) Matrix 2

In the composite with 60% fiber volume content, fibers are arranged in a hexagonal pattern and the principal strains in the regions of interest behave similarly as the composites with 50% and 40% fiber volume contents. Again, three regions which we label as matrix/fiber, matrix 1 and matrix 2 are investigated. Figure A-19 in the appendix, is a principal stress plot of the 60% fiber volume model and labels the respective regions. The principal strain plots for all three regions is shown in Figure 32 and confirms the patterns observed in the composites with 40% and 50% fiber volume contents: Matrix/fiber regions are at higher strains initially but unconfined, i.e. not tightly surrounded by fibers, are susceptible to greater deformation during shear loading. For matrix 1, the principal strain reaches a maximum of 0.81% principal strain. Matrix 2's principal strain rapidly increases to 7.72% and creeps during the 5 minute recovery period. At 25 minutes, the principal strain reaches 9.11%. In comparison, the matrix/fiber strain oscillates steadily and recovers to 0.196% during the recovery period.

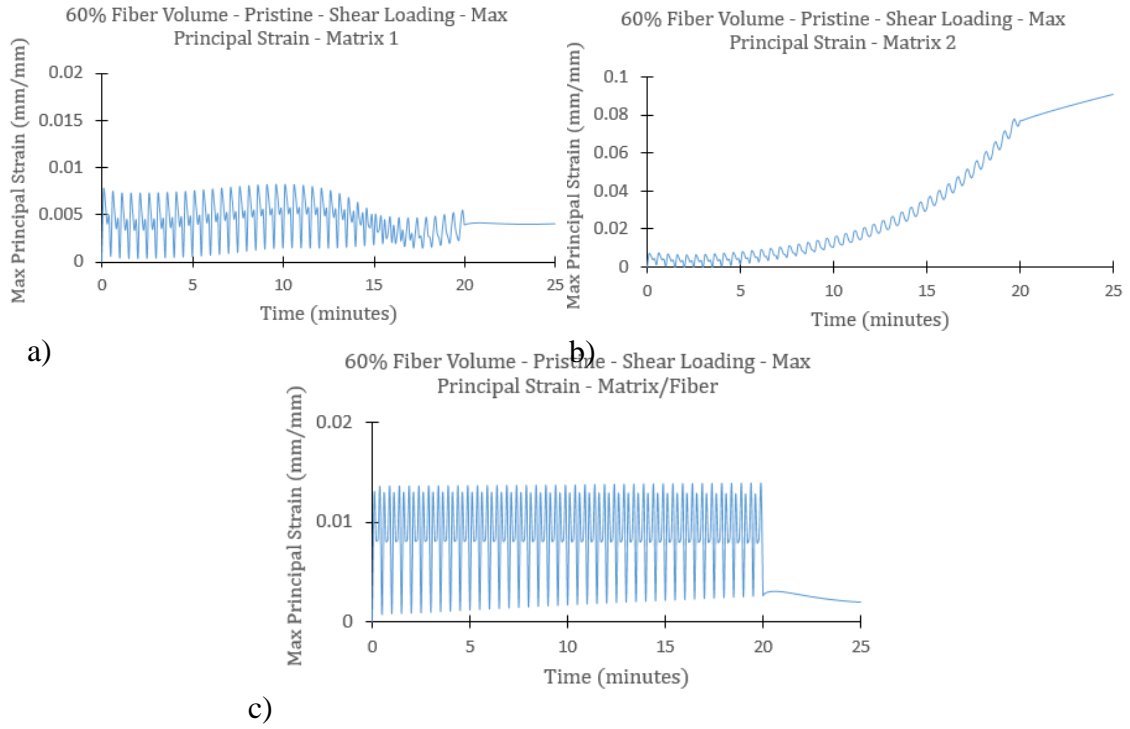


Figure 32 60% Fiber Volume - Pristine - Shear Loading - Max Principal Strains a) Matrix 1 b) Matrix 2 c) Matrix/Fiber

Although the 60% fiber volume model is cycled in simple shear, the normal strain E33 is significant. The normal stress is below 20 MPa for all three locations. However, matrix 1 reaches -4.71% compressive strain and matrix 2 reaches 8.98% normal strain. Figure 33 are the normal strain/stress hysteresis plots for all three locations.

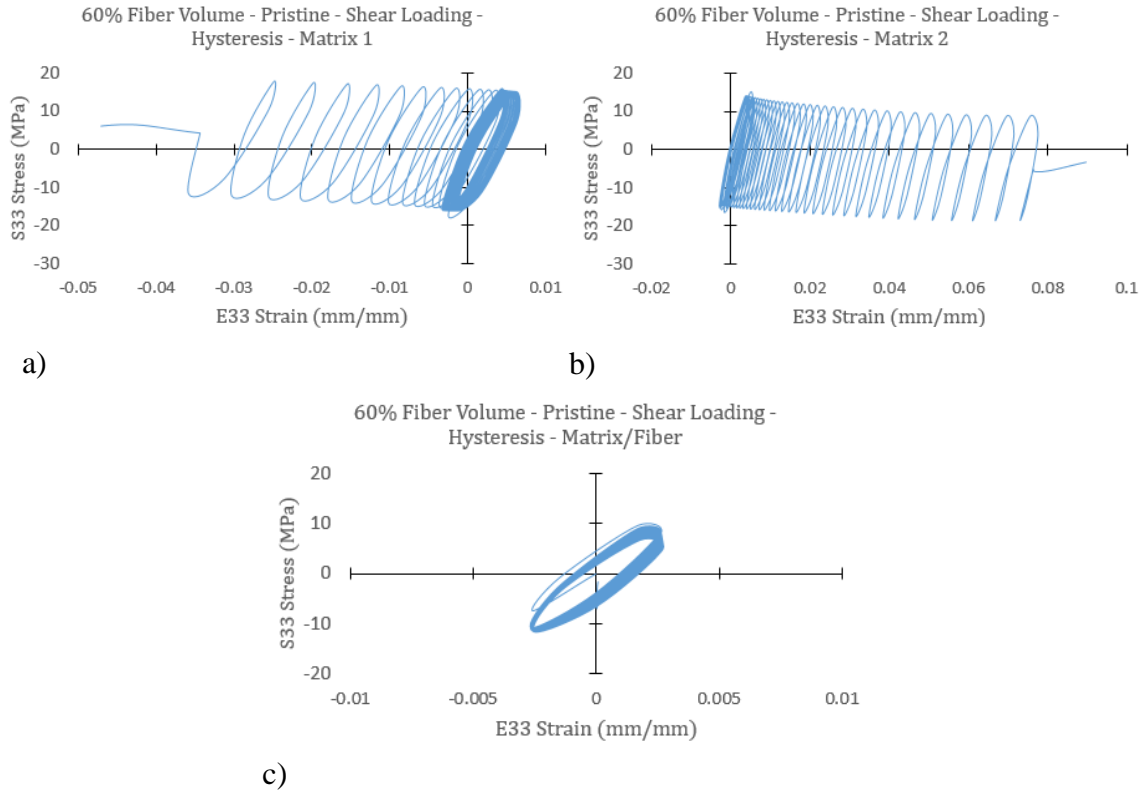


Figure 33 60% Fiber Volume - Pristine - Shear Loading – Hysteresis a) Matrix 1 b) Matrix 2 c) Matrix/Fiber

For the temperature change in the pristine shear loaded models, Figure 34 is the temperature plot for the models. The graph shows a correlation between fiber volume and temperature increase. At the same displacement amplitude (0.01 mm), the composite with 60% fiber volume content experiences the highest temperature increase followed by the composite with 50% and the 40% fiber volume contents, respectively. The model with 60% fiber volume content shows the temperature increase to 312.52 Kelvin. The model with 50% fiber volume content shows the final temperature of 310.94 Kelvin. Following the trend, the 40% fiber volume's internal temperature reached 308.14 Kelvin at 17 minutes and thirty seconds.

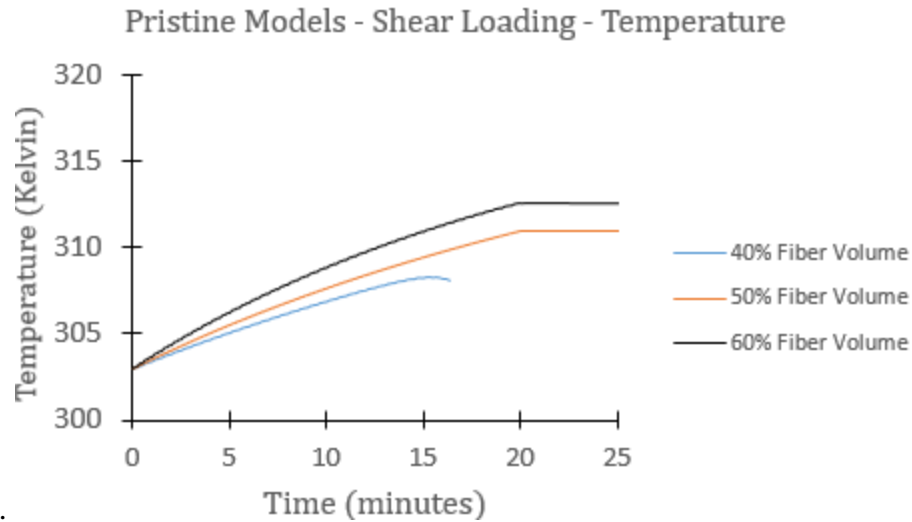


Figure 34 Pristine - Shear Loading – Temperature

The principal strains are plotted in Figure 35. For the same displacement amplitude applied (0.01 mm or 1% strain), the temperature increase during shear loading is less than the temperature increase for longitudinal loading. However, even a temperature increase from 303 Kelvin to 311 Kelvin causes an increase in principal strains because the heat softens the polymer. In the appendix, Figure A-20 through Figure A-23 show the temperature distribution for the 50% fiber volume for four time steps: 1 minute, 5 minutes, 10 minutes and 20 minutes. From Figure 35, the matrix/show minimal strain increase with respect to temperature increase. In contrast all the matrix 2 locations are sensitive to the temperature changes. Table 8 shows individual principal strain values at 305 Kelvin, 307 Kelvin and 312 Kelvin. For the 40% fiber model, only the principal strains at 305 Kelvin and 307 Kelvin are recorded because the model did not reach higher temperatures. The strain increase depends on both temperature and microstructural fiber arrangements, however, all models show that the temperature affects the principal strain by softening the polymer matrix.

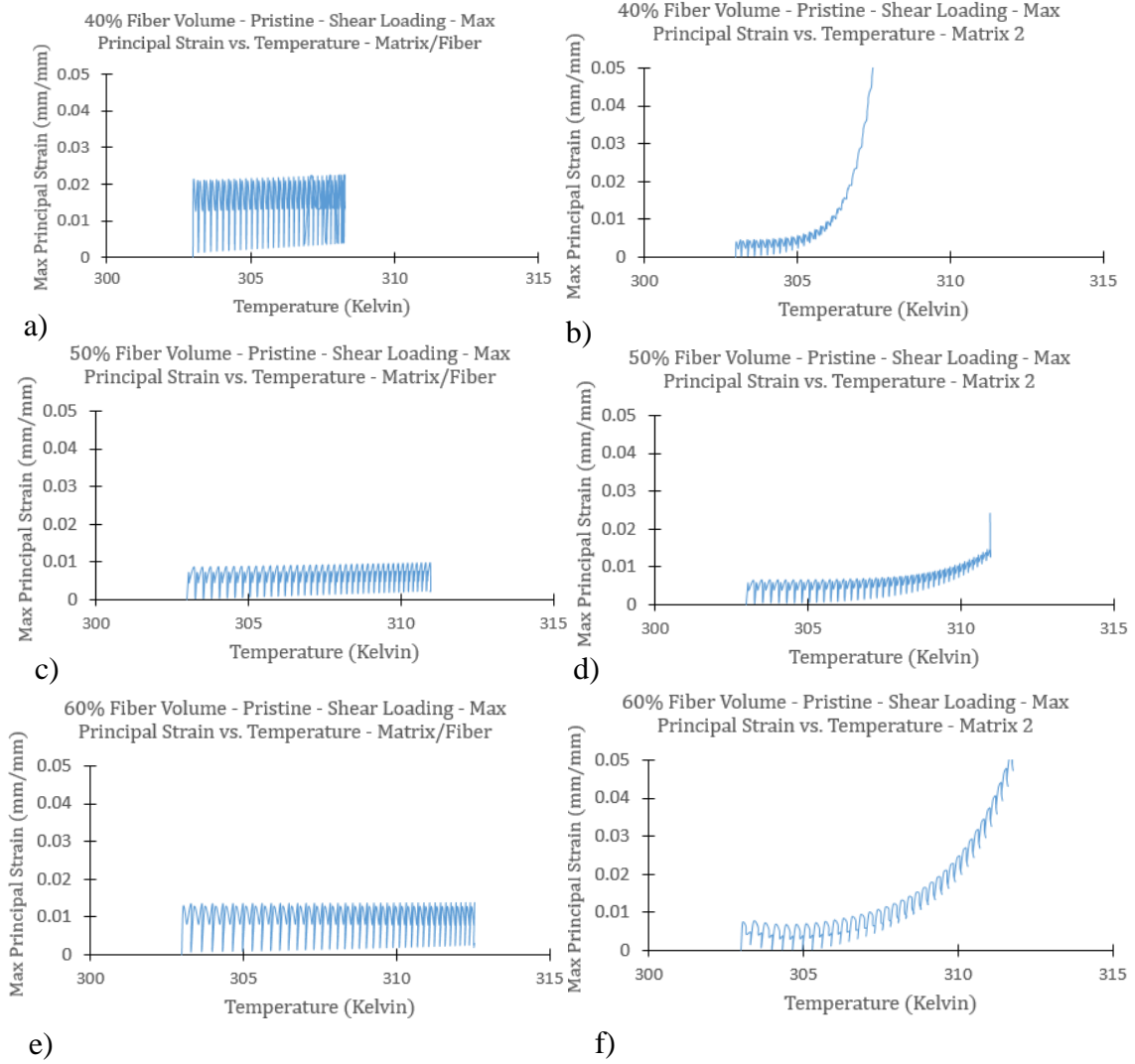


Figure 35 Max Principal Strain vs. Temperature – Shear Loading – Pristine - a) 40% Fiber Volume – Matrix/Fiber b) 40% Fiber Volume – Matrix 2 c) 50% Fiber Volume – Matrix/Fiber d) 50% Fiber Volume – Matrix 2 e) 60% Fiber Volume Matrix/Fiber f) 60% Fiber Volume – Matrix 2

Table 8 Max Principal Strain vs. Temperature - Pristine Models - Shear Loading

Fiber Volume		40%		50%		60%	
Location		Matrix/Fiber	Matrix 2	Matrix/Fiber	Matrix 2	Matrix/Fiber	Matrix 2
Temperature	305K	2.13%	0.57%	0.65%	0.65%	1.29%	0.68%
	307K	2.22%	5.59%	N/A	N/A	N/A	N/A
	312K	N/A	N/A	1.07%	1.07%	1.37%	9.11%

6.2 Transverse Loading of Pristine Composite Models

Three fiber configurations (40%, 50% and 60%) are cycled at frequency 3/60 Hz and loaded along the transverse fiber direction. The objective is to investigate the temperature increase and the micromechanical field variables (stress, state) and compare them to the longitudinal and shear loading. In contrast to the longitudinal and shear configuration models, the transverse loading configurations have four fibers only to reduce the computational time. Figure 36 is the model with 40% fiber volume content subjected to transverse loading configuration. The local coordinate system is shown. For the transverse loading cases, 80 MPa traction is applied for the 40% and 50% fiber configuration. A 60 MPa traction is applied on the left face of the 60% fiber volume to achieve numerical convergence.

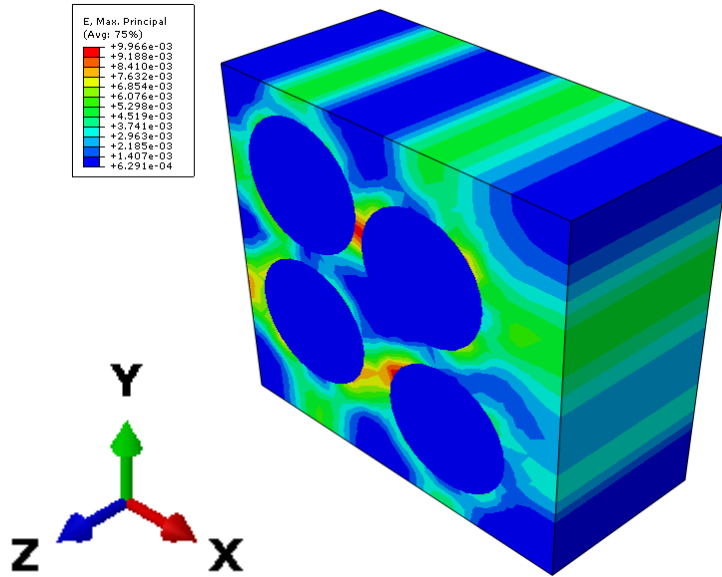


Figure 36 40% Fiber Volume - Pristine - Material Orientation

Similar to the longitudinal load cases, strain concentrations occur in the polymer matrix, directly neighboring adjacent fibers. Figure 37 show three regions in the polymer matrix which will be analyzed in depth: Matrix/Fiber 1, Matrix/Fiber 2 and Matrix.

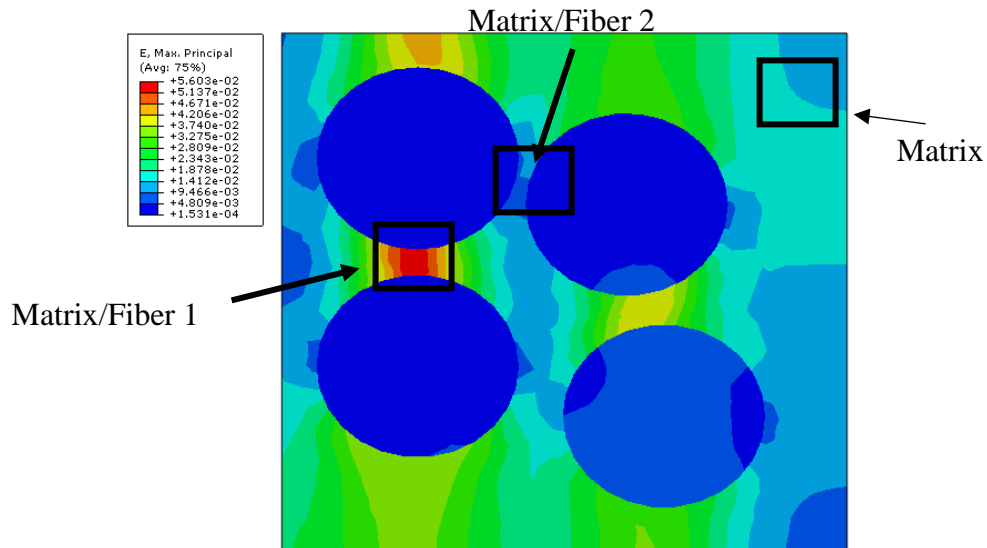


Figure 37 40% Fiber Volume - Transverse – Maximum Principal Strain - 1.1 minute

In general, Matrix/Fiber Location 1 and Matrix/Fiber Location 2 have strain concentrations. However, after 30 minutes of cyclic loading, the Matrix location shows the greatest strain deformation. The principal strain oscillates between 0% and 2% but increases rapidly at 27 minutes until it reaches a maximum principal strain of 5.89%. Figure 38 shows the principal strain versus time for the matrix location. To compare, Matrix/Fiber 1 location has a maximum principal strain of 5.98% and Matrix/Fiber 2 location reaches 2.47% principal strain. Figure 39 are the two principal strain plots for both Matrix/Fiber 1 and Matrix/Fiber 2 location. Softening of the polymer matrix occurs in fiber-less regions. Figure A-39 in the appendix shows the principal strain and regions of matrix softening at 30 minutes for the 40% fiber volume configuration.

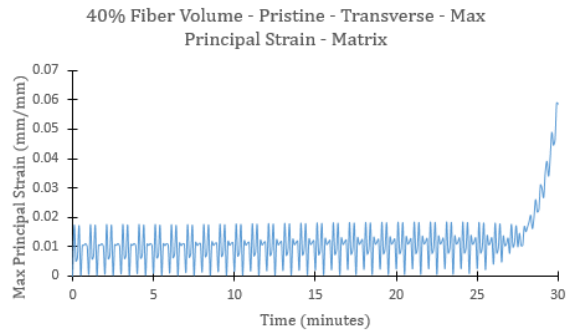


Figure 38 40% Fiber Volume - Transverse - Max Principal Strain – Matrix

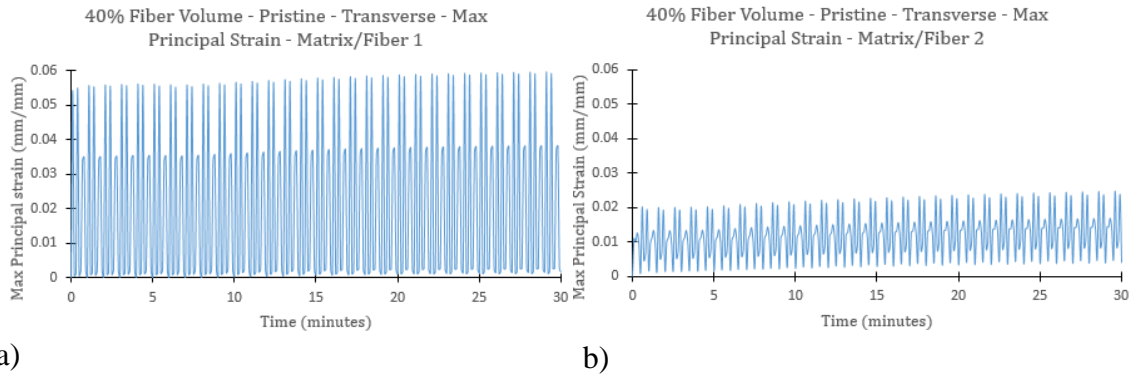


Figure 39 40% Fiber Volume - Transverse - Max Principal Strain a) Matrix/Fiber 1 b) Matrix/Fiber 2

The 50% fiber volume geometry configuration is given in Figure 40. The 60% fiber configuration is shown in Figure A-26 which is located in the appendix. In addition to showing the actual fiber geometry, both Figure 40 and Figure A-26 also highlight the regions of interest such as matrix/fiber region or matrix region. From previous observation of the 40% fiber configuration, the strains are higher near the fiber to matrix interface.

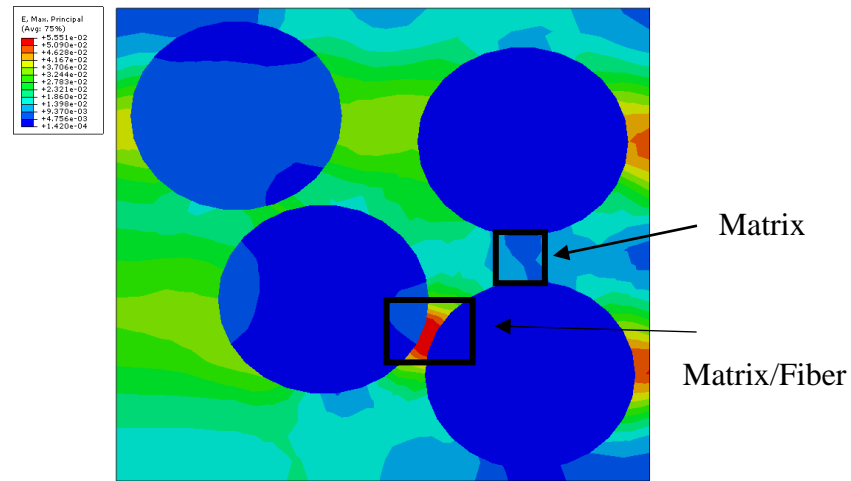


Figure 40 50% Fiber Volume - Pristine - Transverse - Principal Strain

Figure 41 and Figure 42 are the principal strains for the matrix/fiber region of the composites with 50% and 60% fiber volume contents, respectively. The principal strains are 6.40% and 6.13% respectively and increase minimally throughout the 30 minute loading period. This is comparable to the principal strains in the 40% fiber volume configuration which is at 5.98% respectively.

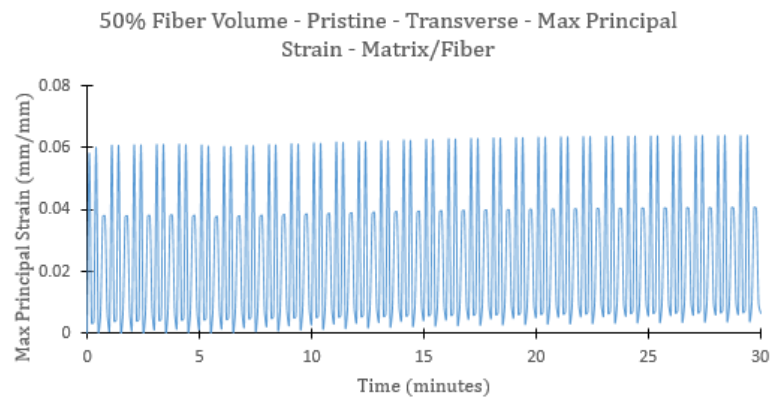


Figure 41 50% Fiber Volume - Pristine - Transverse Loading - Max Principal Strain - Matrix/Fiber

The secondary locations such as the matrix location in the composite with 50% fiber volume content and matrix/fiber 2 location in the composite with 60% fiber volume content have lower principal strains. In the composite with 50% fiber volume content, the matrix location reaches 1.34% max principal strain and in the 60% fiber volume content, the matrix/fiber 2 location reaches 1.19%. The principal strain plots are shown in Figure A-27 and Figure A-28 in the appendix.

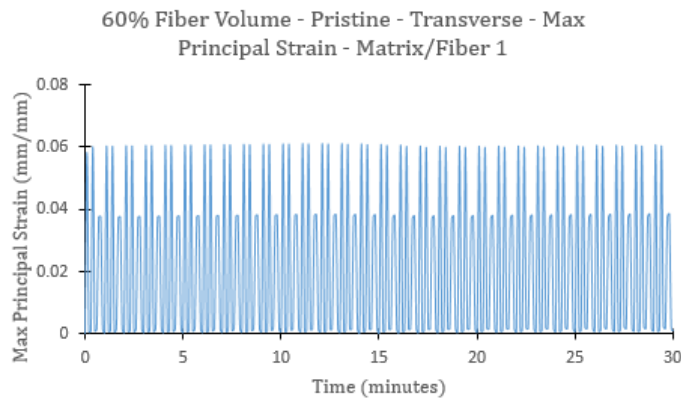


Figure 42 60% Fiber Volume - Pristine - Transverse Loading - Max Principal Strain - Matrix/Fiber 1

In all three fiber configurations, the macroscopic stress-strain hysteresis are ellipsoidal in behavior. For the 40% fiber volume, at the matrix/fiber 1 location, the maximum and minimum E22 strains are 5.98 % and -5.65 %. The maximum and minimum S22 stresses are 199.185 MPa and -191.812 MPa. The maximum hysteresis stress and strain values for the locations listed in Table 9. The normal strains vary 5.98 % to 6.40% and normal stresses vary from 199.19 MPa to 221.99 MPa for the individual fiber configurations. The corresponding actual hysteresis cycles are plotted in Figure 43 and highlight the almost linear elastic behavior of the matrix near the adjacent fibers. The remaining hysteresis plots can be found in the appendix, Figure A-29 through Figure A-32.

Table 9 Pristine Fiber Models - Transverse Loading - Hysteresis Stresses and Strains

Fiber Volume	40%	50%	60%
Location	Matrix/Fiber 1	Matrix/Fiber	Matrix/Fiber 1
Max/Min Normal Strains (%)	5.98/-5.65	6.40/-6.14	6.09/-6.00
Max/Min Normal Stresses (MPa)	199.19/-191.81	209.77/-200.82	221.99/-215.49

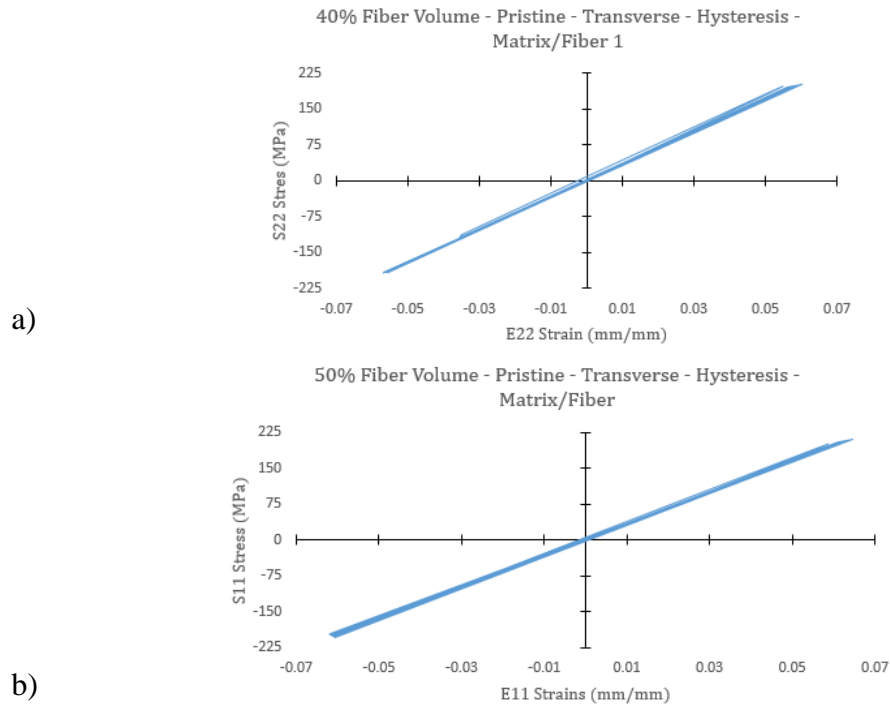


Figure 43 Pristine Configurations - Transverse - Hysteresis Plots a) 40% Fiber Volume b) 50% Fiber Volume c) 60% Fiber Volume

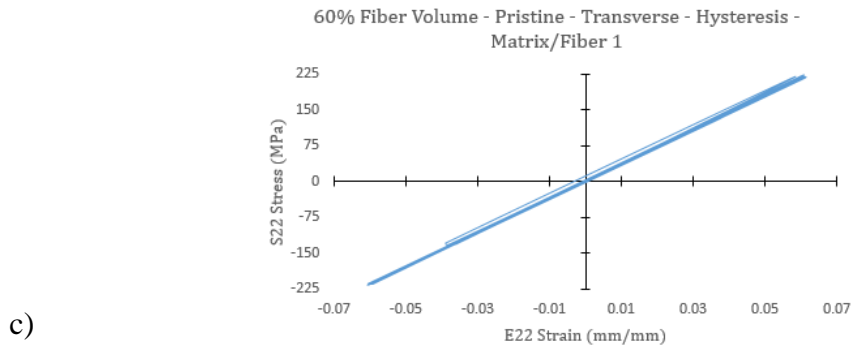


Figure 43 continued

The hysteresis cycle represents the amount of energy being dissipated. Since the localized hysteresis response for all three configurations are close to linear in behavior and no large-strain deformations occur, it is expected that the corresponding temperature increases should be smaller than temperature increases found in the longitudinal loading, which exhibited highly nonlinear localized hysteresis responses. The temperature increases for all three configurations reflect the hysteresis responses well. The 40% fiber volume model reached 316.4 Kelvin and the 50% fiber volume reached 316.7 Kelvin. In contrast, the 60% fiber volume simulation only reached 308.8 Kelvin after 30 minutes. This is consistent with the fact that 60 MPa was applied on the 60% fiber volume model. The 60% fiber volume model, when cycled with 80 MPa traction, has large strain gradients across fibers which causes convergence issues. Figure 44 is the temperature plot versus time for all three fiber volume configurations. The temperature vs. time plot furthermore reflects that temperature increases are more sensitive to an increase in traction load applied instead of a change in fiber volume. Overall, the temperature distribution is uniform throughout the models because they are loaded slowly and temperature conduction is allowed within each composite model. The temperature contours for the 50% fiber model are plotted for various time intervals in the appendix, Figure A-33 through Figure A-36.

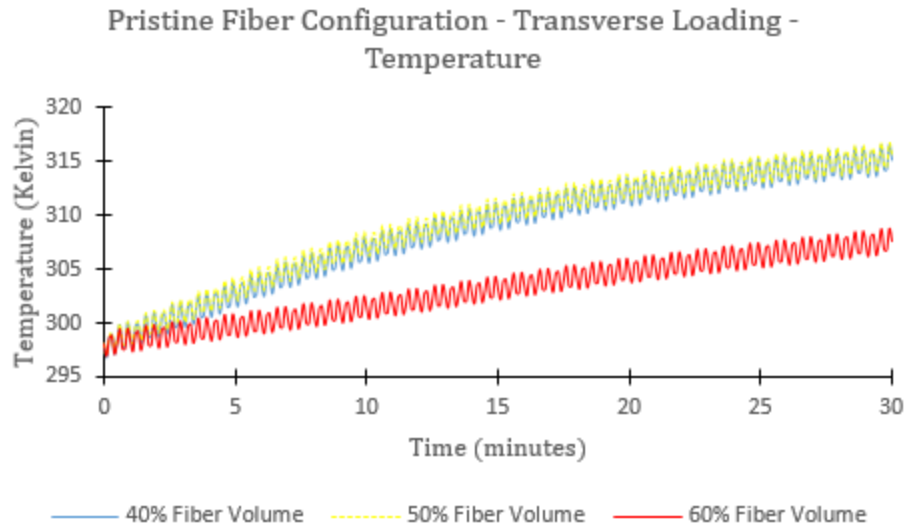


Figure 44 Pristine Configurations - Transverse Loading – Temperature

Figure 45 shows the principal strain versus temperature for the fiber models loaded in transverse direction. Overall, the transverse loaded fiber models are less sensitive to temperature changes than the fiber models loaded in the longitudinal direction or shear direction. The matrix/fiber principal strains are plotted for the composites with 40%, 50% and 60% fiber volume contents. Also, the matrix location principal strains are plotted for the composites having 40% and 50% fiber volume content. The 60% fiber model did not have any excessive matrix deformation because it was cycled at a lower load. The 40%, 50% and 60% fiber volume matrix/fiber polymer reached maximum principal strains of 2.37%, 6.40% and 1.05% respectively. In contrast, the matrix locations reached higher principal strains throughout the loading cycle.

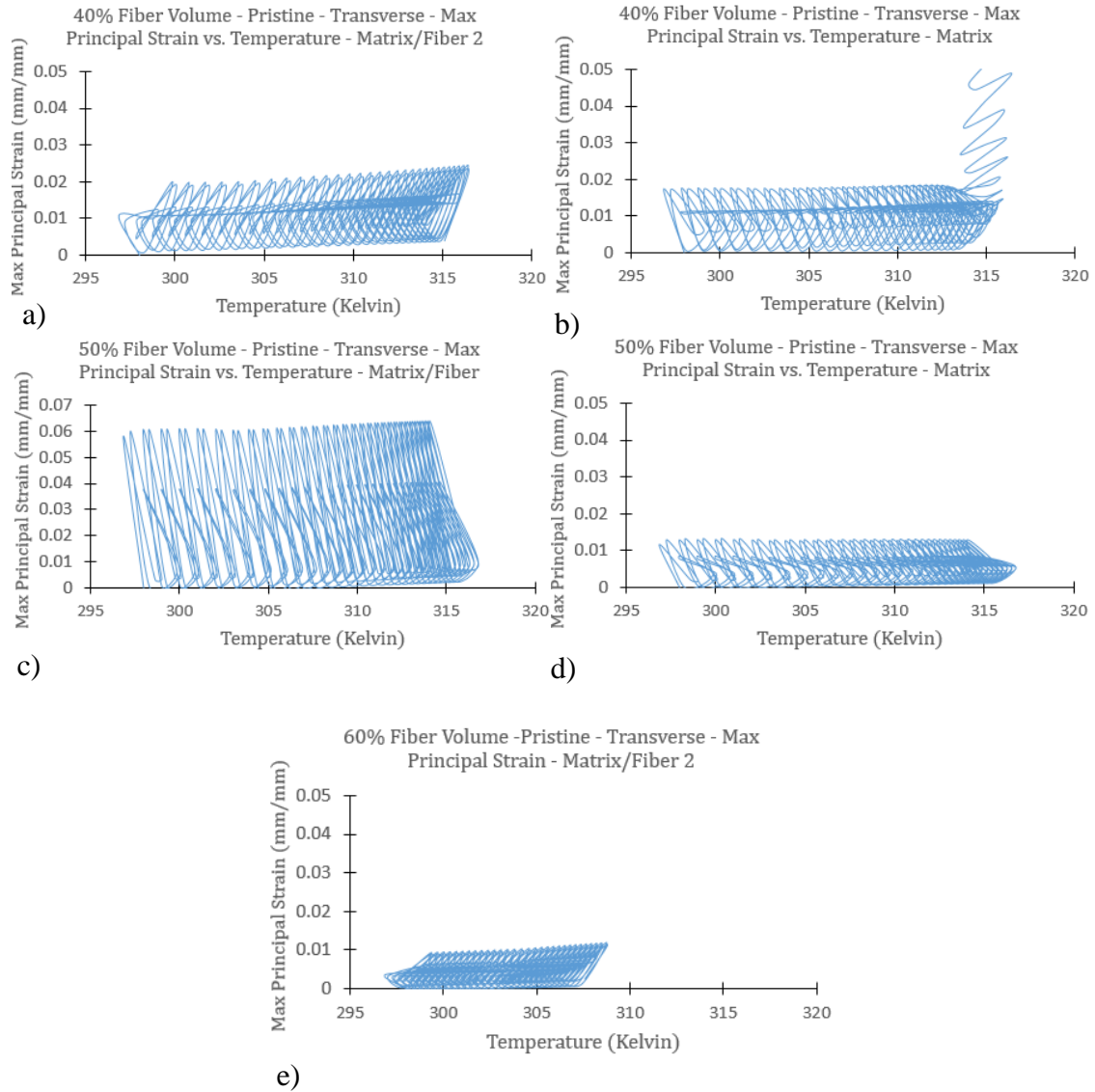


Figure 45 Max Principal Strain vs. Temperature – Transverse Loading – Pristine - a) 40% Fiber Volume Matrix/Fiber 2 b) 40% Fiber Volume Matrix c) 50% Fiber Volume Matrix/Fiber d) 50% Fiber Volume Matrix e) 60% Fiber Volume Matrix/Fiber 2

Table 10 shows the principal strains against the temperatures at 4 different temperatures. Note that the 60% fiber volume sample was cycled at a lower load (60 MPa) so only the matrix/fiber 2 location's principal strains are transcribed. In addition, the principal strains are lower in the 60% fiber volume.

Table 10 Max Principal Strain vs. Temperature - Pristine - Transverse Loading

Fiber Volume		40%		50%		60%
Location		Matrix/Fiber 2	Matrix	Matrix/Fiber	Matrix	Matrix/Fiber 2
Temperature (Kelvin)	300	2.00%	0.70%	6.07%	1.31%	0.92%
	305	2.08%	1.05%	6.03%	1.28%	1.05%
	310	2.24%	1.84%	6.25%	1.28%	N/A
	315	2.37%	5.85%	6.40%	1.30%	N/A

7 THE EFFECT OF VOIDS ON MATRIX DEFORMATION AND TEMPERATURE CHANGE

7.1 *Longitudinal Loading of Void Fiber Configuration Models*

Void geometry for composites with 40%, 50% and 60% fiber volume contents are created using a MATLAB script which distributes ellipsoidal voids randomly throughout the fiber geometry. The MATLAB script varies geometric dimensions including major and minor radius of the ellipsoidal voids. Additional geometric parameters varied include minimum spacing between voids and fibers to prevent finite element mesh distortion. For the 40%, 50% and 60% fiber content models, the void percentage for the fiber models are 0.26%, 0.35% and 0.23% respectively. The void content is held low to minimize computational time. Figure A-37 in the appendix shows the 40% fiber volume void model. Unless otherwise specified, the longitudinal models are cycled for 20 minutes at a frequency 2/60 Hz. The displacement amplitude applied is 0.01 mm. For the 40% fiber volume, void configuration, the polymer matrix deforms severely when it is cycled for 20 minutes at frequency 2/60 Hz. Three locations are identified that show elevated strain measures. For convenience, we label the locations matrix/fiber, matrix/void and matrix/edge. The matrix/edge refers to a polymer matrix region located adjacent to an edge. These regions either show stress concentrations such as the matrix/fiber location or undergo large deformations (matrix/void and matrix/edge location). Figure 46 is the fiber model at 0.400 min time step. The locations are labeled on the fiber model.

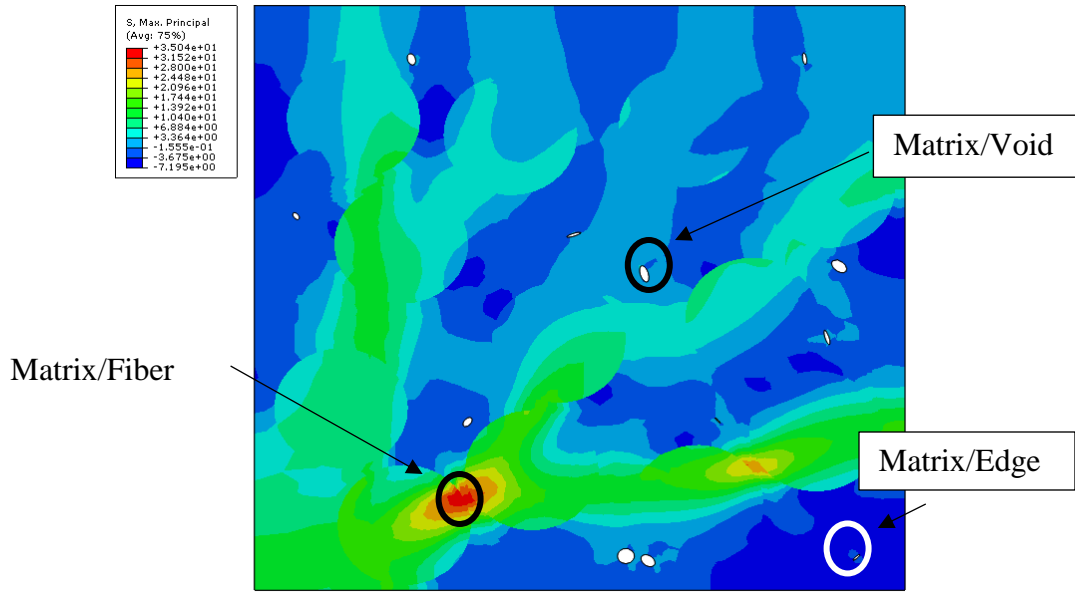


Figure 46 40% Fiber Volume - Longitudinal - Max Principal Stress – 0.400 minutes

Figure 47 shows the maximum principal strains for all three regions of interest. The maximum principal strain is 2.04%. In contrast, the matrix/void and matrix/edge locations' maximum principal strains are 10.12% and 20.16% at 20 minutes. The matrix/void and matrix/edge location principal strains stay below 1% strain initially and the principal strain rapidly increases at the 15 minute mark. Figure 47 shows the principal strain plots for both the matrix/void and matrix/edge locations. In addition, Figure A-40 and Figure A-41 provide additional insight in the region of significant polymer softening. The hysteresis loops for the matrix/void and matrix/edge are plotted in Figure 48.

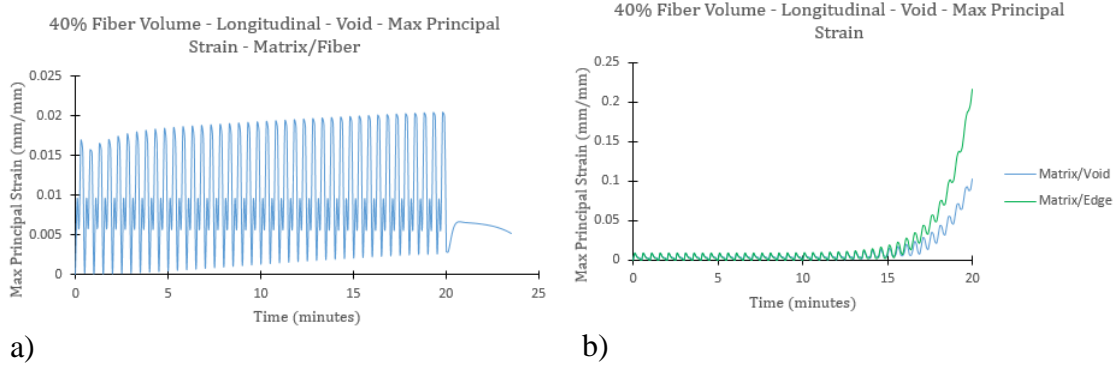


Figure 47 40% Fiber Volume - Longitudinal - Max Principal Strain a) Matrix/Fiber b) Matrix/Void and Matrix/Edge

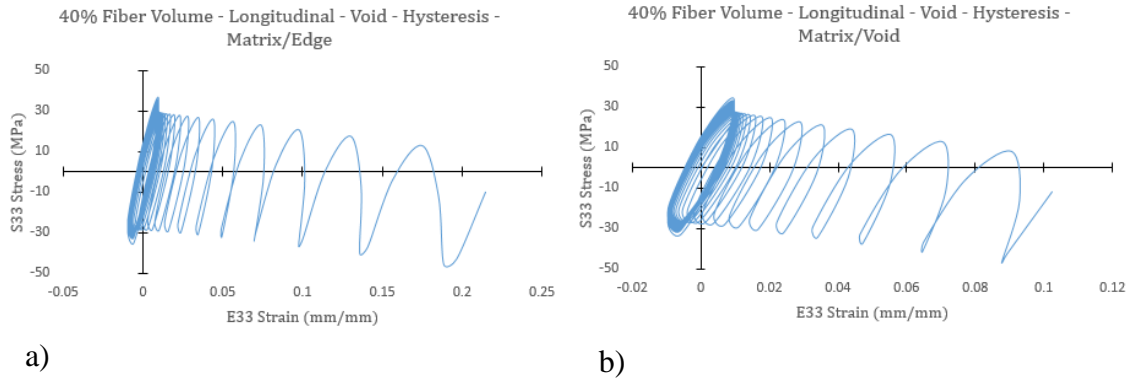


Figure 48 40% Fiber Volume - Longitudinal - Hysteresis a) Matrix/Void b) Matrix/Edge

The hysteresis loops for both matrix/void and matrix/edge are highly nonlinear. The normal E33 strain is at 2% initially but increases rapidly to 10% and 20% at the 15 minute mark. The maximum and minimum normal stress S33 for the matrix/void are 34.59 MPa and -46.55 MPa. Similarly, the maximum and minimum normal stress S33 for the matrix/edge are 36.98 MPa and -45.77 MPa. The matrix/fiber hysteresis loop is shown Figure 49. Maximum normal stress is 20.12 MPa and minimum normal stress is -21.65 MPa. The normal strain E33 strain varies between 0.95% and - 0.96% strain.

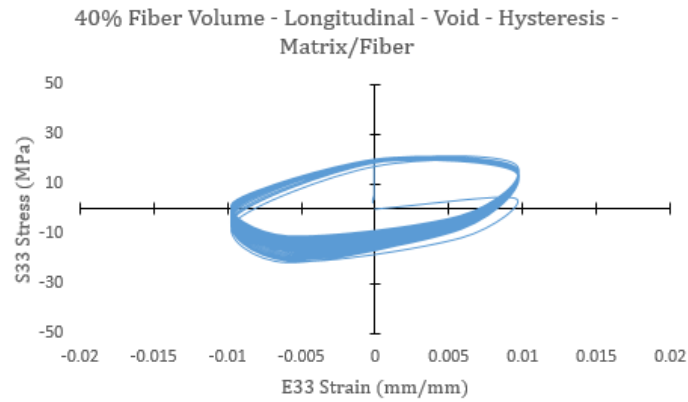


Figure 49 40% Fiber Volume - Longitudinal - Hysteresis – Matrix/Fiber

The normal strains in the unrestrained matrix/void and matrix/edge polymer are a magnitude greater than the strain in the matrix/fiber polymer. This indicates that the void and edge effect has a significant effect on the matrix deformation. Existence of voids decreases the overall stiffness in the matrix. Even when small void contents are considered, such as the ones presented in this study, the effect of voids on the overall mechanical responses of composites is significant. Cycling the composites with 50% and 60% fiber volume contents at frequency 2/60 Hz and a displacement amplitude of 0.01 mm shows the significant changes in the strain fields due to the existence of voids. Figure 50 is the principal strain contour of the composite having 50% fiber volume content with void configuration, at 20 minutes. Visible are the voids and the resulting strain perturbation.

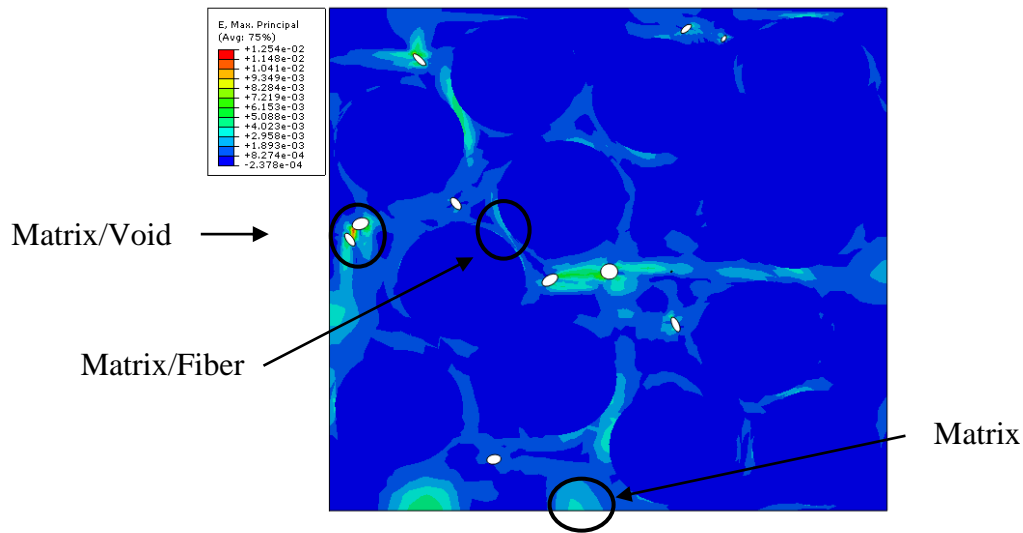


Figure 50 50% Fiber Volume – Void – Longitudinal -2/60 Hz- 20 minutes - Max Principal Strain

An additional close-up view of the perturbed principal strain field is also found Figure A-42. The strain in the matrix/fiber location (see Figure 50 for location), increases steadily until it reaches 2.89 % at 20 minutes. Allowing the 50% fiber volume model to recover, the strain recovers to 0.5%. The matrix/fiber principal strain plot for the 50% fiber volume content can be found in the appendix, Figure A-43. Figure 51 are the principal strain graphs for the matrix/void and matrix location.

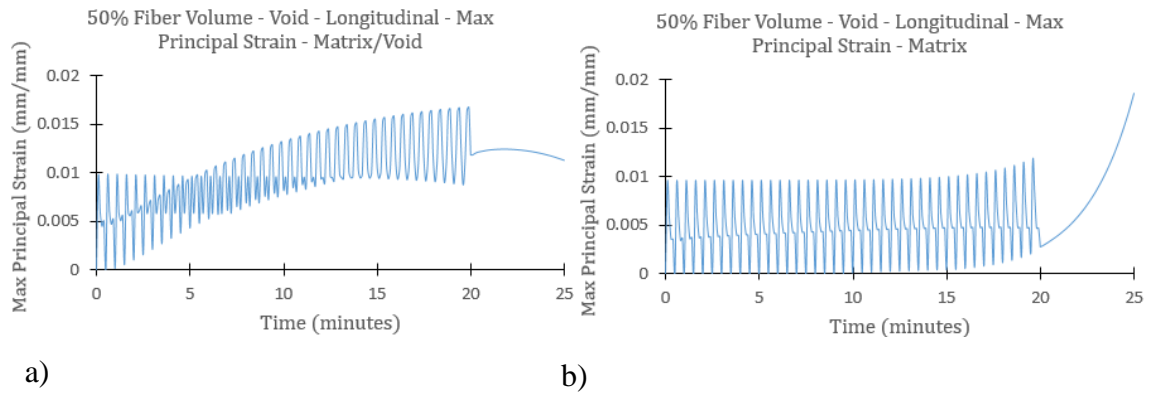


Figure 51 50% Fiber Volume - Void- Longitudinal- Principal Strain a) Matrix/Void b) Matrix

Figure 51, the principal strain adjacent to the void initially resides at 1% but increases until it reaches 1.58% at 20 minutes. Furthermore, during the recovery period, the principal strain recovers to approximately 1%. In comparison, the principal strain of the matrix remains at 1% and begins to increase during the recovery period because residual stresses causes the polymer matrix to creep. The matrix's principal strain at 25 minutes is 1.86%. The corresponding hysteresis loops for the composite with 50% fiber volume content did not show large strain deformation behavior. The hysteresis loops can be found in the appendix, Figure A-44 through Figure A-46.

Similar to the pristine longitudinal loading models, shown in section 4, the strains are larger in the matrix/fiber region for the composite with 60% fiber volume content. In addition, voids cause strain risers in the polymer. Figure 52 is the 60% fiber volume void model at 18.9 minutes. The locations of interests are also indicated in Figure 52. An additional close-up view of the 60% fiber volume and its void regions is given in the appendix.

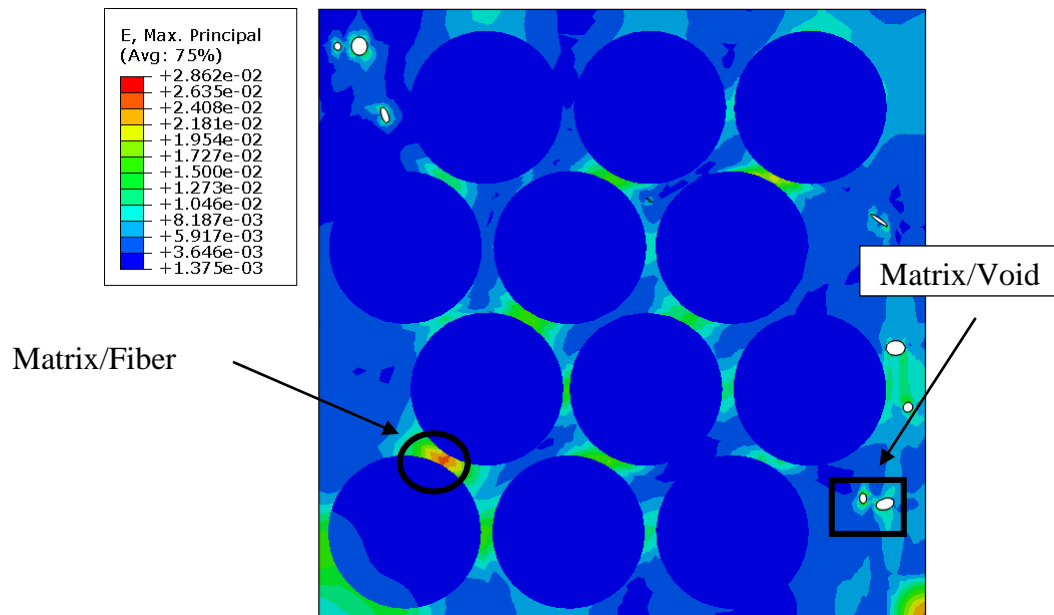


Figure 52 60% Fiber Volume - Void – Longitudinal Loading - Principal Strain - 18.9 minutes

The principal strain in the matrix/fiber region is initially at 1.17% and rises to 1.49% over the 20 minute loading period. The strain recovers to 0.336% during the 5 minute recovery period. In comparison, the matrix/void's principal strain is at 0.965% and increases to at 1.27% 20 minutes. Furthermore, the principal strain continues to increase to 4.10% during the recovery period, indicating that the polymer creeps. The principal strain graphs are shown in Figure 53. To show that the material creeps, the longitudinal stress graphs for both the matrix/fiber and matrix/void region are found in the appendix, Figure A-48. Furthermore the localized hysteresis loops prove that near the matrix/void region the polymer undergoes greater percentage change in strain than the polymer in the matrix/fiber region. Figure 54 are the hysteresis plots for both the matrix/fiber and matrix/void regions. The max S33 stresses in the matrix/fiber polymer and matrix/void are 28.74 MPa and 38.89 MPa, respectively. Minimum stresses are -28.11 MPa and -37.45 MPa for the matrix/fiber and matrix/void regions, respectively. This is comparable to the stress amplitudes experienced by the previously analyzed composites with 40% and 50% fiber volume contents. Furthermore, the principal strains generally began to increase at the 15 minute mark and continued to increase. Both composites having 50% and 60% fiber volume contents showed creep behavior near the voids. The composite having 40% fiber volume content showed the largest strain change in its matrix/void and matrix/edge regions.

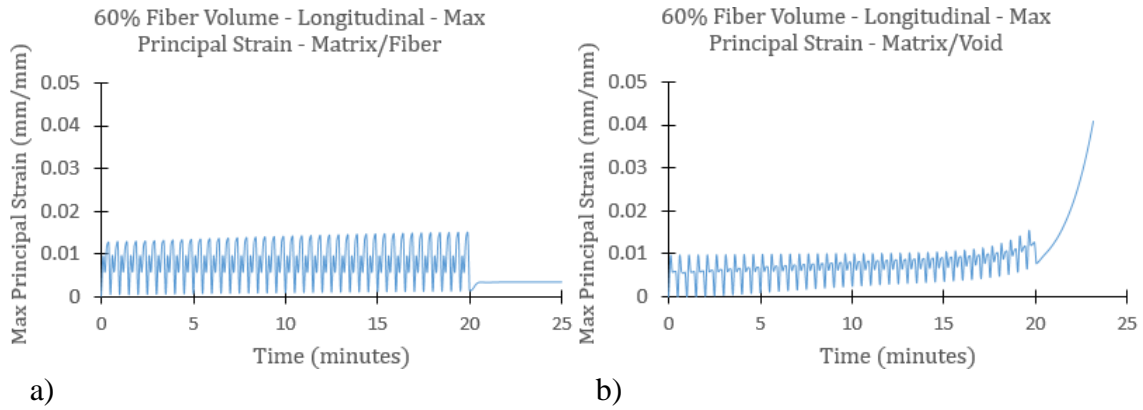


Figure 53 60% Fiber Volume - Void - Longitudinal - Max Principal Strain a) Matrix/Fiber b) Matrix/Void

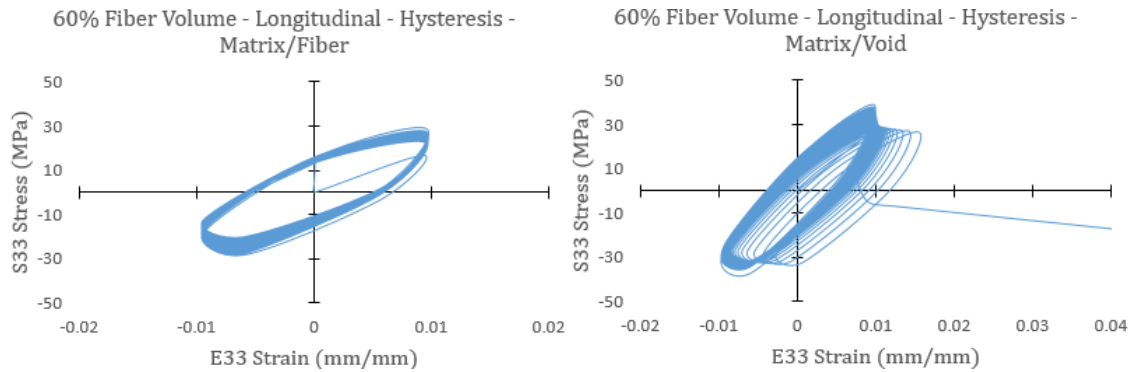


Figure 54 60% Fiber Volume - Void - Longitudinal - Hysteresis a) Matrix/Fiber b) Matrix/Void

Regarding the temperature changes, all three configurations increased by approximately 18 Kelvin through the 20 minute load duration. Furthermore, the temperature changes were uniform since the heat conduction throughout the composite body is allowed. Figure 55 is the temperature versus time for all three void fiber models. The principal strain plots for the matrix/void region for all fiber content models were nonlinear and showed large strain deformations when the temperature is increased. The principal strains versus their respective temperatures are plotted in Figure 56. The six separate graphs in the figure show the matrix/fiber and matrix/void strains for each composite model. In general, the strains are at approximately 1% initially for the matrix/void locations which agree well with the applied displacement of 0.01 mm.

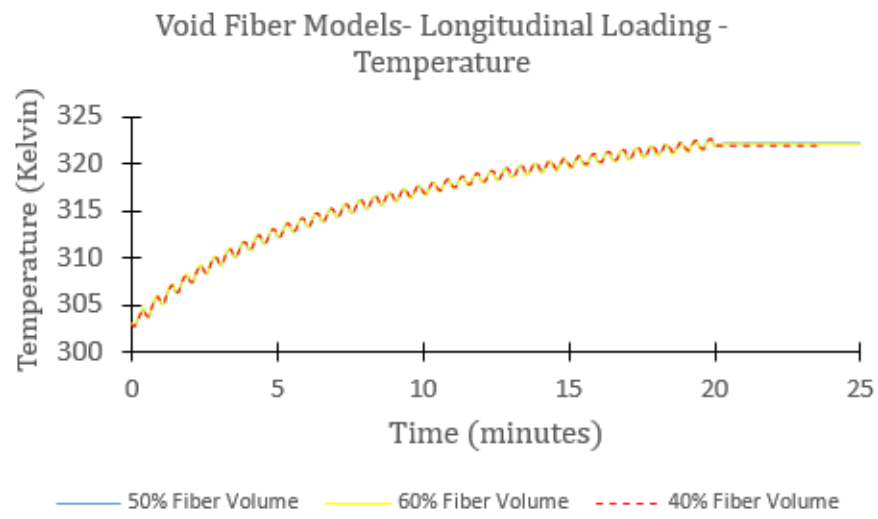
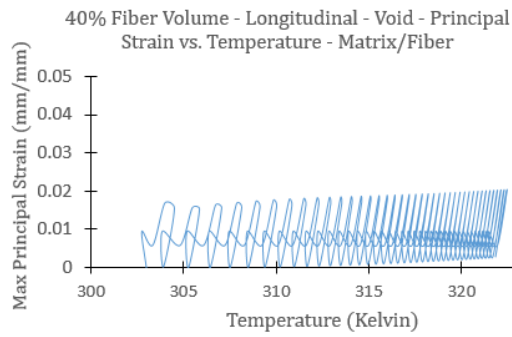
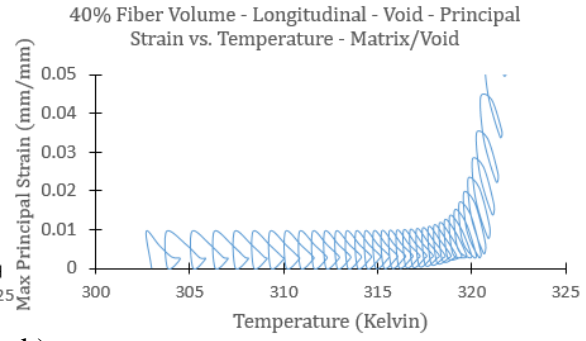


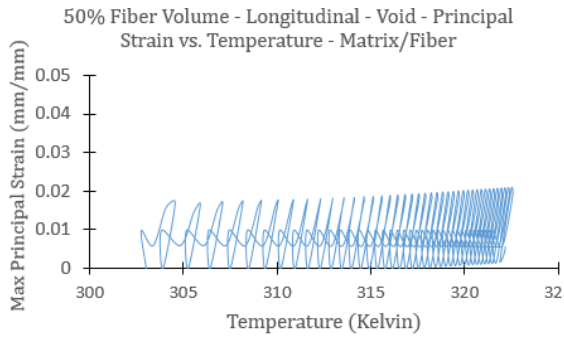
Figure 55 Void Models - Longitudinal – Temperature



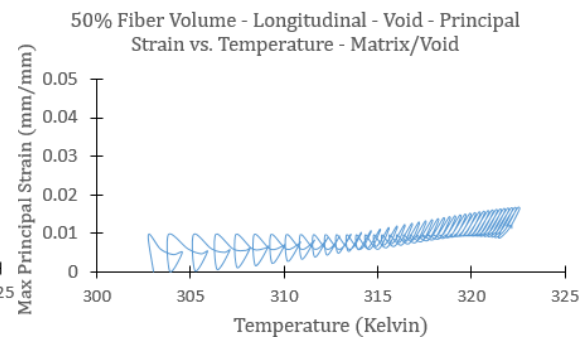
a)



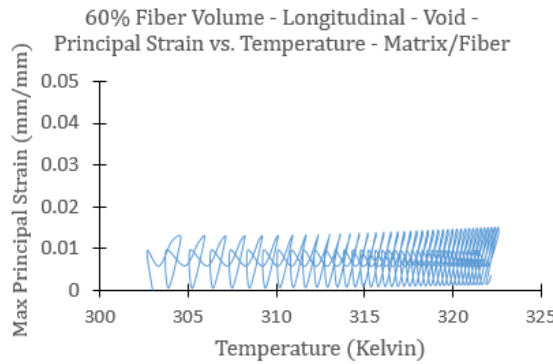
b)



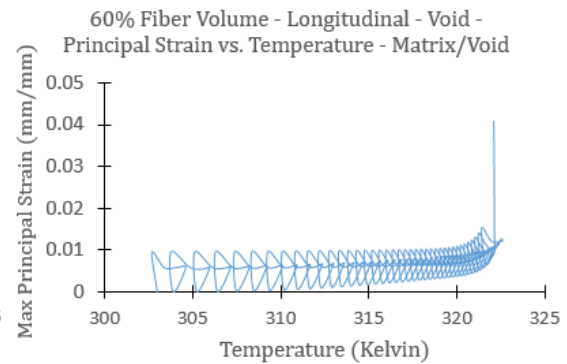
c)



d)



e)



f)

Figure 56 Max Principal Strain vs. Temperature – Longitudinal Loading – Void - a) 40% Fiber Volume Matrix/Fiber b) 40% Fiber Volume Matrix/Void c) 50% Fiber Volume Matrix/Fiber d) 50% Fiber Volume Matrix/Void e) 60% Fiber Volume Matrix/Fiber f) 60% Fiber Volume Matrix/Void

Table 11 summarizes the principal strains at three temperatures: 310 Kelvin, 315 Kelvin and 320 Kelvin. The maximum principal strains in the matrix/fiber reached 1.45 % - 2.01%. The strains in the matrix/void region are lower initially but do increase throughout the load cycle. However, at the same temperature, principal strains in the matrix/void are still lower than in the matrix/fiber strains.

Table 11 Max Principal Strain vs. Temperature - Void - Longitudinal Loading

Fiber Volume		40%	50%	60%	40%	50%	60%
Location		Matrix/Fiber			Matrix/Void		
Temperature (Kelvin)	310	1.79%	1.75%	1.27%	0.95%	0.77%	0.98%
	315	1.88%	1.86%	1.36%	0.96%	1.18%	0.99%
	320	1.98%	2.01%	1.45%	1.39%	1.53%	1.05%

7.2 Shear Loading of Void Fiber Configuration Samples

Three fiber volume configurations are cycled at frequency 2/60 Hz for twenty minutes followed by a 5 minute recovery period. Figure A-49 in the appendix illustrates the shear load profile. The shear displacement applied on the front face is 0.01 mm in the 1-direction. In general, temperature changes and permanent strain deformations occur less than in the longitudinal void models. However, large polymer matrix deformation was observed in matrix adjacent to fibers which are spaced far apart. As an example, Figure 57 shows the principle strains for the composite with 50% fiber volume content at 14 minutes and 30 seconds. At the center of the fiber sample and at the sample's edges, larger deformation occurs. Subsequently, these regions have larger strains than the overall homogeneous strain. The figure shows that the 50% fiber volume, void configuration, has 12 fibers totals and 10 voids. The matrix/void and matrix/fiber locations are marked in the figure.

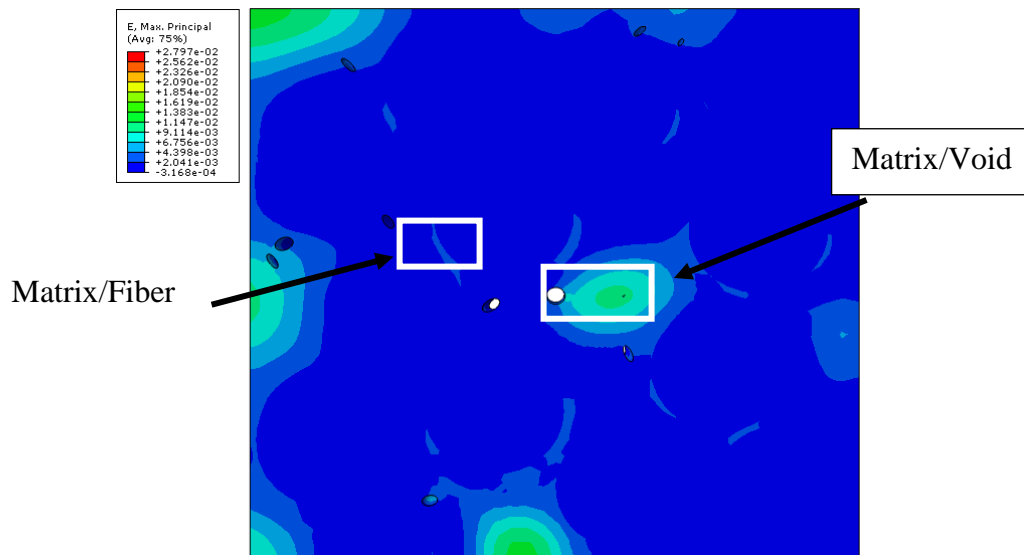


Figure 57 50% Fiber Volume - Void - Shear Loading - Max Principal Strain - 14.50 Minutes

The principal strain in the matrix/void region is at 0.5% for the first 15 minutes of the cyclic loading period and rises to 3.56% at 20 minutes. The strain rate for the matrix/void polymer increases throughout cycling. During the 5 minute recovery period,

the principal strain continues to rise and reaches 12.3% which would constitute strain failure in the polymer. Residual stresses in the matrix/void region cause the material to creep. The maximum principal stress plot for the matrix/void location is found in the appendix, Figure A-50. In contrast, the matrix/fiber principal strain is higher initially (1.24%) but the change in principal strain is smaller and reaches only 1.40% at 20 minutes. In addition, the matrix/fiber polymer recovers to 0.39% after 5 minutes of recovery. The principal strain is plotted in Figure 58 a) for the matrix/void and Figure 58 b) for the matrix/fiber.

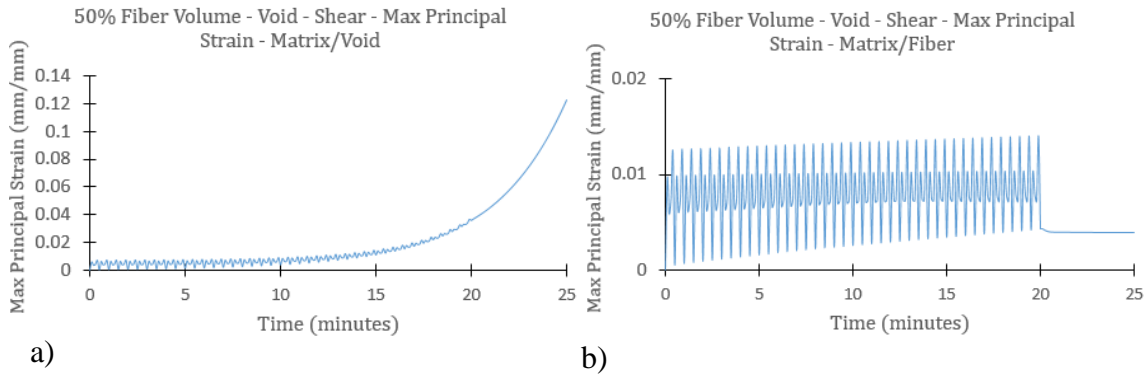


Figure 58 50% Fiber Volume - Void - Shear - Max Principal Strain – a) Matrix/Void b) Matrix/Fiber

While the principal strains indicate the existence of viscous strain after removal of loading, the corresponding hysteresis loops in the matrix regions show less energy dissipation than the hysteresis loops in the longitudinal loading samples. Shear stresses are less than 15 MPa and shear strains are less or equal to 1% shear strain. In fact, the shear stress/strain hysteresis plots for both locations behave linearly. For reference purposes, the shear hysteresis plots for the 50% fiber volume, void configuration are found in the appendix, Figure A-51 and Figure A-52. Surprisingly, the E33 normal strain constitutes a significant portion of the overall strain. However, plotting the E33 and S33 hysteresis plots, it is evident that these strains are significant. Figure 59 a) is the hysteresis plot in the matrix/fiber region and Figure 59 b) is the hysteresis plot in the matrix/void region. The E33 normal strains for the matrix/fiber region are very small and vary between

-0.2% and 0.2%. The normal stress S33 varies between 11.00 MPa and -9.70 MPa. In comparison, the E33 normal strain increases to 3% at the end of 20 minutes but continues to creep because of residual stresses until it reaches 12.2%. The S33 stresses vary between 4.81 MPa and -62.54 MPa.

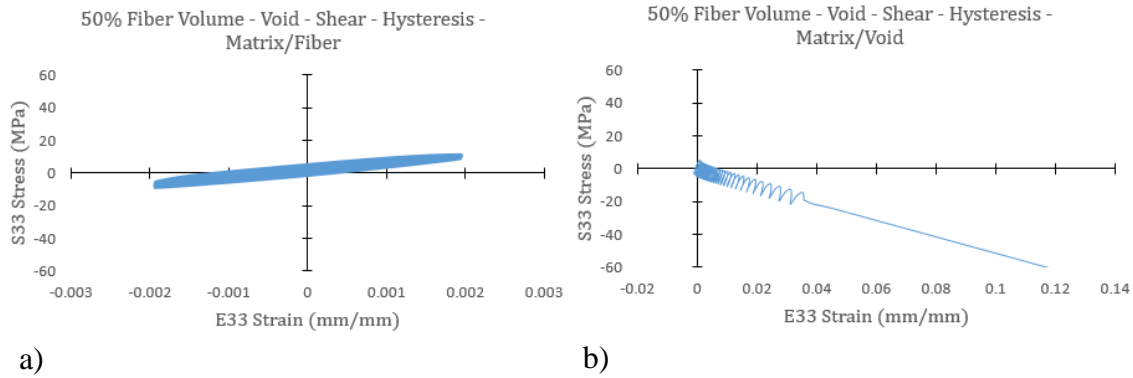


Figure 59 50% Fiber Volume - Void - Shear - Hysteresis – a) Matrix/Fiber b) Matrix/Void

The 40% fiber volume void model is evaluated at three different locations. The locations are labeled as matrix/fiber, matrix/void and matrix. Overall, the matrix/fiber and matrix/void exhibited linear-elastic behavior and permanent deformation is negligible. In contrast, matrix near the edge region strains and deforms until convergence issue due to excessive deformation occurred. Figure A-53 in the appendix shows the contour plot for the principal strain at 20 minutes. The locations of the three regions of interest can be found in Figure A-54. Also, the principal strains are plotted for 40% fiber volume in Figure 60. The principal strains at 20 minutes for the matrix/fiber and matrix/void at 20 minutes are 1.56% and 1.0%. The principal strain for the matrix/fiber in the composite with 40% fiber content is similar to the principal strain for the matrix/fiber in the composite with 50% fiber content. However, the principal strain in the matrix/void for the 40% fiber volume stays constant throughout the loading period. This differs from the matrix/void region in the composite with 50% fiber volume content which deforms heavily. Nevertheless, the 40% fiber volume shows deformations in the polymer matrix near the

edge region of the geometry. Figure 60 c) is the principal strain for the matrix. From the graph, the polymer deforms rapidly and reaches 11.2 % strain at 25 minutes.

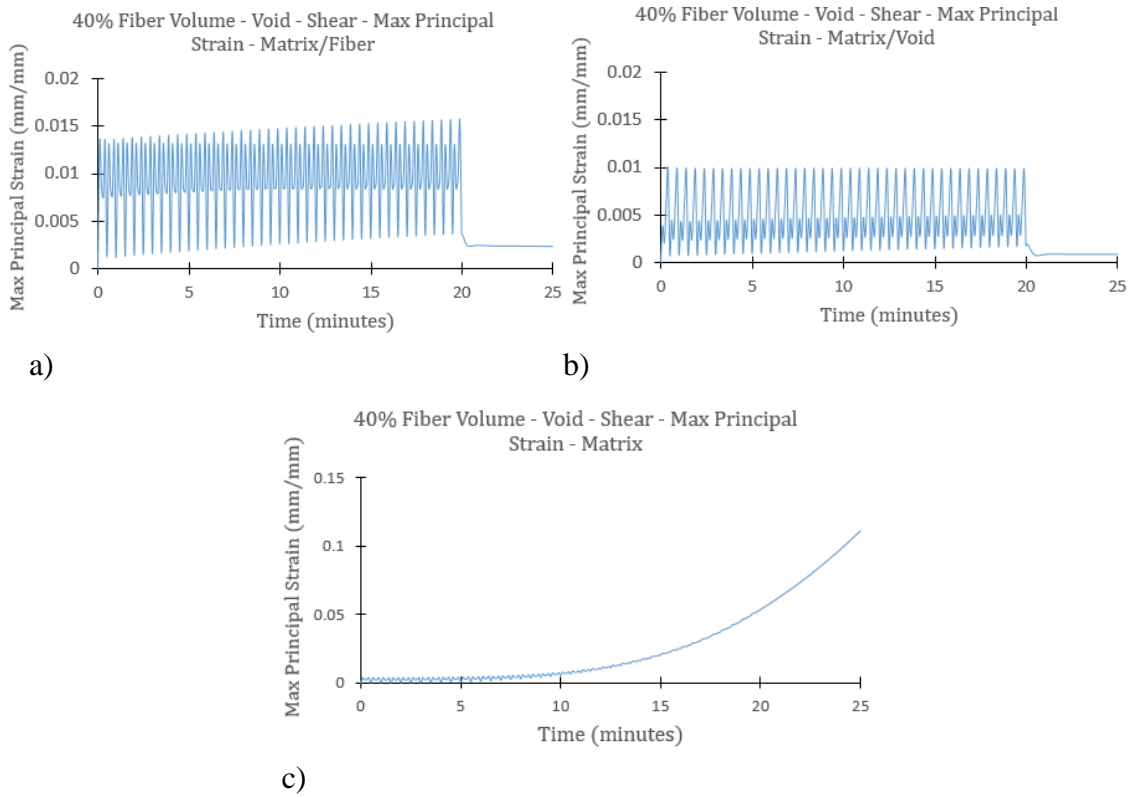


Figure 60 40% Fiber Volume - Void - Shear - Principal Strain a) Matrix/Fiber b) Matrix/Void c) Matrix

Evaluating the shear hysteresis and the affiliated energy dissipation, both matrix/fiber and matrix/void regions exhibit linear hysteresis behavior. Plotting the E13 shear strain and S13 shear stress for matrix/fiber, matrix/void and matrix region, the strains are less than 2% and the stresses are less than 20 MPa. Figure 61 is the shear hysteresis plot for the 40% fiber volume. On the other side, Figure 62 are the normal strains (E33) hysteresis plots for all three locations. In contrast to Figure 61, the normal strains are smaller in magnitude but the hysteresis traces are nonlinear. The hysteresis plot of the matrix region, as shown in Figure 61 c), is especially noteworthy: The hysteresis trace does not form a closed loop, instead the strain continues to increase throughout the loading period. This behavior is similar to the hysteresis plot of composite with 50% fiber volume

content (see Figure 59 b) where the E33 normal strain and S33 normal stress exhibit larger nonlinear behavior.

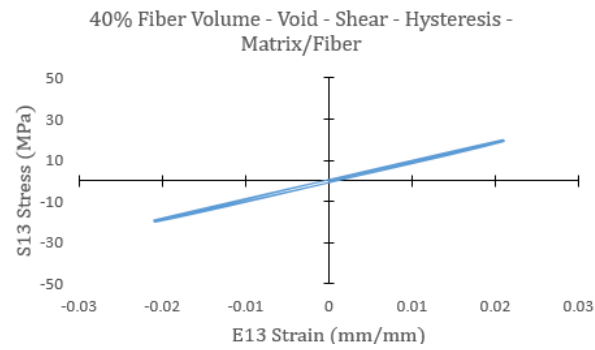


Figure 61 40% Fiber Volume - Void - Shear - Shear Hysteresis - Matrix/Fiber

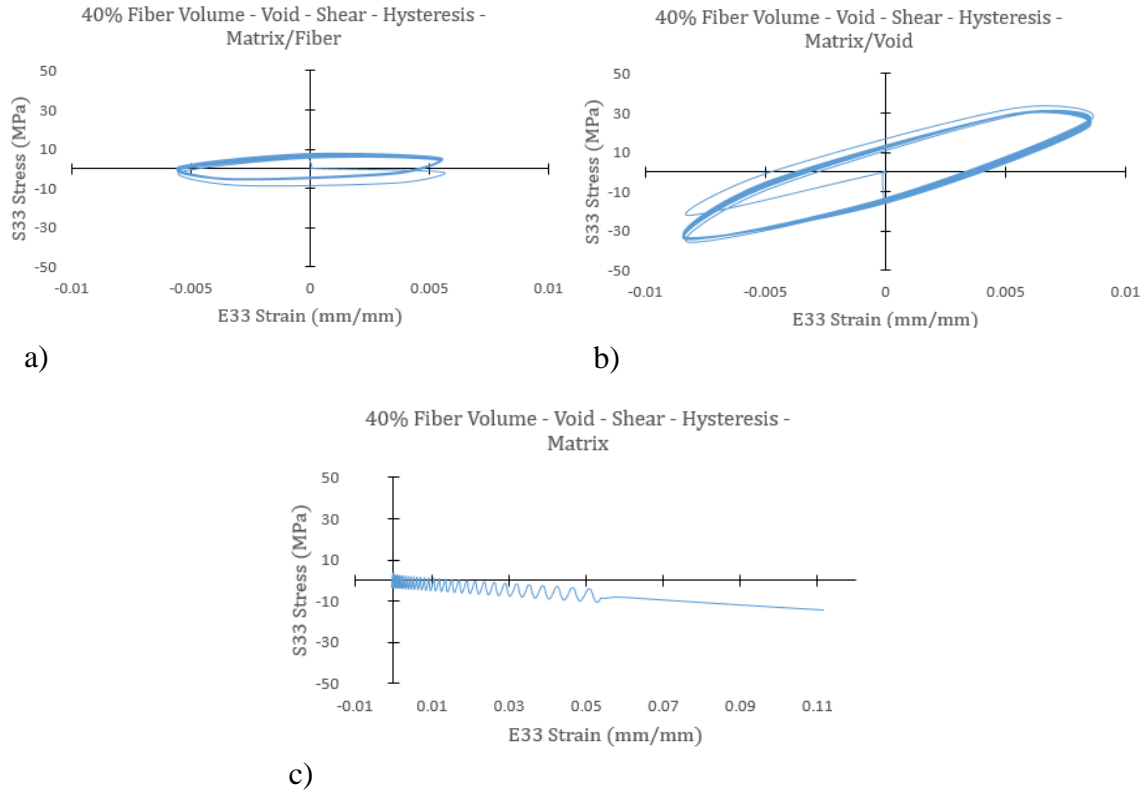


Figure 62 40% Fiber Volume - Void - Shear - Hysteresis - a) Matrix/Fiber b) Matrix/Void c) Matrix

At last, the effect of void on the overall responses of the composite with 60% fiber volume content is also evaluated for the deformation near the voids and fibers. To distinguish the respective regions, Figure 63 is the principal stress contour plot for the 60% fiber volume, void configurations. Three regions are labeled in the figure: Matrix/Fiber, Matrix/Void and Matrix.

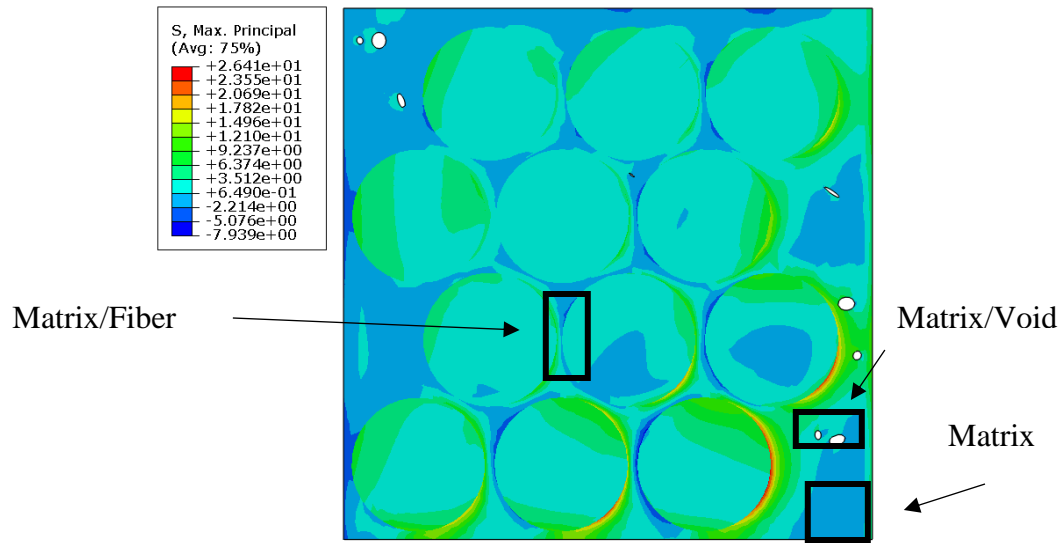


Figure 63 60% Fiber Volume - Void - Shear Loading - Max Principal Stress - 3 minutes

The principal strains for the matrix/void and matrix regions increase during the 20 minute load cycle. The principal strain increase is significant for the matrix region, which reaches 1.47% at 10 minutes, 5.50% at 15 minutes and 24% at 20 minutes. For the matrix/void region, the principal strain starts at 0.74% initially and increases to 0.95% at 20 minutes. However, the matrix/void region continues to creep during the 5 minute recovery period and reaches 3.25 %. In contrast, the matrix/fiber does not experience large deformations. The matrix/fiber region has 1.46% principal strain but the principal strain does not increase through the loading period. Figure 64 shows the principal strain plots for the matrix/void, matrix/fiber and matrix regions. Overall, for the void samples subjected to shear loading, the initial strains at the matrix/fiber interface are always higher but the matrix/fiber polymer is resistant to permanent deformation.

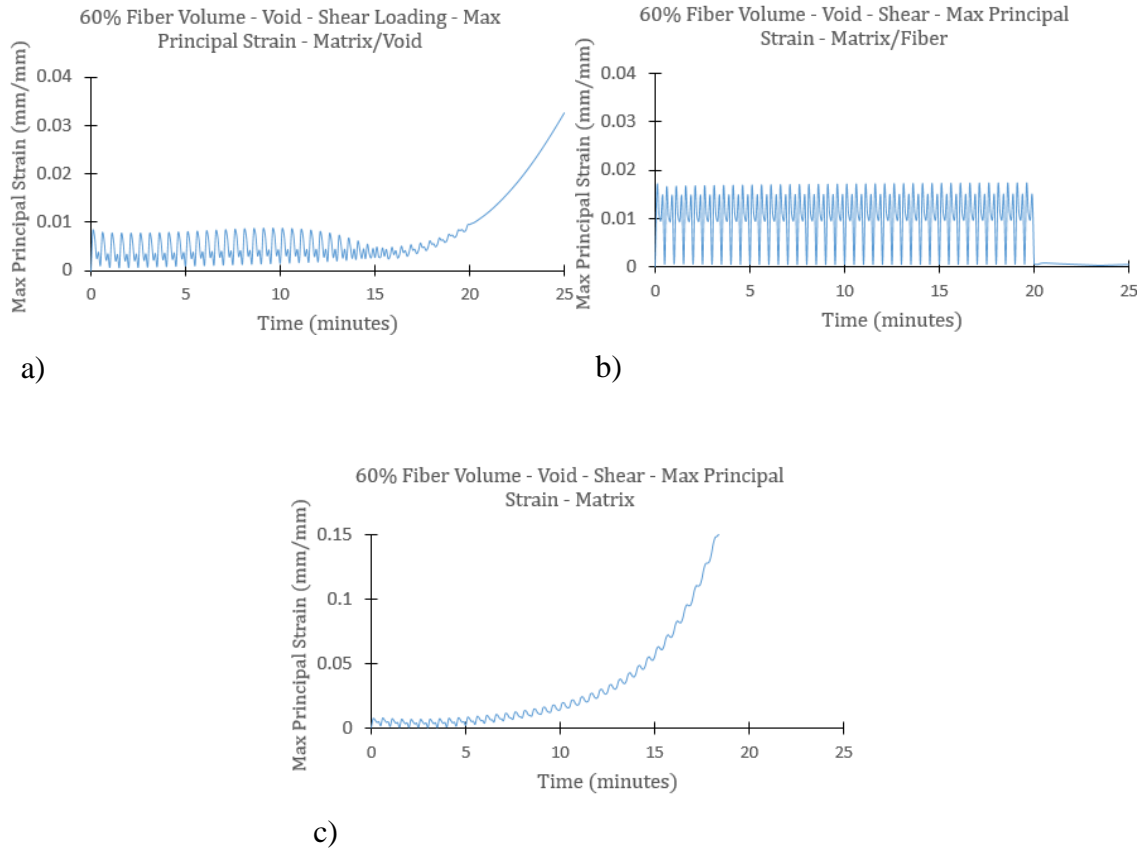


Figure 64 60% Fiber Volume - Void - Shear Loading - Principal Strain a) Matrix/Void b) Matrix/Fiber c) Matrix

Evaluating the individual strain components of the three locations, the E33 normal strains and S33 normal stresses constitute a major component of the principal strain. The hysteresis plots are shown in Figure 65. The matrix/void hysteresis is shown in Figure 65 a) and shows that the polymer is under compressive normal strains towards the end of the load cycle. Figure 65 b) is the hysteresis graph for the matrix/fiber region. First, the normal strains are less than the normal strain in either matrix/void or matrix location. The normal strain in the matrix/fiber location oscillates between -0.34% and 0.35% and the hysteresis loop traces a nearly linear elastic hysteresis loop. In contrast, Figure 65 c) is the matrix hysteresis. The hysteresis plot is highly nonlinear and does not recover its strain amplitude. The strain keeps increasing while the normal stress continues to decrease throughout the load cycle. Comparing the hysteresis loops across different fiber volume models, the

matrix is susceptible to shear loading and is subjected to the largest deformations. Furthermore the matrix/fiber locations experience higher strains and stresses initially but behave linear elastic throughout the load cycle. Additional hysteresis plots for the 60% fiber volume composite can be found in the appendix, Figure A-55 through Figure A-57.

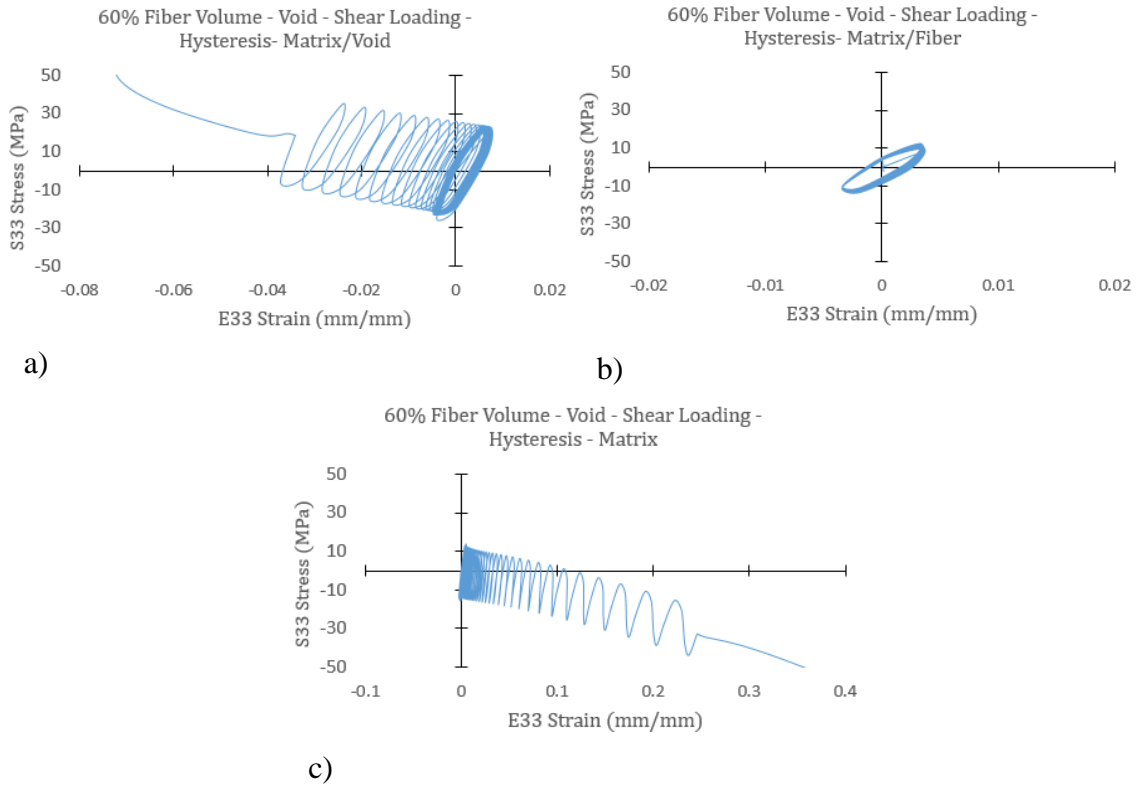


Figure 65 60% Fiber Volume - Void - Shear Loading a) Matrix/Void b) Matrix/Fiber c) Matrix

For temperature increases, all configurations increased in temperature. At 20 minutes, the 40% fiber volume is at 309.5 Kelvin, the 50% fiber volume is at 311.0 Kelvin and the 60% fiber volume is at 312.5 Kelvin. Figure 66 is the temperature plot versus time for the shear loaded void models.

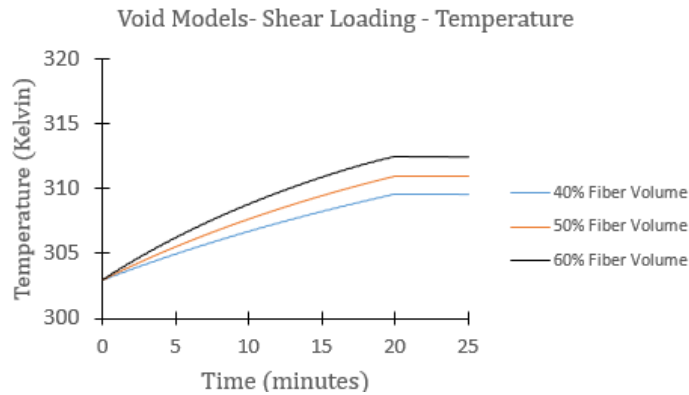
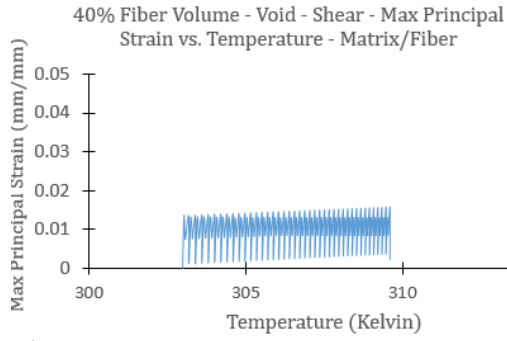
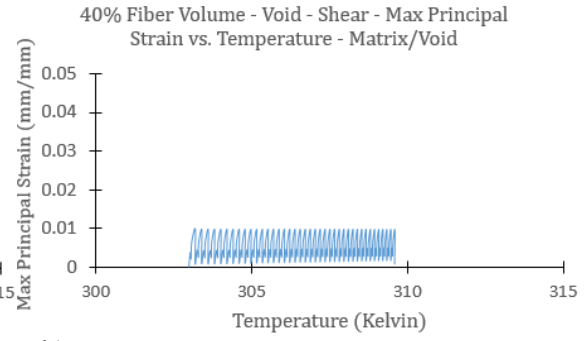


Figure 66 Void Models - Shear Loading – Temperature

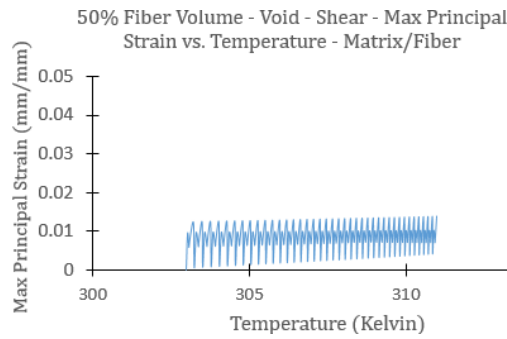
The temperature ranges for the shear loading are clearly delineated. In Figure 67, the principal strains for all three fiber models at the matrix/fiber and matrix/void locations are plotted. The temperature ranges from 303 Kelvin to 312 Kelvin and is generally small. The principal strains for both the composites with 40% and 60% fiber contents oscillated between 0 and 1% which is in good agreement with the overall homogenized strain response. However, in the 50% fiber content model the principal strain in the matrix/void region increased to 1.38% at 310 Kelvin and continues to creep during the recovery period. Furthermore, in the 60% fiber volume, the principal strain in the matrix/void (Figure 67 f) decreases slightly at 310 Kelvin and then increases back to 1% at 312 Kelvin. This is unusual because the rest of the principal strain graphs only show strain increases throughout the load cycle. In general, the matrix/void region in a void sample are not as susceptible to temperature changes as the pure matrix region for the pristine fiber samples (Figure 35). Strains are less than 5% and the increase in strain is small. Table 12 summarizes the principal strains for the fiber models at 305 Kelvin, 307 Kelvin and 310 Kelvin. Note that there is no value for the 40% fiber volume at 310 Kelvin. The 40% fiber volume's temperature only increased to 309.5 Kelvin.



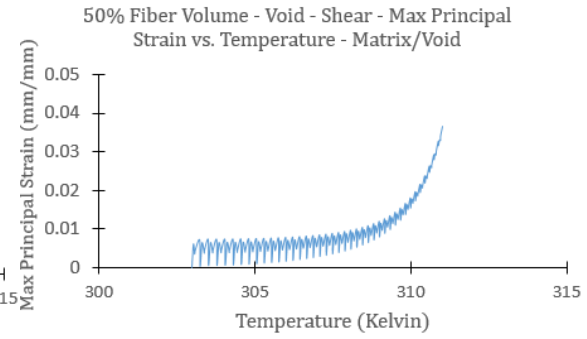
a)



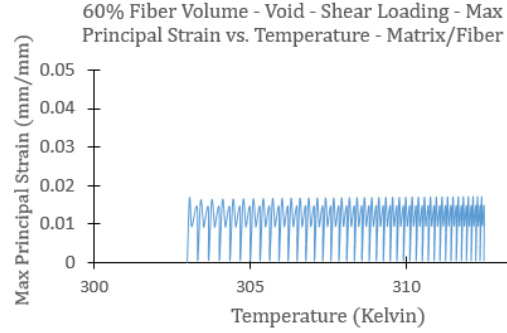
b)



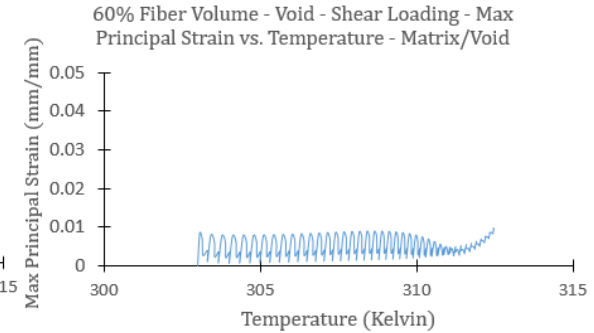
c)



d)



e)



f)

Figure 67 Max Principal Strain vs. Temperature – Shear Loading – Void - a) 40% Fiber Volume Matrix/Fiber b) 40% Fiber Volume Matrix/Void c) 50% Fiber Volume Matrix/Fiber d) 50% Fiber Volume Matrix-Void e) 60% Fiber Volume Matrix/Fiber f) 60% Fiber Volume Matrix/Void

Table 12 Max Principal Strain vs. Temperature - Void - Shear Loading

Fiber Volume		40%	50%	60%	40%	50%	60%
Location		Matrix/Fiber			Matrix/Void		
Temperature (Kelvin)	305	1.30%	1.27%	1.46%	0.97%	0.75%	0.77%
	307	1.47%	1.31%	1.66%	0.98%	0.78%	0.86%
	310	N/A	1.38%	1.69%	N/A	1.98%	0.47%

7.3 Transverse Loading of Void Fiber Models

The transverse fiber models have four carbon fibers instead of the 12 fibers found in the longitudinal and shear loaded models. Ellipsoidal voids are added to the individual finite element models to study the effect of voids on the field variables on the microscopic level. For the 40% fiber content model, the void content is 0.20%. The 50% and 60% fiber content models had void percentages of 0.16% and 0.10%, respectively. Adding voids to the transverse models dramatically increases the computational time. For the 40% fiber model, a traction of 60 MPA is applied on the bottom face of the model. The 40% fiber model is cycled along the y-direction with a frequency 3/60 Hz. Figure 68 shows the material orientation of the system and the location of the voids in the polymer matrix of the 40% fiber volume specimen.

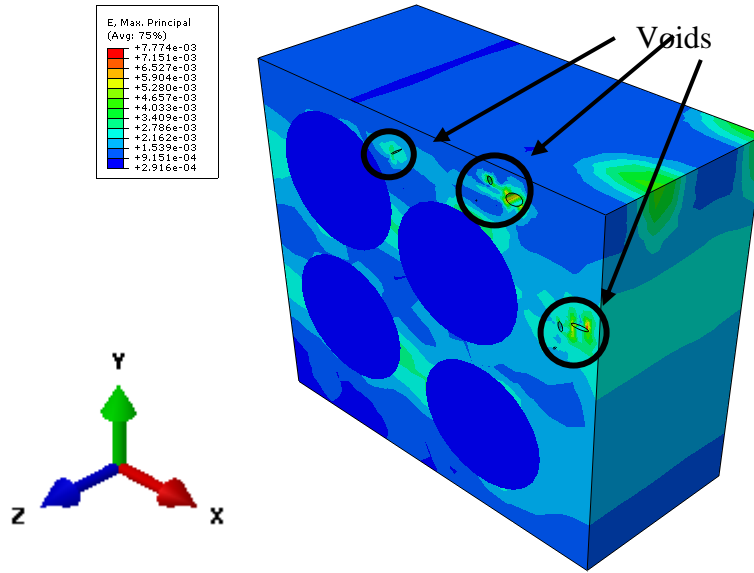


Figure 68 40% Fiber Volume - Void – Transverse

Two locations in the 40% fiber volume specimen are studied, one adjacent to neighboring fibers and one adjacent to the void. Figure 69 shows the locations of the fiber/matrix and matrix/void regions. Figure 70 show the maximum principal strain history

for both the matrix/fiber and matrix void element. The maximum principal strain for a matrix/fiber element oscillates between 0% and 4.1% strain and does not significantly increase throughout the load cycles. However, the maximum principal strain adjacent to a void is lower in magnitude initially (~0.8%) but steadily increases throughout the 30 minutes of loading until it reaches a maximum principal strain of 1.34%.

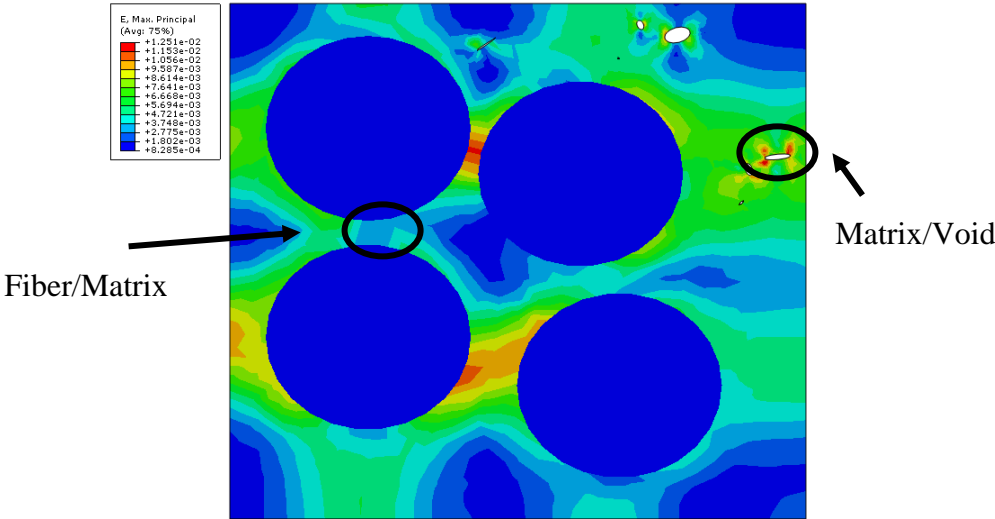


Figure 69 40% Fiber Volume - Void - Transverse - Max Principal Strain - 29.3 minutes

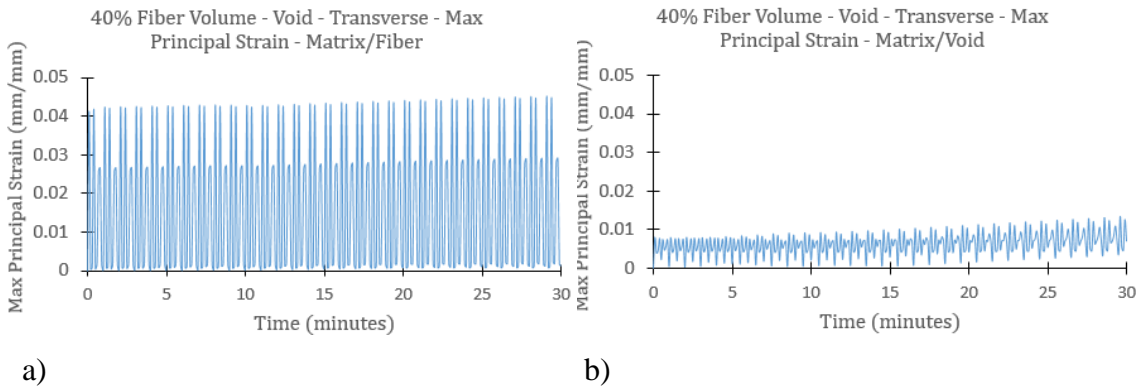


Figure 70 40% Fiber Volume - Void - Transverse - Max Principal Strain a) Matrix/Fiber b) Matrix/Void

Multiple strain components including the shear strain and normal strain contribute to the maximum principal strain. The shear hysteresis graphs are shown in Figure 71. It is apparent that the matrix/void location experiences significant shear strain deformation. The maximum shear strain E12 reaches a maximum of 2.03% and a minimum of -1.26%. The shear stress S12 amplitudes for the matrix/void region oscillates between 11 and -11 MPa. In contrast, Figure 71 a) which is the shear hysteresis for the matrix/fiber region shows that the shear strain only reaches 0.37% and -0.26%. Furthermore, the shear stress amplitudes are small, oscillating between 3.08 and -3.11 MPa.

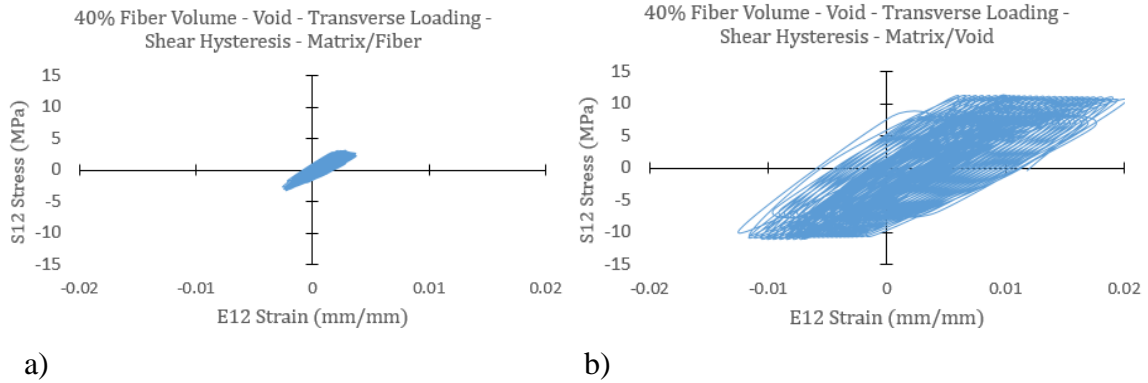


Figure 71 40% Fiber Volume - Void - Transverse – Shear Hysteresis a) Matrix/Fiber b) Matrix/Void

However, the normal strain E22 and normal stress S22 for the matrix/fiber region is significant. In comparison, the normal stress and strain components for the matrix/void regions are small in comparison to the stress and strain in the matrix/fiber region. The normal strain and stress hysteresis graphs are shown in Figure 72. The normal stress in the matrix/fiber region S22 vary from -144 MPa to + 149 MPa, while the E22 normal strain amplitudes vary from -4.21% to 4.51%. In comparison to the matrix/void's shear strains, the matrix/void's normal strains are small and vary between -0.60% and 0.69%. The normal stresses are insignificant as well, cycling between -8.25 and 8.07 MPa.

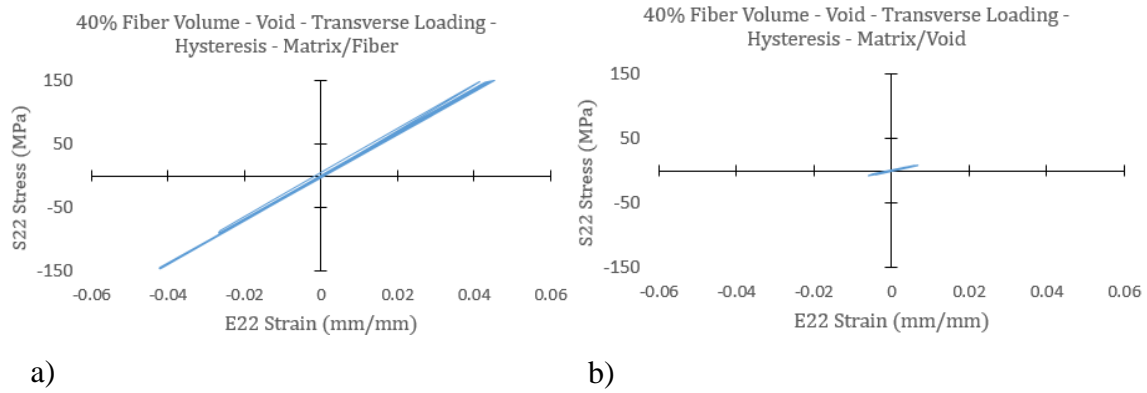
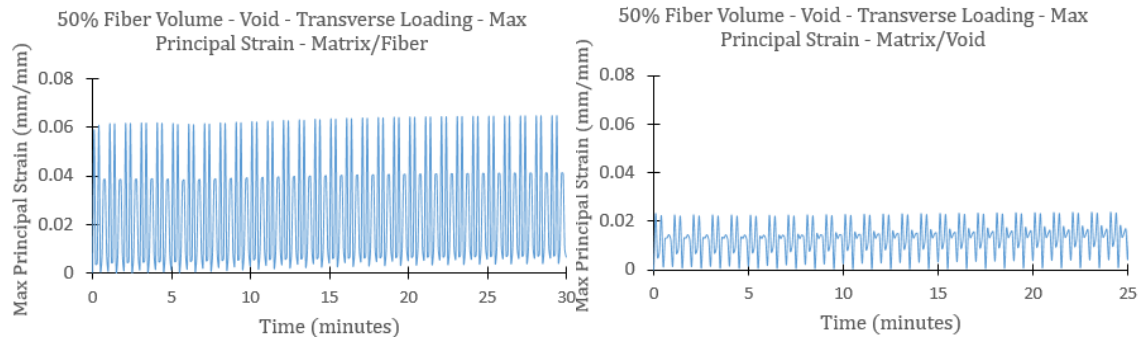


Figure 72 40% Fiber Volume - Void - Transverse – Hysteresis a) Matrix/Fiber b) Matrix/Void

The model with 50% fiber volume content is cyclic loaded along its transverse fiber direction for thirty minutes. The traction load is 80 MPa and the cyclic frequency is 3/60 Hz. The regions of interests, matrix/fiber and matrix/void are highlighted in the appendix, Figure A-58. The principal strains for the regions are plotted in Figure 73. Both matrix/fiber and matrix/void strains behave linearly and no increase in strain is observed. The matrix/fiber max principal strain is 6.48% and the matrix/void's max principal strain is 2.37%. Comparing the 50% fiber volume's response to the 40% fiber volume's response, they are similar: The matrix/fiber strains are within the 4-6% range while the matrix/void's principal strains remain low, between 1-2%. Noteworthy is that the 40% fiber volume's principal strain increases but the increase in principal strain is small and less than 0.55%. In contrast to the longitudinal and shear load cases, traction controlled displacement is applied to the transverse loaded fiber models. The maximum principal stress for the transverse loaded samples in the fiber/matrix is 150 MPa and 212.41 MPa for the 40% and 50% fiber content respectively. In contrast, the max principal stresses for the longitudinal load case (0.01 mm displacement) are 42.36 MPa and 37.36 MPa for 40% and 50% fiber content respectively. For the shear load case (0.01 mm shear displacement), the max principal stresses are 30.41 MPa and 30.25 MPa for the 40% and 50% fiber content models. Figure A-59 through Figure A-70 in the appendix show the principal stresses at both fiber/matrix and matrix/void locations for the 40% and 50% fiber content models.



a)

b)

Figure 73 50% Fiber Volume - Void - Transverse Loading - Max Principal Strain – a) Matrix/Fiber b) Matrix/Void

The principal strain components are mainly due to the normal strains E11 and E33. Figure 74 shows the hysteresis plot for the E22 normal strain and S22 normal stress. Figure 74 a), which is the hysteresis for the matrix/fiber, shows that the normal strain alternates in a nonlinear fashion. The matrix/fiber normal strains alternate between -0.70% and 0.97%. In contrast to the matrix/fiber, the strains in the matrix/void region behave essentially linear-elastic. The normal strain in the matrix/void region oscillates between -1.43% and 1.84%. The maximum normal stresses are 87.42 MPa and 15.69 MPa for the matrix/fiber and matrix/void respectively.

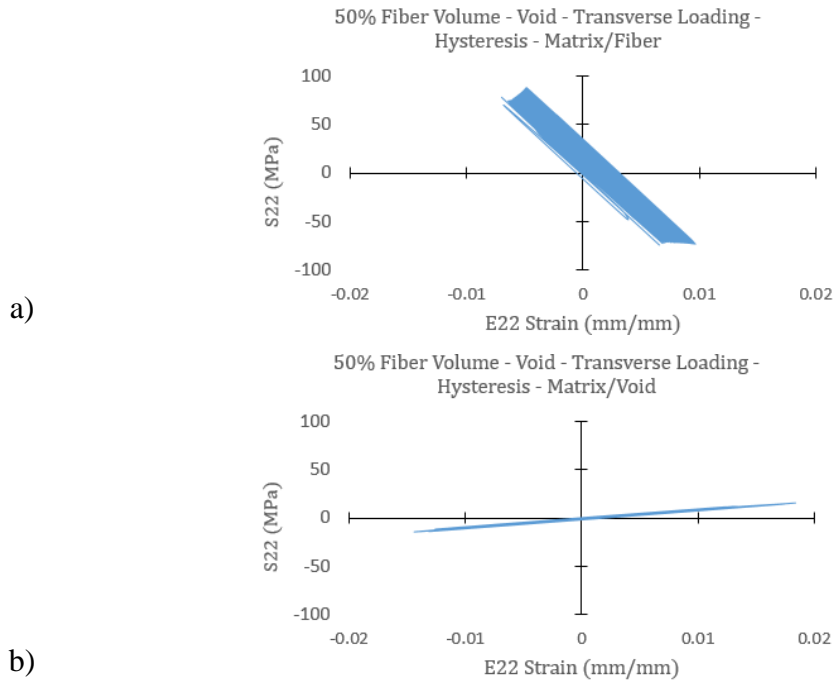
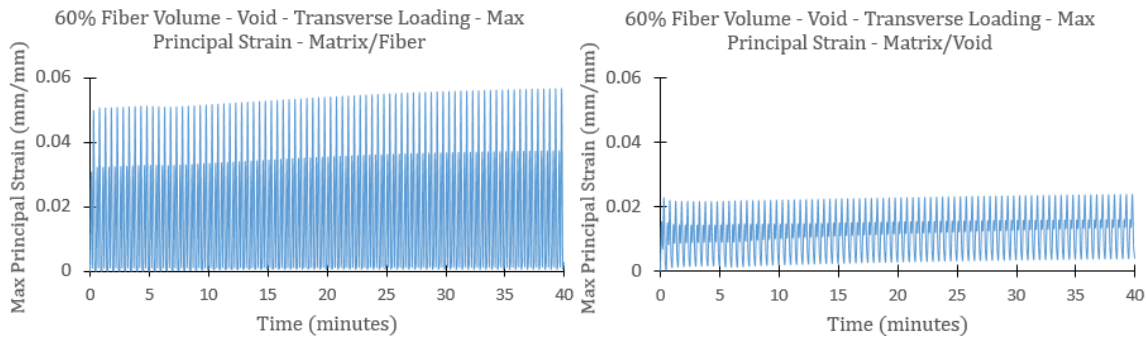


Figure 74 50% Fiber Volume - Void - Transverse Loading - y-direction Hysteresis a) Matrix/Fiber b) Matrix/Void

The composite is loaded along the x-direction or 1-direction. Therefore, it is expected that the normal strains E11 should be largest, as demonstrated in the hysteresis plots for the normal strains E11 and S11. For the matrix/fiber, the normal strains E11 varied from -6.23% to 6.48%. The normal strains in the matrix/void alternate from -2.57% to 2.37%. In addition to the greater normal strains, the normal stresses S11 are also greater than the S11 normal stresses (shown in Figure 74). The normal stresses S11 for the matrix/fiber vary from -203.14 MPa to 212.27 MPa. Normal stresses in the matrix/void region are smaller, oscillating from -60.04 MPa to 56.65 MPa. The E11/S11 hysteresis plots behave linear elastic and the graphs are located in the appendix, Figure A-71 and Figure A-72.

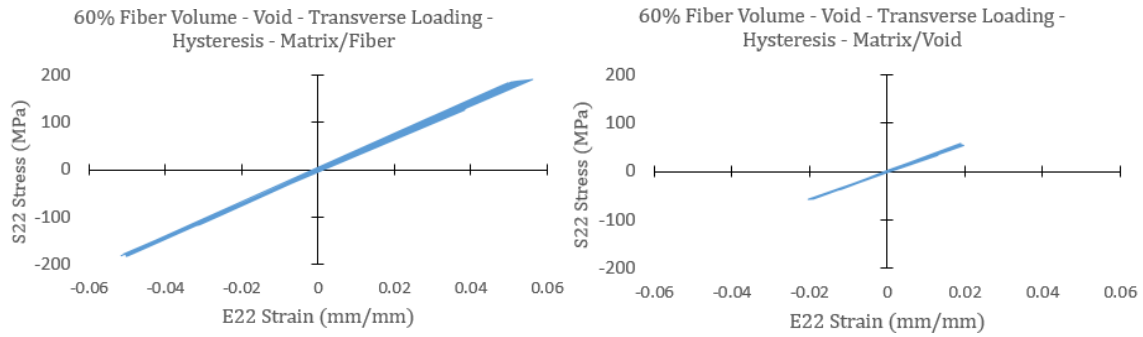
The composite models with 60% fiber volume content are spaced at least 10% of the fiber radius apart. A traction load is applied to the bottom face of the model and the cyclic frequency is 4/60 Hz. In comparison, the 40% and 50% fiber models are cycled at frequency 3/60 Hz. Furthermore, the cyclic load duration is increased from 30 minutes to

40 minutes to obtain a correlation between loading duration and temperature change. Similar to the principal strain results shown in the previous transverse loading, the matrix adjacent to closely-spaced fibers is at a higher strain state. The regions of interests and the geometry of the 60% fiber model can be found in the appendix, Figure A-73. The principal strains for the 60% fiber model at two locations are shown in Figure 75. The principal strain for the matrix/fiber is at 5.07% and rises to 5.67% at 40 minutes. The matrix/void's principal strain is lower and reaches a maximum of 2.36%. At both locations, the strains behave linear-elastic and no large deformation is observed in the 60% model.



a) b)
Figure 75 60% Fiber Volume - Void - Transverse - Max Principal Strain - a) Matrix/Fiber b) Matrix/Void

In comparison to the previous 40% and 50% fiber void models, the highest strain in the 60% fiber void model is the normal strain in the 2-direction. In the 40% and 50% fiber void models, shear strains and additional normal strains contribute to the overall strain response. The hysteresis plots for the two locations are plotted in Figure 75. Observing both hysteresis plots, the matrix/fiber experiences larger normal strains than the matrix/void polymer.



a)

b)

Figure 76 60% Fiber Volume - Void - Transverse – Hysteresis a) Matrix/Fiber b) Matrix/Void

The temperature increase for each model is significant. Figure 77 is the temperature versus time plot. As expected, because the 40% fiber volume has a lower traction load applied, it also experiences the smallest temperature increase. The 40% fiber volume, void configuration reaches 311.08 Kelvin at 30 minutes. Similarly, the 50% fiber volume reaches 315.68 Kelvin and the 60% fiber volume reaches 315.63 Kelvin at 30 minutes. At 30 minutes, the 60% fiber volume's internal temperature is 315.93 Kelvin.

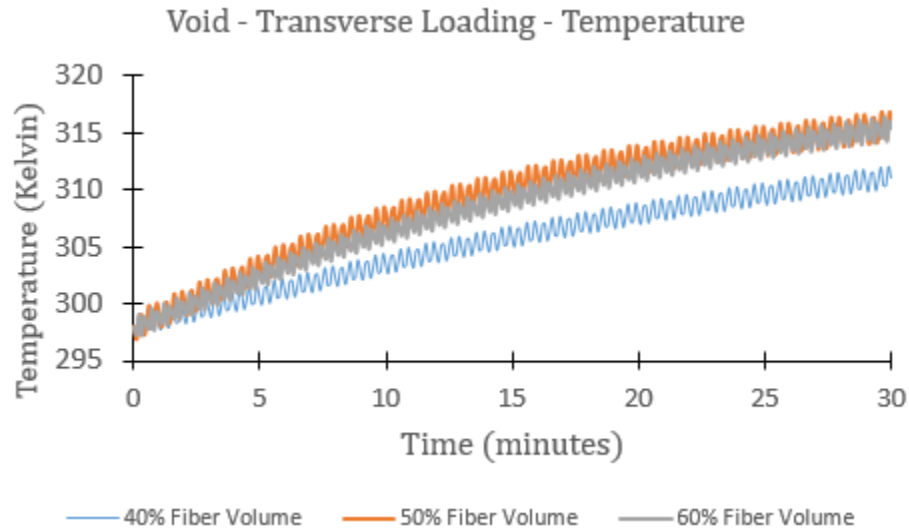
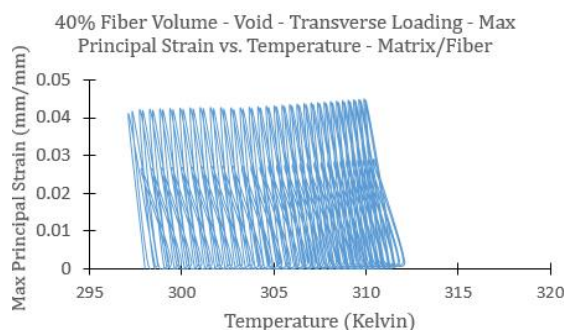
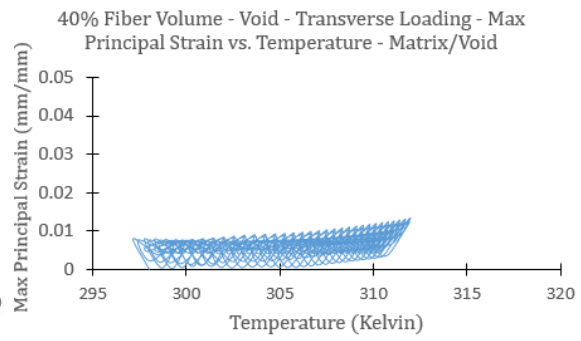


Figure 77 Void - Transverse Loading – Temperature

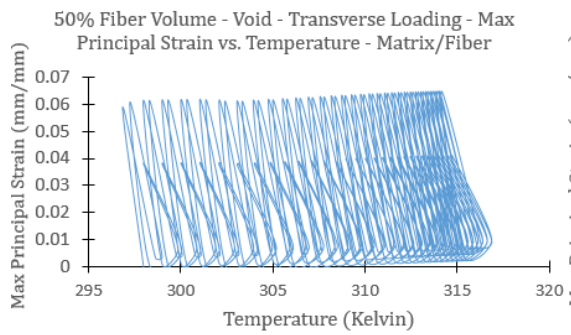
The principal strains for all three fiber content models are plotted against the respective temperatures in Figure 78. The principal strains in the matrix/fiber location are greater than 4%. The principal strains in the matrix/void locations are lower and vary 0.95% to 1.4%. From the previous temperature plot (Figure 77), the 40% fiber volume model has the smallest temperature increase because it is cycled with a 60 MPa traction load. In addition, the respective principal strains vs. temperature are summarized in Table 13.



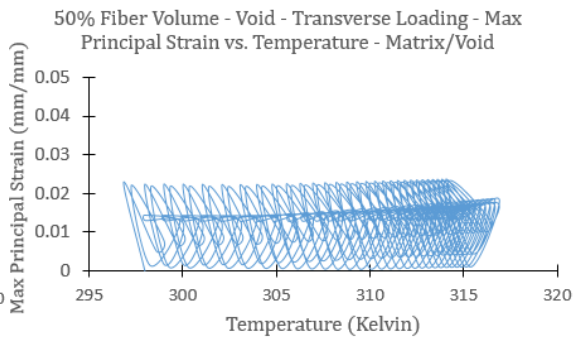
a)



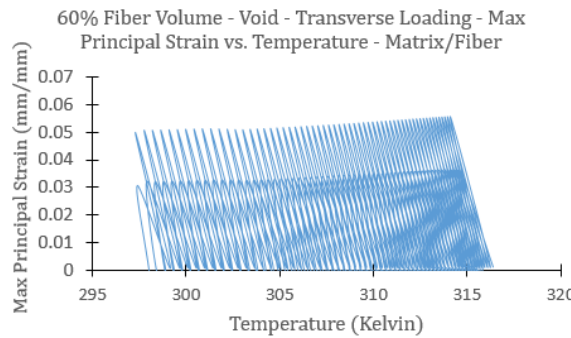
b)



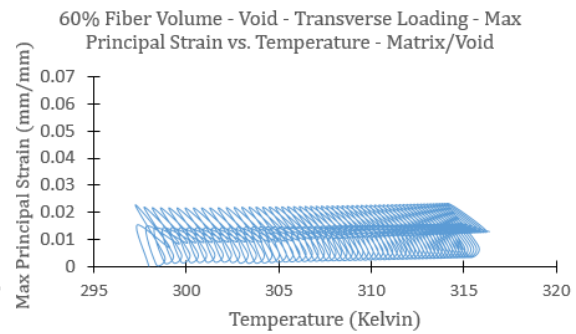
c)



d)



e)



f)

Figure 78 Max Principal Strain vs. Temperature – Transverse Loading – Void a) 40% Fiber Volume Matrix/Fiber b) 40% Fiber Volume Matrix/Void c) 50% Fiber Volume Matrix/Fiber d) 50% Fiber Volume Matrix/Void e) 60% Fiber Volume Matrix/Fiber f) 60% Fiber Volume Matrix/Void

Table 13 Max Principal Strain vs. Temperature - Void - Transverse Loading

Fiber Volume		40%	50%	60%	40%	50%	60%
Location		Matrix/Fiber			Matrix/Void		
Temperature (Kelvin)	305	4.28%	6.13%	5.15%	0.95%	1.41%	2.19%
	310	4.40%	6.31%	5.29%	1.20%	1.57%	2.23%
	315	N/A	6.47%	5.55%	N/A	1.65%	2.31%

8 SUMMARY AND CONCLUSION

This study investigates the performance of fiber reinforced polymer composites at the microscopic and macroscopic scales under cyclic loadings. For this purpose, carbon fiber reinforced composite finite elements are created and the influence of viscoelastic matrix on the response of composite is studied. The effect of energy dissipation from the viscoelastic polymers on the hysteretic responses of composites is examined. Furthermore, the finite element models are modified to include voids in order to evaluate the effect of defect on the overall mechanical response of composites. The composites are subjected to cyclic loading at different frequency and loading direction. The study demonstrates that the micromechanics of carbon fiber reinforced composite model vary substantially with respect to location and temperature in the composite thus confirming that our hypothesis holds true. Below are the summaries and conclusions from the study:

- (1) Stress fields and strain fields are substantially higher at matrix/fiber interfaces. This is observed for all fiber volume configurations (40%, 50% and 60%) and all load cases (longitudinal, transverse and shear). While the stress and strain field at the matrix/fiber interface are greater initially, the change in the stress/strain field is smaller throughout the load cycle. It can be assumed that the fibers surrounding the matrix “restrain” the polymer matrix and minimizing the viscoelastic effect.
- (2) Polymer matrix located relatively far apart from neighboring carbon fibers are susceptible to large strain deformations. The deformation is significant, often exceeding more than 5% in principal strain. The large strain deformation is most pronounced in the longitudinal loading followed by shear loading and transverse loading. In addition, voids introduced into the polymer matrix disturb the stress and strain contour field, causing the polymer to be susceptible to large strain deformation during longitudinal loading. Void models which are cyclic loaded in simple shear are sensitive to polymer deformation near the voids. However, the models that include void that are loaded in the transverse direction are less susceptible to polymer deformation near their voids. The void content for all finite

element models is less than 1%. Typical aerospace CFRCs cannot exceed void contents of more than 1.5% [30]. Polymer matrix near the edges or free surface of a fiber volume model are sensitive to the deformation regardless of loading direction. In general, 40% fiber models, where fibers are spaced relatively far apart (compared to 50% and 60% fiber models), show the greatest susceptibility to deformation. Burks et.al [18] observed similar results for their research. According to their research findings, for CFRCs with low fiber content ($<50\%$), the polymer matrix carries a substantial percentage of the load. Yet when the fiber content is increased, the fibers will carry a greater percentage of the overall load and reduce the axial stress in the polymer matrix. However, their research determined that increasing the fiber volume content past 68%, the inter-fiber spacing becomes sufficiently small to create stress risers in the polymer matrix.

- (3) Temperature changes are significant and observed for all three loading directions. For the same displacement applied, the longitudinally loaded fiber models show the highest increase in temperature. The shear and transverse loaded models experience smaller temperature increases in comparison to the longitudinally loaded models. Within the same load cases, the temperature change across different fiber volumes differ slightly for the longitudinal and transverse loading directions. However, the fiber volumes do affect the temperature change for the shear load cases. The 60% fiber volume, shear loaded, generates the greatest temperature increase followed by the 50% and 40% fiber volume. In addition, the temperature distributions is uniform throughout the microstructures due to the conduction of heat. This is due to the fact that loading is relatively slow and allows the heat to reach steady state.
- (4) The cyclic frequency does affect the rate of temperature increase. For the longitudinal loading cases, when the frequency is changed from 2/60 Hz to 3/60 Hz, no significant difference is observed in the rate of temperature change. However, when the cyclic frequency is increased to 5/60 Hz or 10/60 Hz, the temperature rate increase becomes significant. The frequency study used a

displacement amplitude of 0.0075 mm instead of the usual 0.02 mm. The displacement amplitude correlates to longitudinal strains of 0.75% vs. 2% respectively. Even with a lower displacement load applied, in the model with 40% fiber volume content, the polymer matrix experienced excessive deformation within 7 minutes of loading. Consequentially, the finite element analysis failed to converge.

The hysteretic response of the micromechanical field variables differs from that of the homogenized response. The homogenized (macroscopic) response show a relatively small hysteretic of an ellipsoidal shape, which suggest a linear viscoelastic response. However, the hysteretic response at the microscopic scale (at the matrix regions at various locations) shows highly nonlinear shape with large hysteretic area. In some cases, the strain amplitude increases significantly, which could cause damage/failure in the composites.

The thermo-mechanical CFRC FEM is a valuable tool that allows researchers and engineers to study the effect of energy dissipation on the micromechanical field variables in CFRC under cyclic loading. However, the material subroutine is limited because it is a viscoelastic material subroutine and does not model viscoplasticity or damage in the polymer matrix. Within the results, strain and stresses routinely exceeded 5% and 50 MPa respectively. FM73, which is a brittle polymer adhesive, will fail when these strains and stresses are exceeded [31]. Therefore one has to be cautious when presenting the study's results with respect to damage initiation.

In addition, crack growth at the voids should be studied by expanding the material subroutine to include crack initiation parameters. In Appendix B, a 2D 60% fiber content model is created with an ellipsoidal void to simulate crack propagation in finite element models. The fully-coupled thermo-mechanical nonlinear viscoelastic material subroutine is used. An initial temperature for all nodes is specified, however, the elements do not allow for heat conduction within the model. The ellipsoidal void is placed between two fibers. Plane strain elements are needed because 3D finite elements are computationally expensive and contact stress convergence is problematic. Parameters varied include fiber spacing and initial temperature. The finite element model is loaded in both transverse and

shear direction and the crack initiation load is measured. The results indicate that fiber spacing and temperature have a significant effect on the crack onset, however, the model has its limitations. First, it is a 2D plane-strain finite element model and therefore can only accurately model thin CFRP plates. Second, the current plane strain element formulations for ABAQUS do not allow for temperature conduction. Therefore the heat dissipation and hysteresis of CFRP is not accurately captured if subjected to cyclic loading. Instead, the simulation only includes quasi-static ramp loading. Khan and Muliana made significant progress developing a viscoelastic material subroutine for FM73. In addition, the material parameters can be expanded to include common aerospace epoxy and adhesives. Expanding the material subroutine and the material database will allow us to study crack initiation loads in a 3D finite element model with a full thermo-mechanical material model for a variety of aerospace polymers.

REFERENCES

- [1] J. Eshelby, "The Determination of The Field of an Ellipsoidal Inclusion and Related Problems," *Proc. R. Soc.*, vol. A, no. No. 241, pp. 376–396, 1957.
- [2] Z. Hashin, "The Moduli of an Elastic Solid Containing Spherical Particles of Another Elastic Material," *Nonhomogeneity Elast. Plast.*, pp. 463–478, 1959.
- [3] W. Stinchomb and K. Reifsnider, "Fatigue Damage Mechanisms in Composite Materials: A Review," in *Proceedings of an ASTM-NBS-NSF symposium*, 1979, pp. 762–787.
- [4] A. L. Highsmith and K. L. Reifsnider, "Stiffness-reduction mechanisms in composite laminates," *ASTM STP*, vol. 775, pp. 103–117, 1982.
- [5] Z. Hashin, "Analysis of stiffness reduction of cracked cross-ply laminates," *Eng. Fract. Mech.*, vol. 25, no. 5–6, pp. 771–778, 1986.
- [6] V. Vinogradov and Z. Hashin, "Variational analysis of cracked angle-ply laminates," *Compos. Sci. Technol.*, vol. 70, no. 4, pp. 638–646, 2010.
- [7] R. Talreja, "Damage and fatigue in composites - A personal account," *Compos. Sci. Technol.*, vol. 68, no. 13, pp. 2585–2591, 2008.
- [8] D. Krajcinovic, "Continuous Damage Mechanics Revisited: Basic Concepts and Definitions," *J. Appl. Mech.*, vol. 52, no. 4, pp. 829–834, 1985.
- [9] J. Aboudi, *Mechanics of Composite Materials: A Unified Micromechanical Approach*, 1st ed. Amsterdam: Elsevier, 1991.
- [10] M. C. Lafarie-Frenot, C. Hénaff-Gardin, and D. Gamby, "Matrix cracking induced by cyclic ply stresses in composite laminates," *Compos. Sci. Technol.*, vol. 61, no. 15, pp. 2327–2336, 2001.
- [11] V. Bellenger, A. Tcharkhtchi, and P. Castaing, "Thermal and mechanical fatigue of a PA66/glass fibers composite material," *Int. J. Fatigue*, vol. 28, no. 10 SPEC. ISS., pp. 1348–1352, 2006.
- [12] D. Rittel and Y. Rabin, "An investigation of the heat generated during cyclic loading of two glassy polymers. Part II: Thermal analysis," *Mech. Mater.*, vol. 32, pp. 149–159, 2000.
- [13] J. W. Holmes and C. Cho, "Experimental Observations of Frictional Heating in Fiber-Reinforced Ceramics," *J. Am. Ceram. Soc.*, vol. 75, no. 4, pp. 929–938, 1992.

- [14] L. Toubal, M. Karama, and B. Lorrain, "Damage evolution and infrared thermography in woven composite laminates under fatigue loading," *Int. J. Fatigue*, vol. 28, no. 12, pp. 1867–1872, 2006.
- [15] H. Mivehchi and A. Varvani-Farahani, "The effect of temperature on fatigue strength and cumulative fatigue damage of FRP composites," *Procedia Eng.*, vol. 2, no. 1, pp. 2011–2020, 2010.
- [16] M. Bureau and J. Denault, "Fatigue Resistance of Continuous Glass Fiber / Polypropylene Composites : Temperature Dependence," *Polym. Compos.*, vol. 25, no. 6, pp. 622–629, 2004.
- [17] H. Li and B. Zhang, "A new viscoelastic model based on generalized method of cells for fiber-reinforced composites," *Int. J. Plast.*, vol. 65, pp. 22–32, 2015.
- [18] B. Burks, J. Middleton, and M. Kumosa, "Micromechanics modeling of fatigue failure mechanisms in a hybrid polymer matrix composite," *Compos. Sci. Technol.*, vol. 72, no. 15, pp. 1863–1869, 2012.
- [19] A. R. Maligno, N. A. Warrior, and A. C. Long, "European Journal of Mechanics A / Solids Effects of inter-fibre spacing on damage evolution in unidirectional (UD) fibre-reinforced composites," *Eur. J. Mech. A/Solids*, vol. 28, no. 4, pp. 768–776, 2009.
- [20] K. A. Khan and A. H. Muliana, "Fully coupled heat conduction and deformation analyses of nonlinear viscoelastic composites," *Compos. Struct.*, vol. 94, no. 6, pp. 2025–2037, 2012.
- [21] K. A. Khan and A. H. Muliana, "Fully coupled heat conduction and deformation analyses of visco-elastic solids," *Mech. Time-Dependent Mater.*, vol. 16, no. 4, pp. 461–489, 2012.
- [22] R. Schapery, "Further development of a thermodynamic constitutive theory: stress formulation," *Purdue University Report No.AA & ES. 692*. 1969.
- [23] R. . Schapery, "Nonlinear viscoelastic and viscoplastic constitutive equations based on thermodynamics," *Mech. Time-Dependent Mater.*, vol. 1, pp. 209–240, 1997.
- [24] Hexcel, "HexTow AS4," 2016. [Online]. Available: <http://www.hexcel.com/Resources/DataSheets/Carbon-Fiber-Data-Sheets/AS4.pdf>. [Accessed: 01-Jan-2016].
- [25] H. Hu and C. T. Sun, "The characterization of physical aging in polymeric composites," *Compos. Sci. Technol.*, vol. 60, no. 14, pp. 2693–2698, 2000.

- [26] A. Muliana and K. A. Khan, "A time-integration algorithm for thermorheologically complex polymers," *Comput. Mater. Sci.*, vol. 41, no. 4, pp. 576–588, 2008.
- [27] D. Peretz and Y. Weitsman, "Nonlinear Viscoelastic Characterization of FM-73 Adhesive," *J. Rheol. (N. Y. N. Y.)*, vol. 26, no. 3, p. 245, 1982.
- [28] D. Peretz and Y. Weitsman, "The Nonlinear Thermoviscoelastic Characterizations of FM- 73 Adhesives," *J. Rheol. (N. Y. N. Y.)*, vol. 27, no. 2, pp. 97–114, 1983.
- [29] A. Muliana and K. . Khan, "A time-integration algorithm for thermorheologically complex polymers," *Comput. Mater. Sci.*, vol. 41, no. 4, pp. 576–588, 2008.
- [30] S. R. Ghiorse, "A Comparison of Void Measurement Methods for Carbon/Epoxy Composites - A236438," 1991. [Online]. Available: <http://www.dtic.mil/get-tr-doc/pdf?AD=ADA236438>. [Accessed: 01-Jan-2016].
- [31] Cytec, "MatWeb Cytec FM 73 Epoxy Film Adhesive," 2017. [Online]. Available: <http://www.matweb.com/search/datasheettext.aspx?matguid=7a4bae930fb9427baf033747c9745460>. [Accessed: 03-Mar-2017].
- [32] S. Roy and J. Reddy, "A Finite Element Analysis of Adhesively Diffusion and Delayed Failure," *Comput. Struct.*, vol. 29, no. 6, pp. 1011–1031, 1988.
- [33] W. C. Carpenter, "Viscoelastic analysis of bonded connections," *Comput. Struct.*, vol. 36, no. 6, pp. 1141–1152, 1990.
- [34] S. Yadagiri, C. Reddy, and T. Reddy, "Viscoelastic analysis of adhesively bonded joints," *Comput. Struct.*, vol. 27, no. 4, p. 445, 1987.
- [35] N. Choupani, "Characterization of fracture in adhesively bonded double-lap joints," *Int. J. Adhes. Adhes.*, vol. 29, no. 8, pp. 761–773, 2009.
- [36] S. K. Panigrahi and B. Pradhan, "Through-the-width delamination damage propagation characteristics in single-lap laminated FRP composite joints," *Int. J. Adhes. Adhes.*, vol. 29, no. 2, pp. 114–124, 2009.
- [37] A. Needleman, "An analysis of tensile decohesion along an interface," *J. Mech. Phys. Solids*, vol. 38, no. 3, pp. 289–324, 1990.
- [38] V. Tvergaard and J. W. Hutchinson, "On the toughness of ductile adhesive joints," *J. Mech. Phys. Solids*, vol. 44, no. 5, pp. 789–800, 1996.
- [39] J. A. B. P. Neto, R. D. S. G. Campilho, and L. F. M. Da Silva, "Parametric study of adhesive joints with composites," *Int. J. Adhes. Adhes.*, vol. 37, pp. 96–101, 2012.

- [40] D. H. Allen and C. R. Searcy, “A micromechanical model for a viscoelastic cohesive zone,” *Int. J. Fract.*, vol. 107, no. 2, pp. 159–176, 2001.
- [41] Dassault, “ABAQUS 6.14 Manual.” [Online]. Available: <http://bobcat.nus.edu.sg:2080/v6.14/books/usb/default.htm?startat=pt04ch11s04aus69.html#usb-anl-acrackpropagation>. [Accessed: 06-Jan-2017].

APPENDIX A

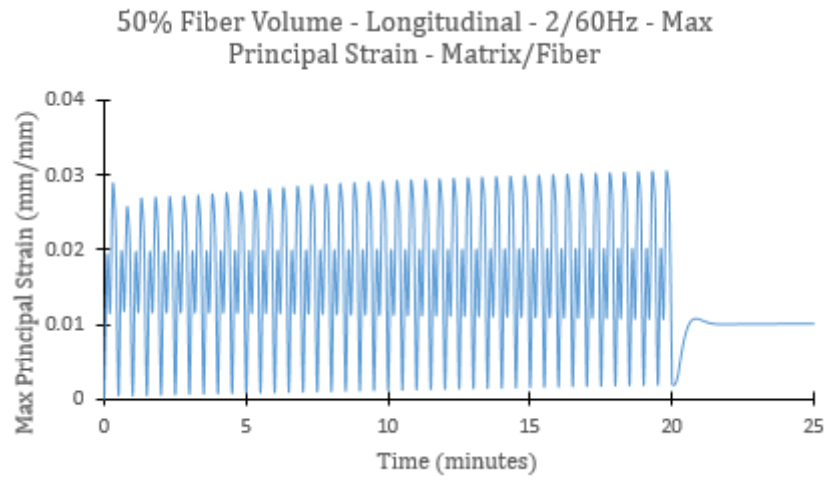


Figure A-1 50% Fiber Volume – 2/60 Hz – 0.02 Disp. – Max Principal Strain

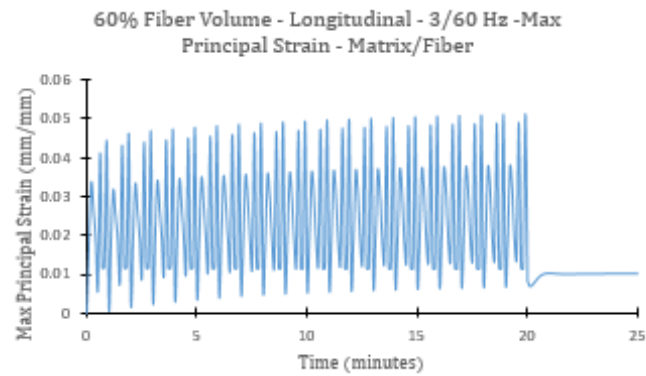


Figure A-2 60% Fiber Volume – 3/60 Hz – 0.02 Disp. – Max Principal Strain

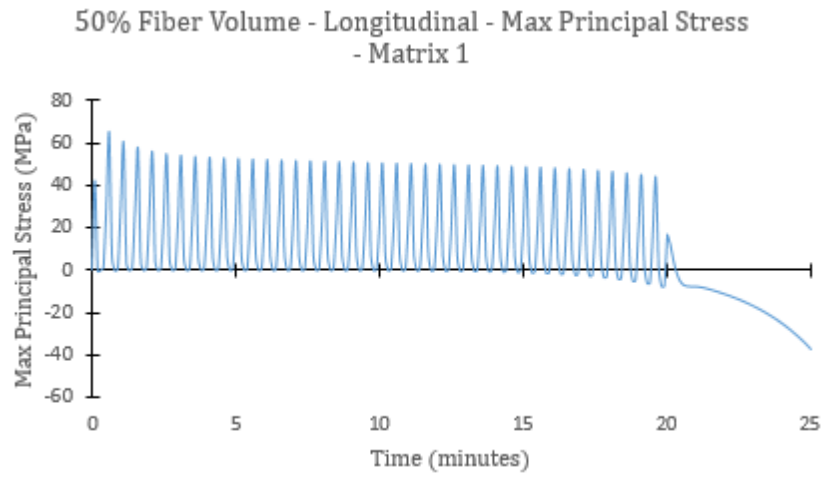


Figure A-3 50% Fiber Volume – Matrix 1 Location – Max Principal Stress

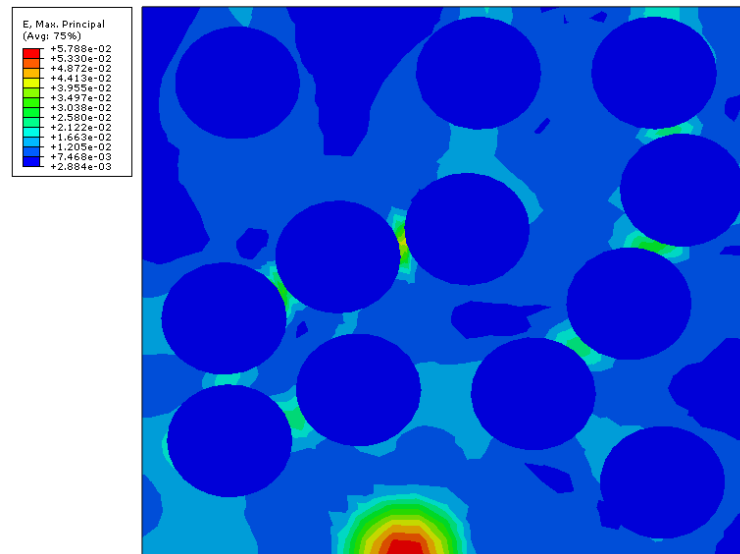


Figure A-4 40% Fiber Volume Longitudinal – Edge Effect Matrix Softening

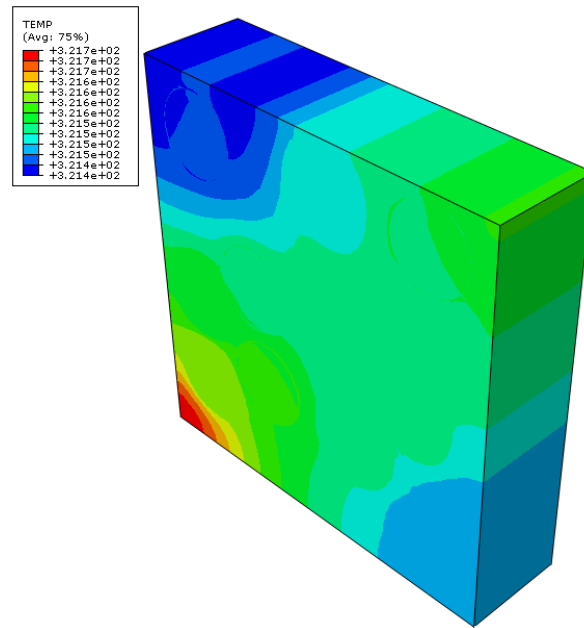


Figure A-5 40% Fiber Volume Longitudinal – Temperature – 5 minutes

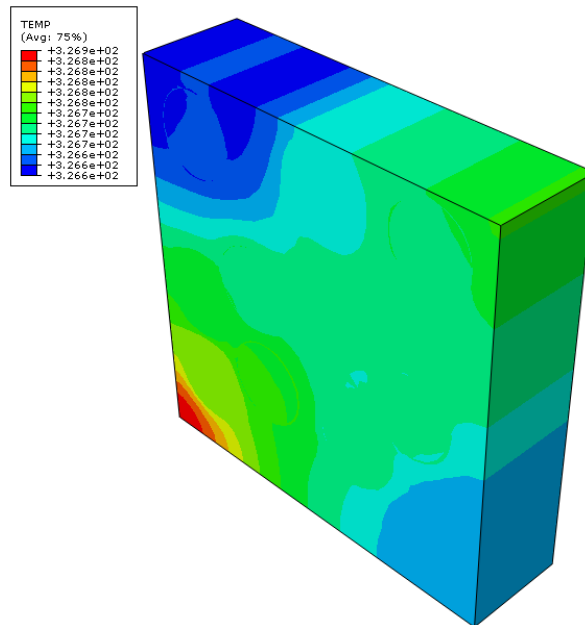


Figure A-6 40% Fiber Volume Longitudinal – Temperature – 10 minutes

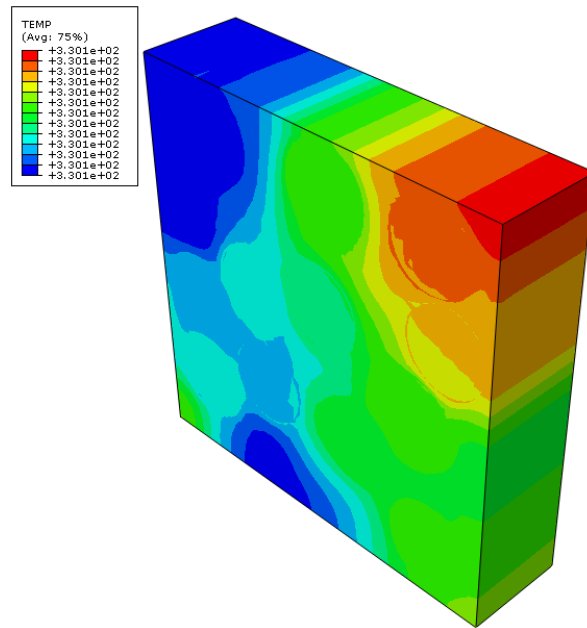


Figure A-7 40% Fiber Volume Longitudinal – Temperature – 13.4 minutes

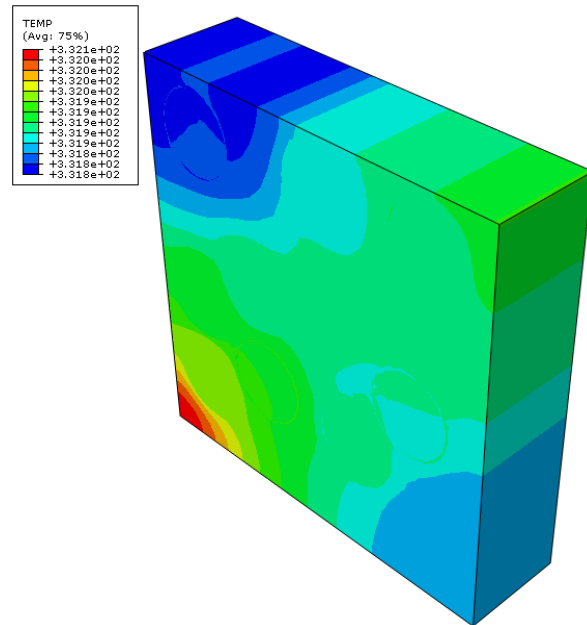


Figure A-8 40% Fiber Volume Longitudinal – Temperature – 20 minutes

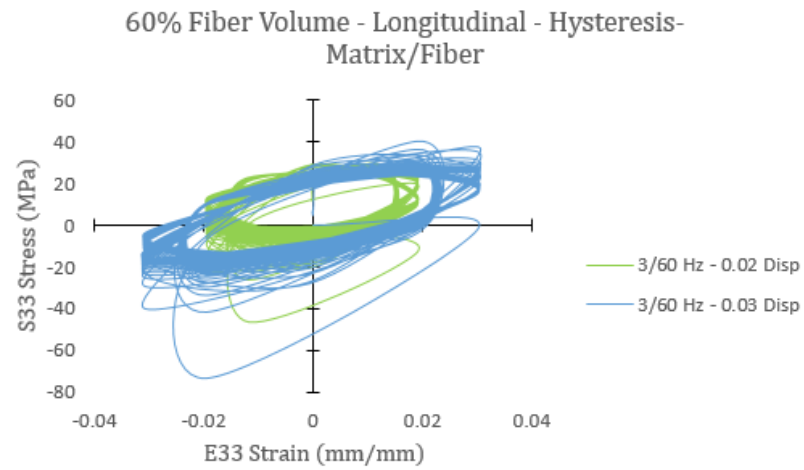


Figure A-9 60% Fiber Volume – Longitudinal – Displacement Boundary – Hysteresis

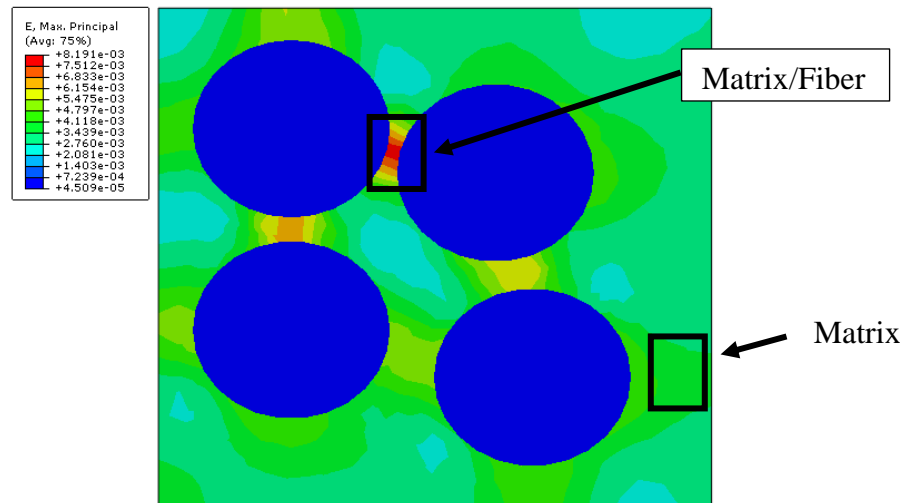


Figure A-10 40% Fiber Volume – Longitudinal – 5/60 Hz – 0.300 minutes – Regions of Interest

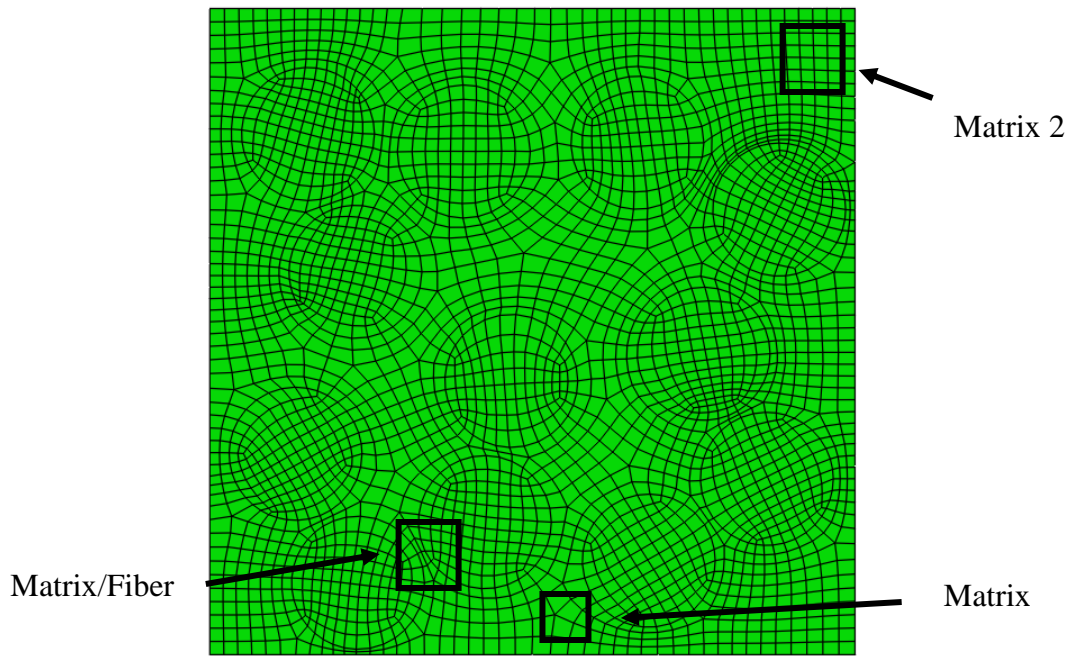


Figure A-11 40% Fiber Volume Pristine– Shear Loading – Regions of Interest

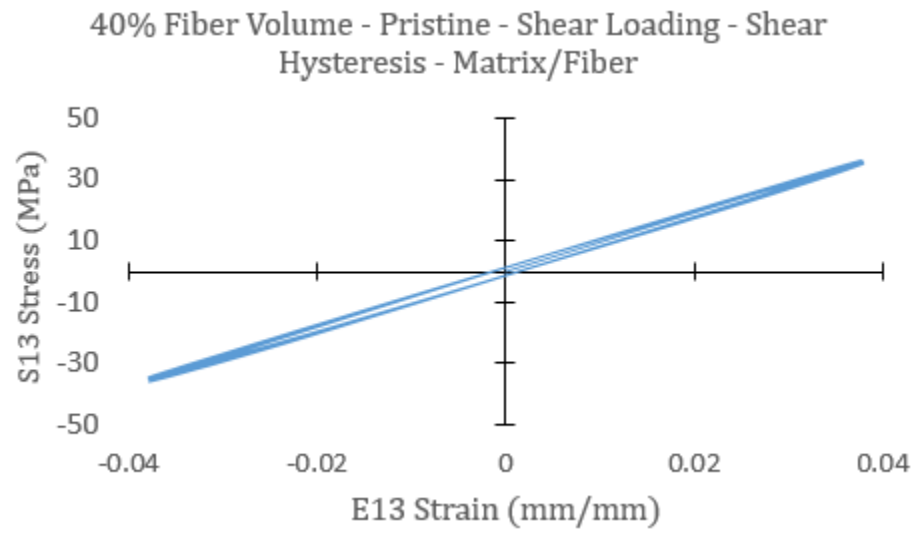


Figure A-12 40% Fiber Volume Pristine– Shear Loading – Shear Hysteresis – Matrix/Fiber

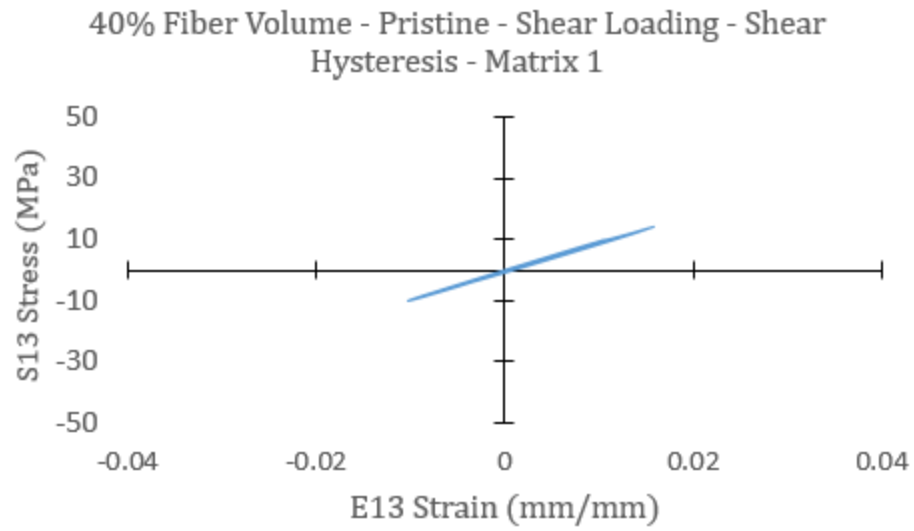


Figure A-13 40% Fiber Volume Pristine– Shear Loading – Shear Hysteresis – Matrix 1

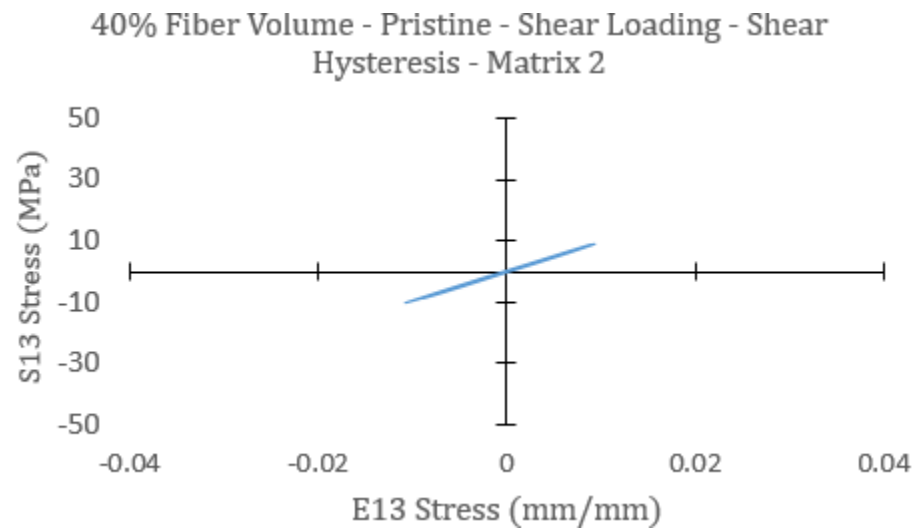


Figure A-14 40% Fiber Volume Pristine– Shear Loading – Shear Hysteresis – Matrix 2

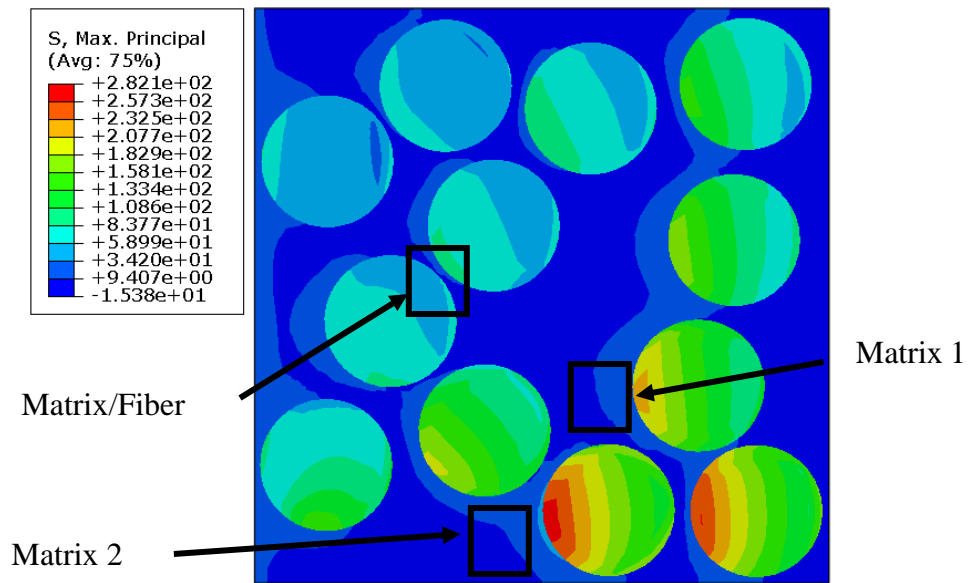


Figure A-15 50% Fiber Volume Pristine - Shear Loading - Regions of Interest

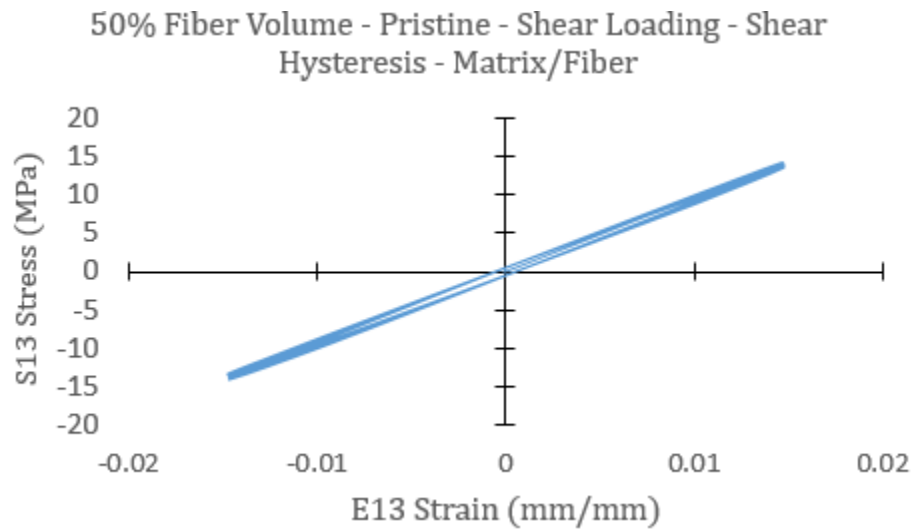


Figure A-16 50% Fiber Volume Pristine - Shear Loading - Shear Hysteresis - Matrix/Fiber

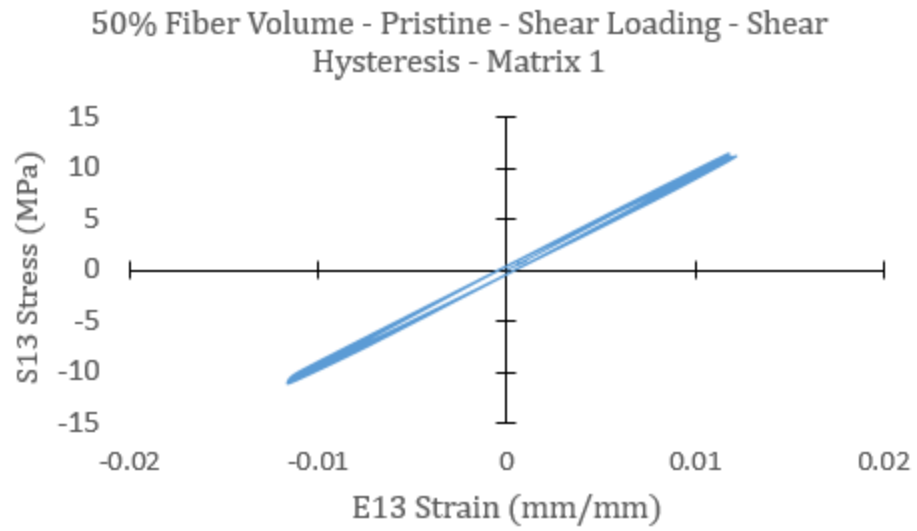


Figure A-17 50% Fiber Volume Pristine– Shear Loading – Shear Hysteresis – Matrix 1

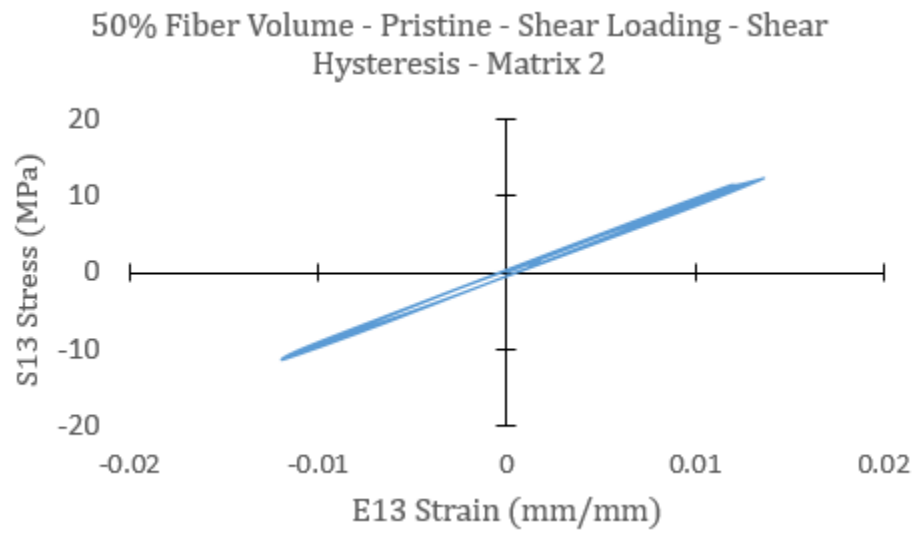


Figure A-18 50% Fiber Volume Pristine– Shear Loading – Shear Hysteresis – Matrix 2

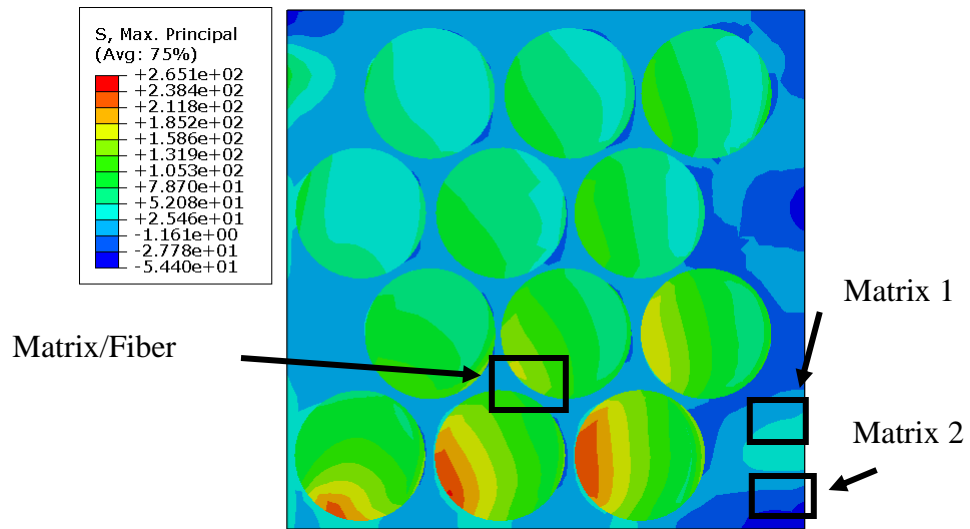


Figure A-19 60% Fiber Volume Pristine– Shear Loading – Regions of Interest

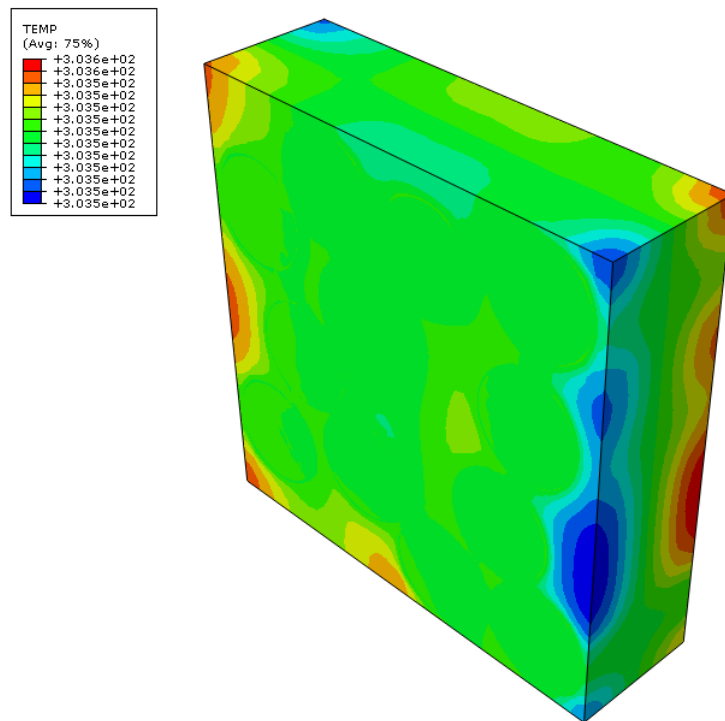


Figure A-20 50% Fiber Volume Pristine– Shear Loading – Temperature – 1 minute

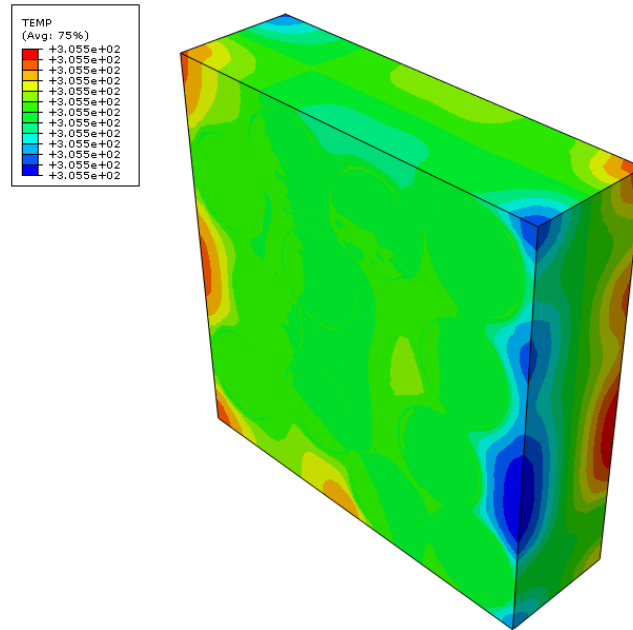


Figure A-21 50% Fiber Volume Pristine– Shear Loading – Temperature – 5 minute

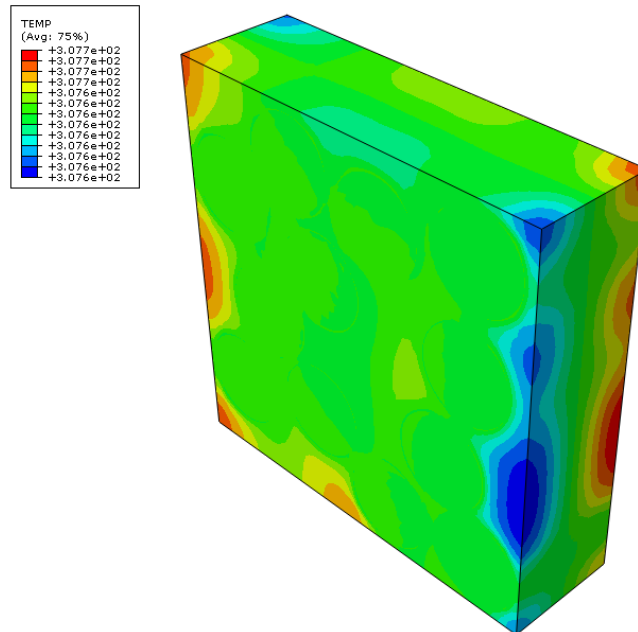


Figure A-22 50% Fiber Volume Pristine– Shear Loading – Temperature – 10 minute

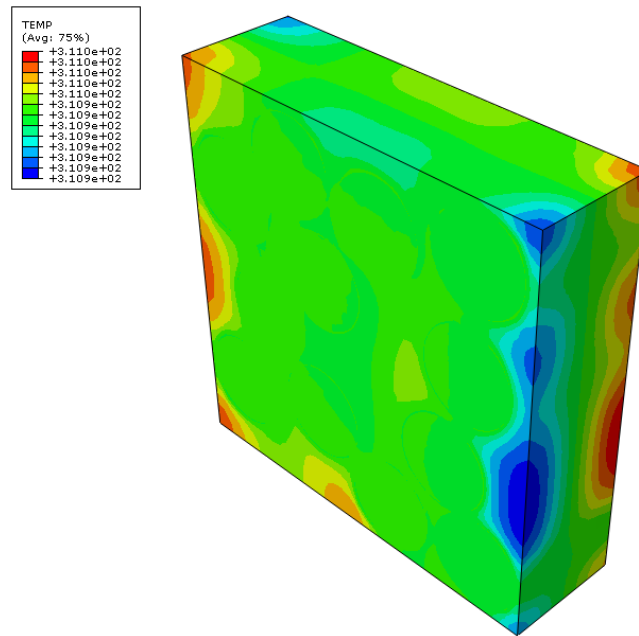


Figure A-23 50% Fiber Volume Pristine– Shear Loading – Temperature – 20 minutes

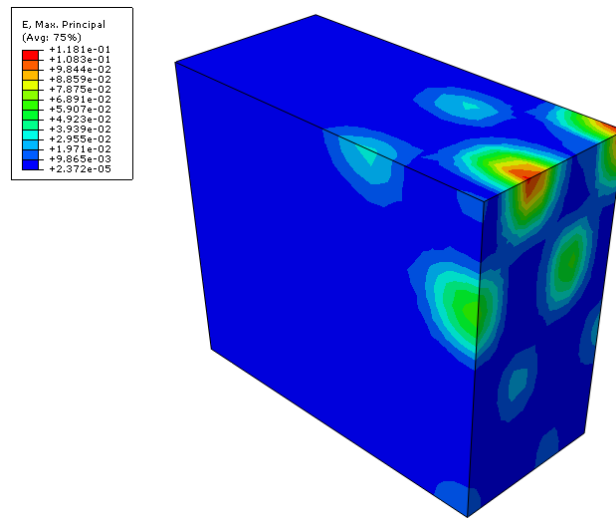


Figure A-24 40% Fiber Volume Pristine– Transverse – Max Principal Strain – 30 minutes

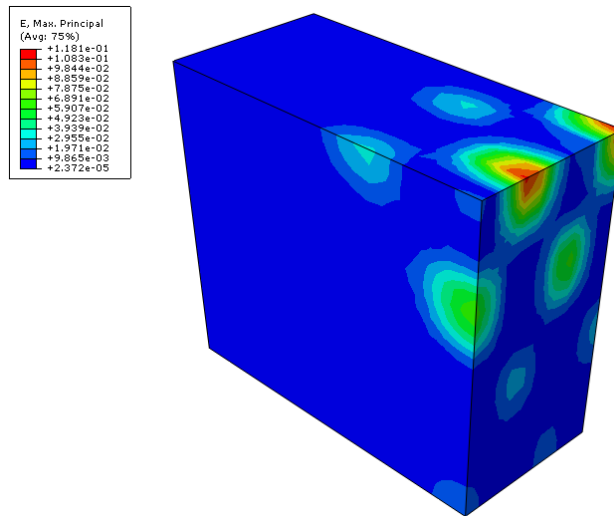


Figure A-25 40% Fiber Volume Pristine– Transverse – Max Principal Strain – 30 minutes

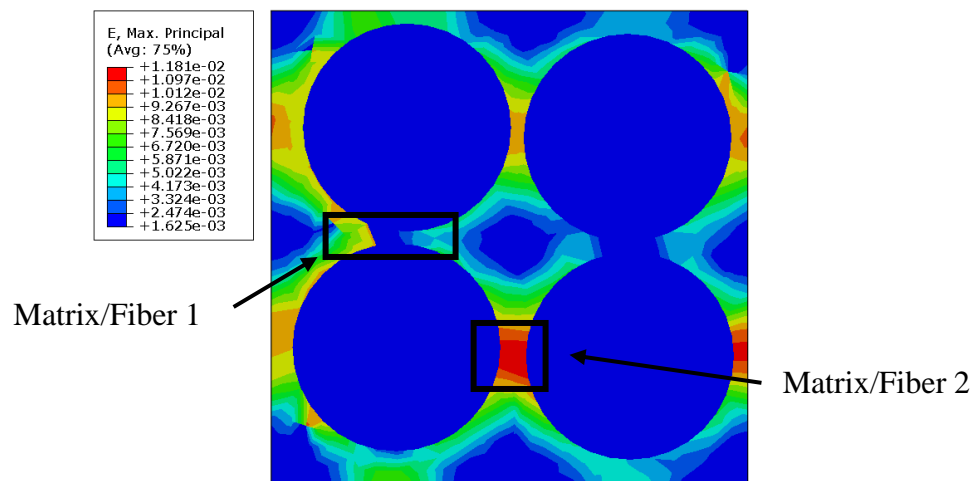


Figure A-26 60% Fiber Volume Pristine– Transverse – Max Principal Strain – 29.3 minutes

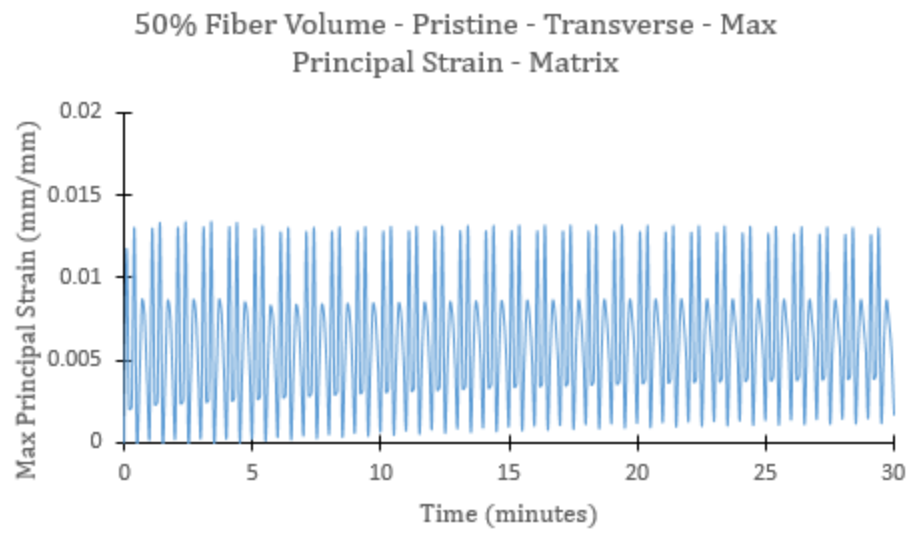


Figure A-27 50% Fiber Volume Pristine– Transverse – Max Principal Strain – Matrix

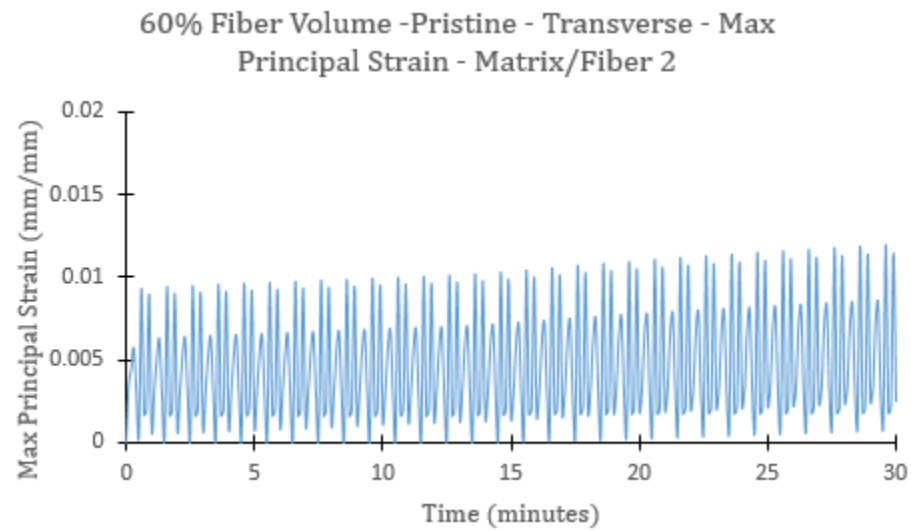


Figure A-28 60% Fiber Volume Pristine– Transverse – Max Principal Strain – Matrix/Fiber 2

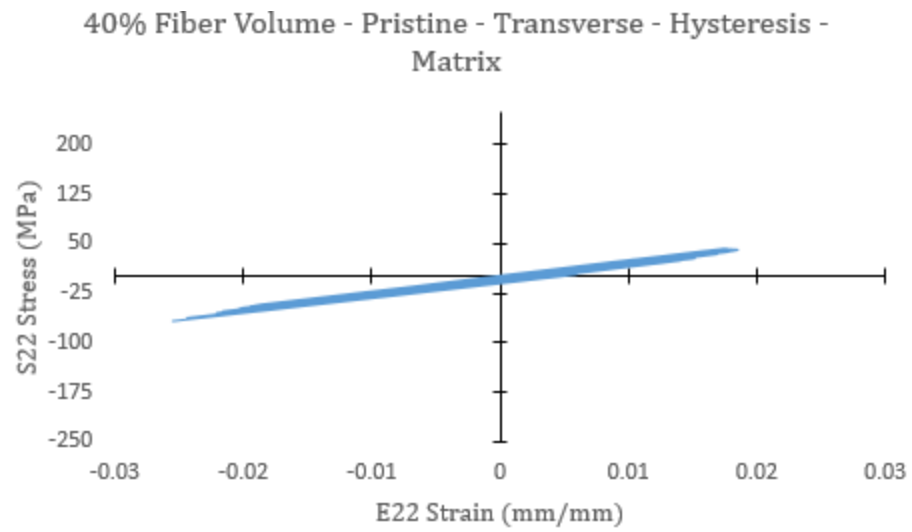


Figure A-29 40% Fiber Volume Pristine– Transverse – Hysteresis - Matrix

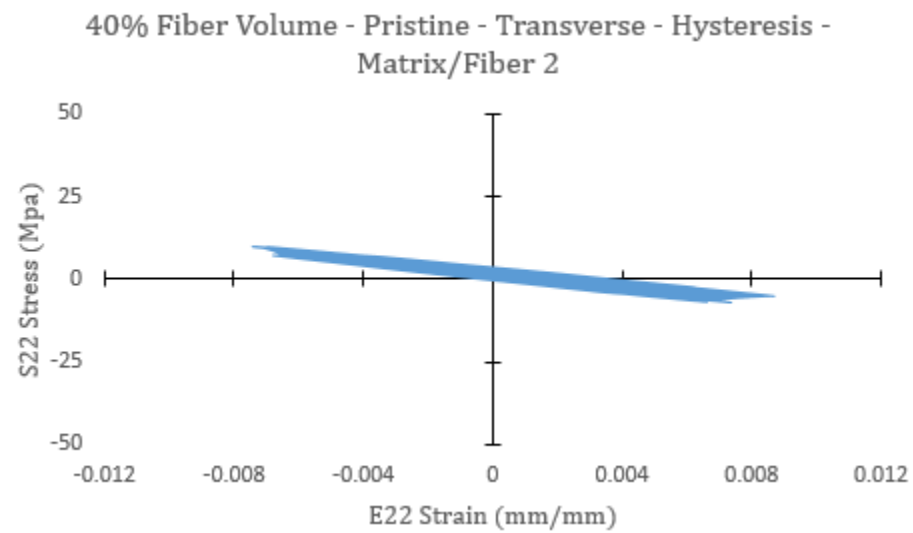


Figure A-30 40% Fiber Volume Pristine– Transverse – Hysteresis – Matrix/Fiber 2

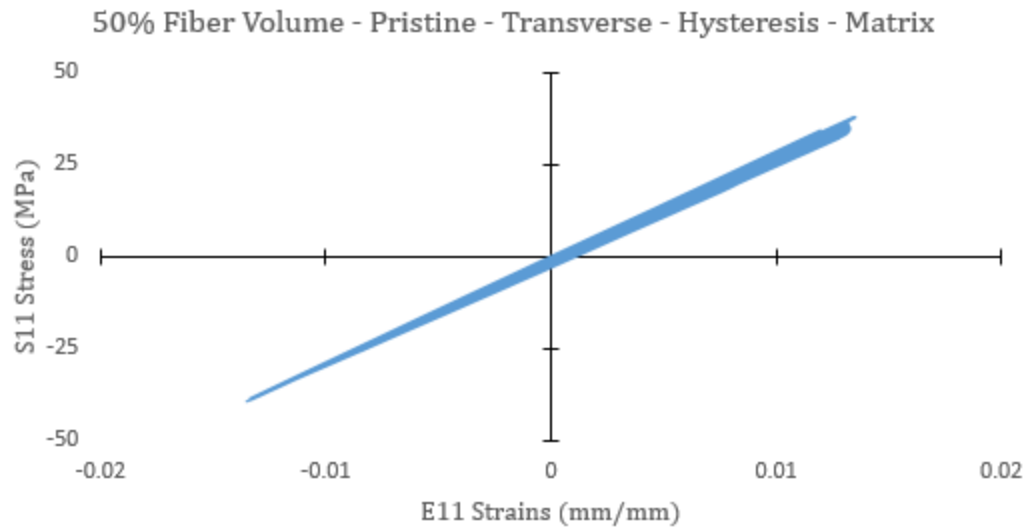


Figure A-31 50% Fiber Volume Pristine– Transverse – Hysteresis – Matrix

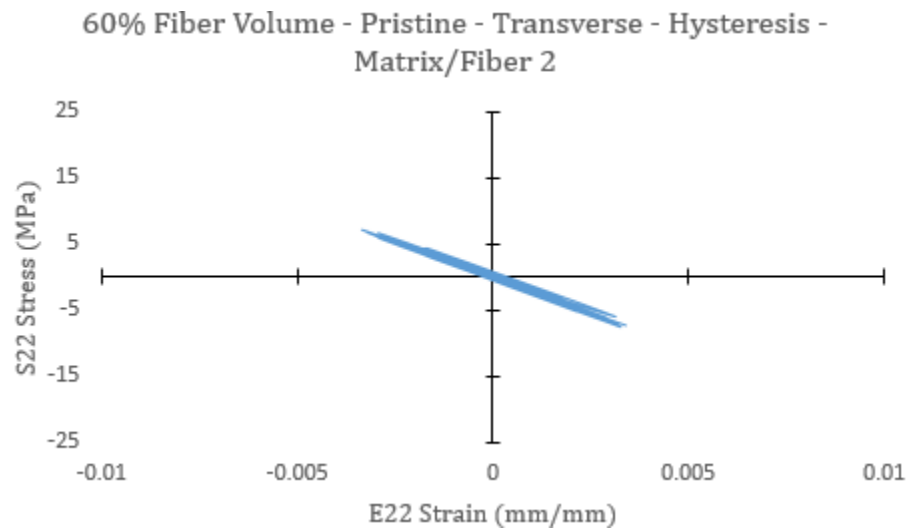


Figure A-32 60% Fiber Volume Pristine– Transverse – Hysteresis – Matrix/Fiber 2

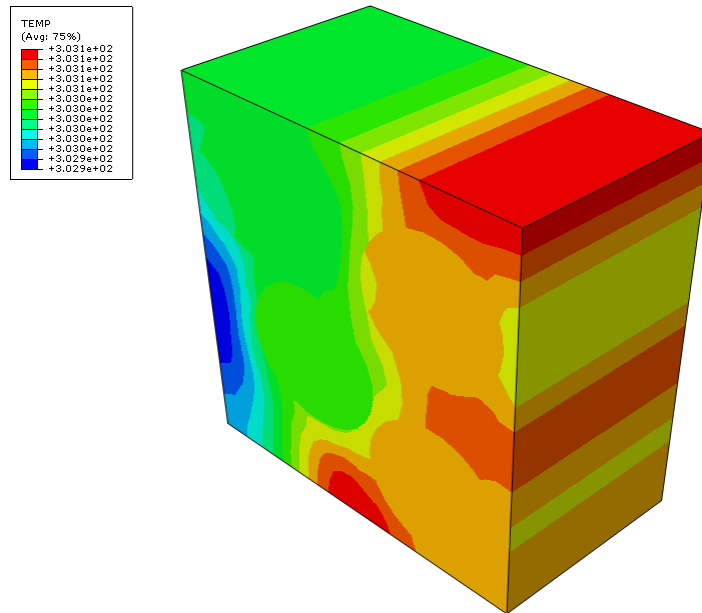


Figure A-33 50% Fiber Volume Pristine– Transverse Loading – Temperature – 5 minutes

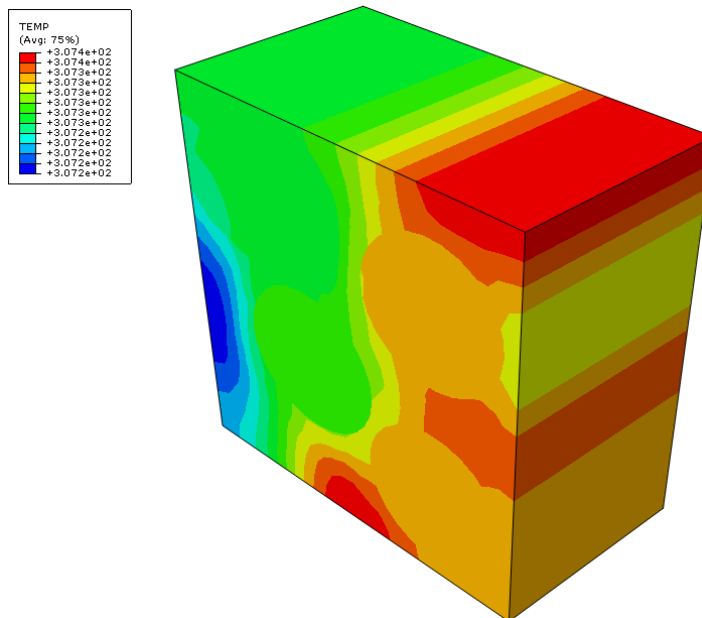


Figure A-34 50% Fiber Volume Pristine– Transverse Loading – Temperature – 10 minutes

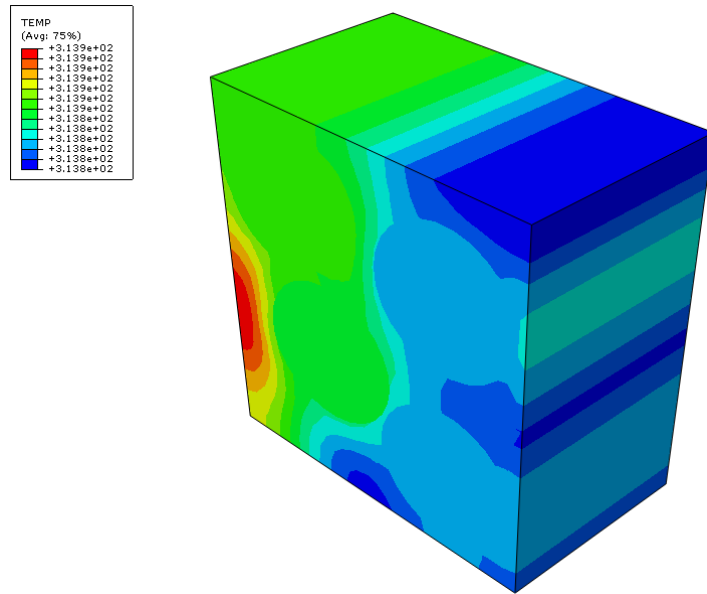


Figure A-35 50% Fiber Volume Pristine– Transverse Loading – Temperature – 14.9 minutes

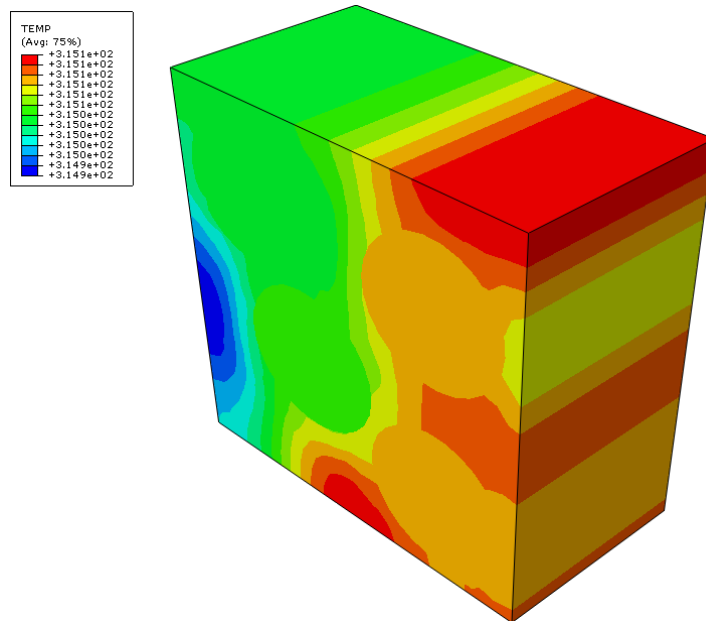


Figure A-36 50% Fiber Volume Pristine– Transverse Loading – Temperature – 28 minutes

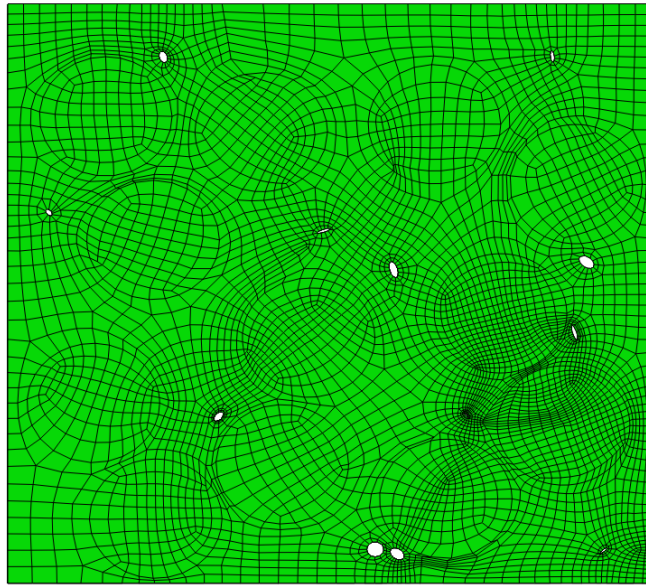


Figure A-37 40% Fiber Volume – Void Configuration

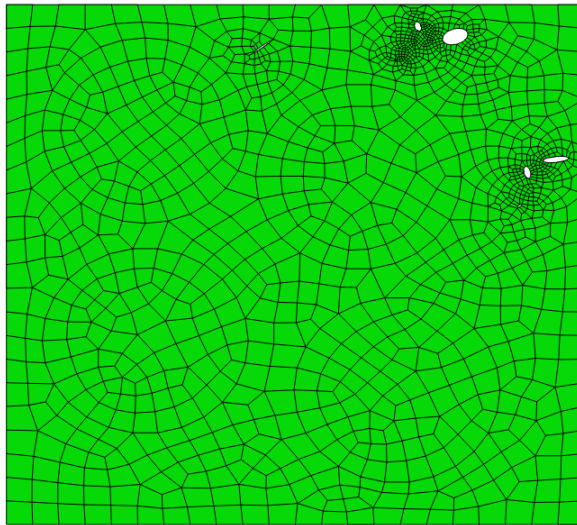


Figure A-38 40% Fiber Volume – Void Configuration – Transverse Loading

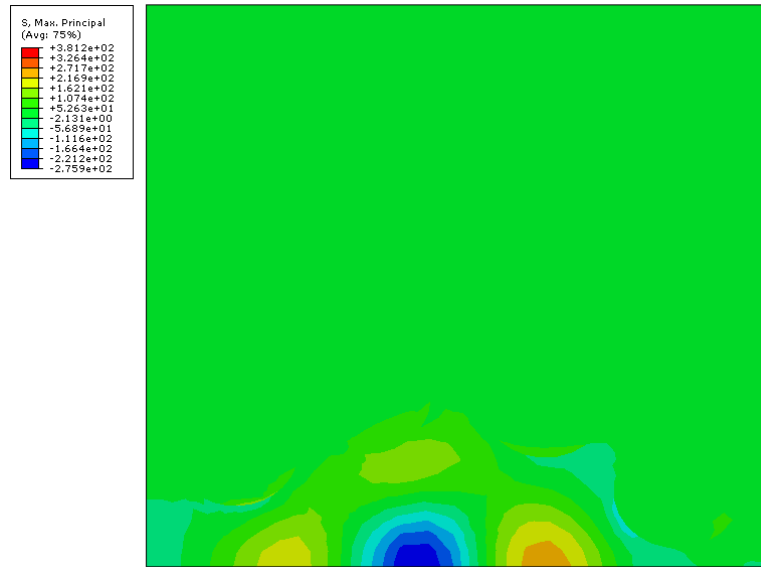


Figure A-39 40% Fiber Volume - 2/60 Hz - Longitudinal Loading - Max Principal Stress - 25 minutes

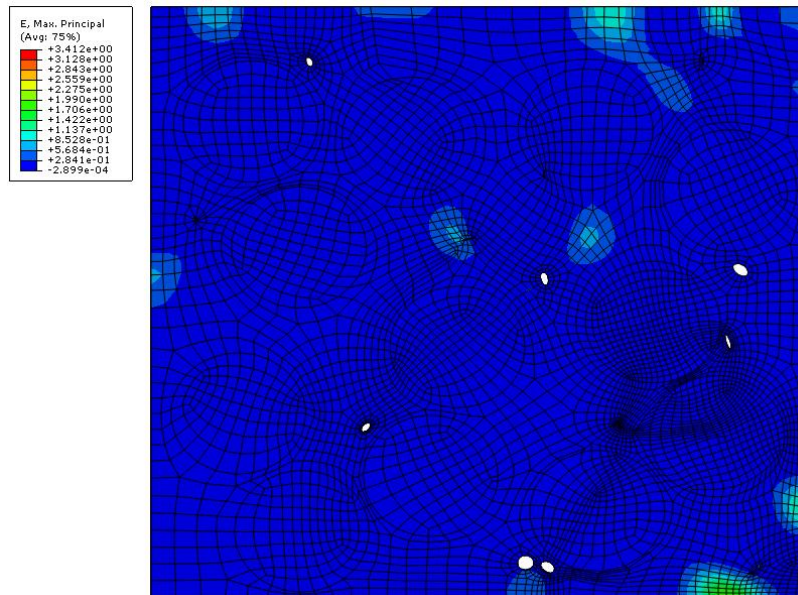


Figure A-40 – 40% Fiber Volume – Void – Longitudinal – Max Principal Strain – 23.5 minutes

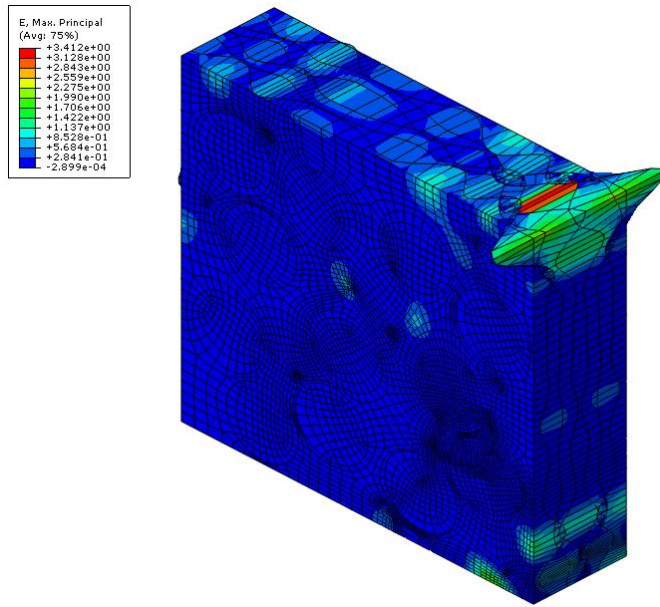


Figure A-41 – 40% Fiber Volume – Void – Longitudinal – Max Principal Strain – 23.5 minutes – Isometric View

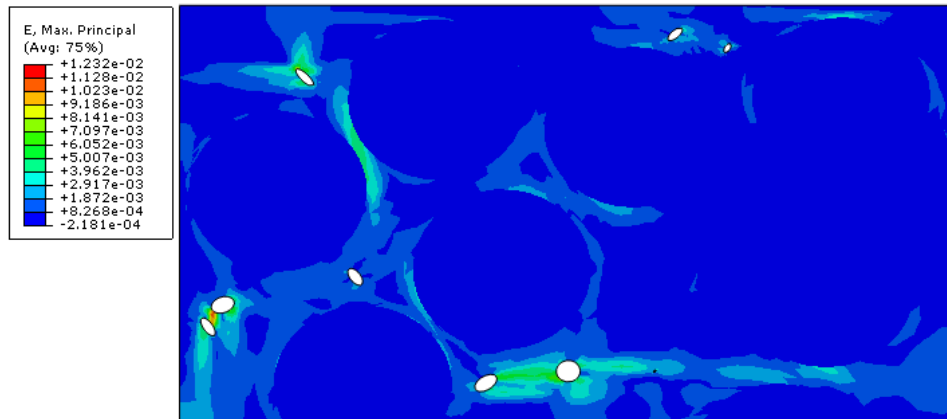


Figure A-42 50% Fiber Volume – Void Configuration – Longitudinal Loading – Max Principal Strain – 19.5 minutes – Close-up View

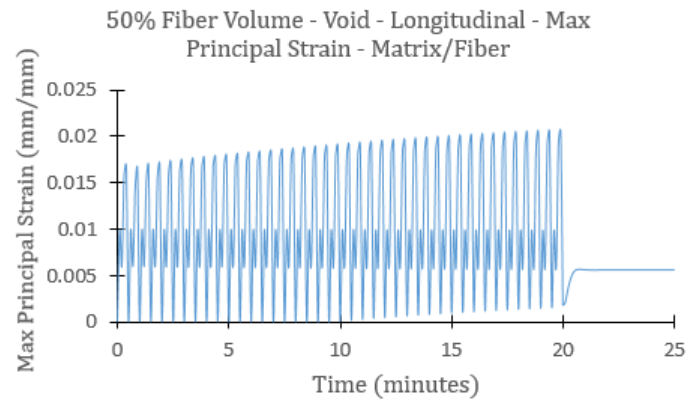


Figure A-43 50% Fiber Volume – Void Configuration – Longitudinal Loading – Max Principal Strain – Matrix/Fiber

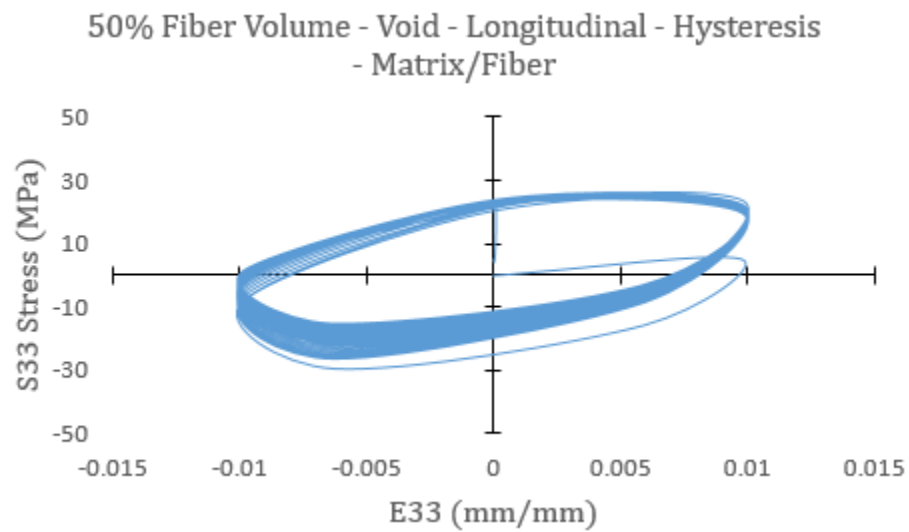


Figure A-44 50% Fiber Volume – Void Configuration – Longitudinal Loading – Hysteresis - Matrix/Fiber

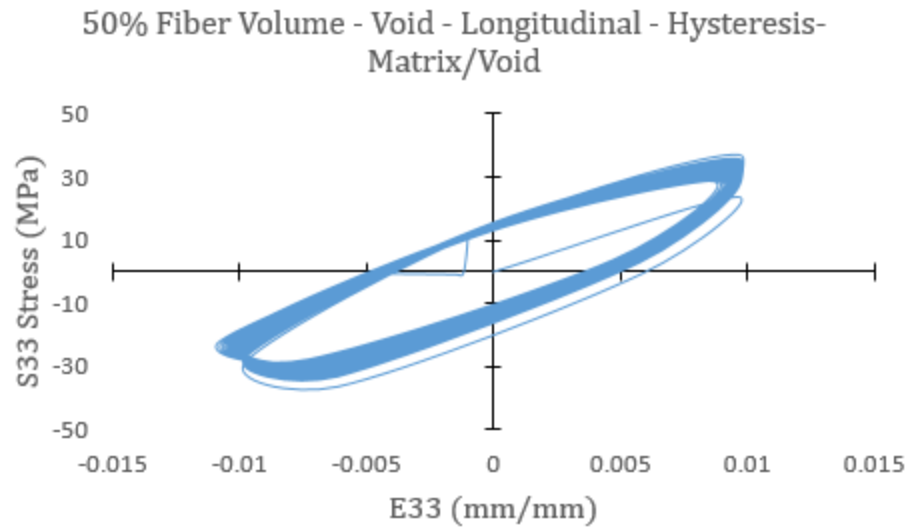


Figure A-45 50% Fiber Volume – Void Configuration – Longitudinal Loading – Hysteresis - Matrix/Void

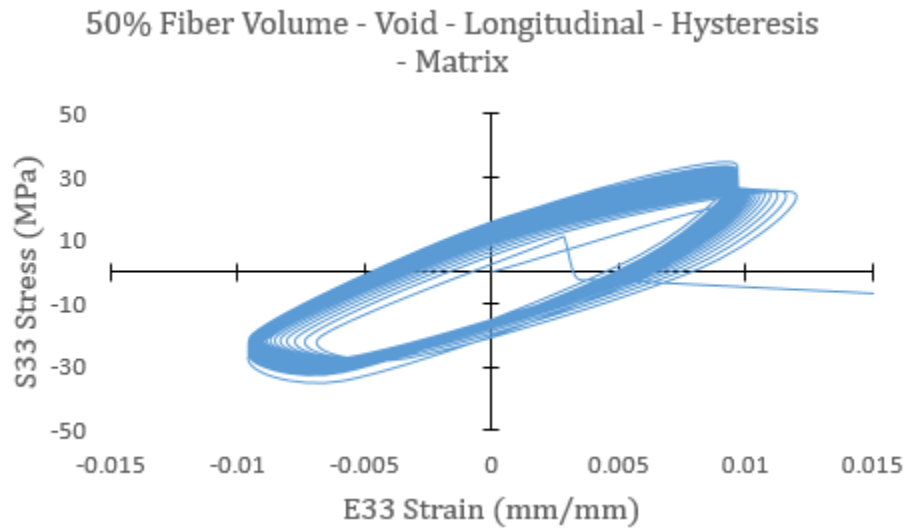


Figure A-46 50% Fiber Volume – Void Configuration – Longitudinal Loading – Hysteresis - Matrix

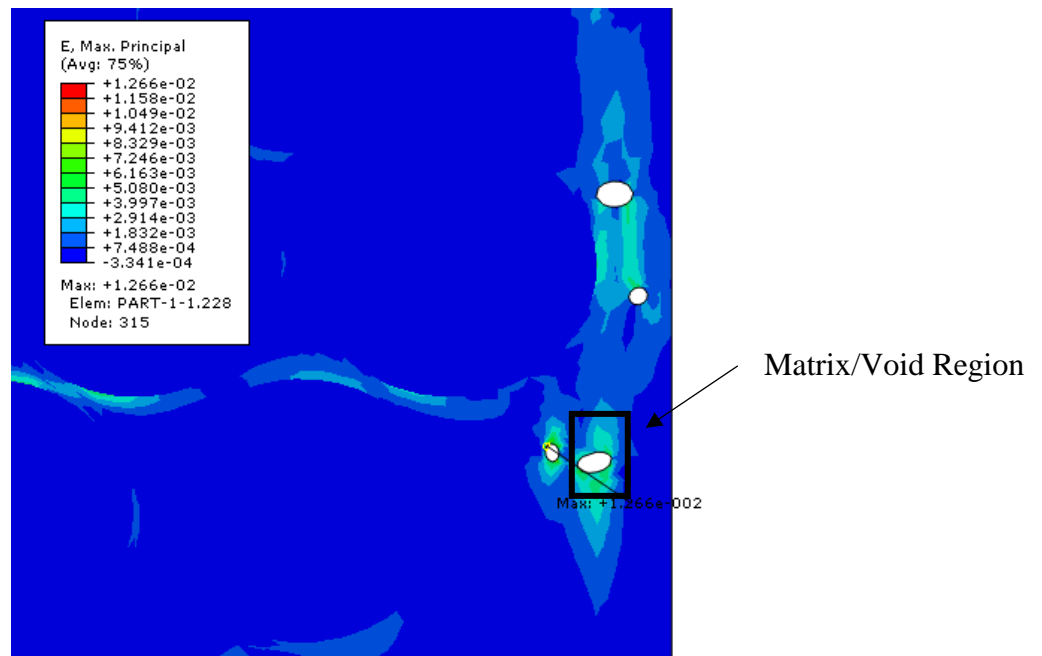


Figure A-47 60% Fiber Volume – Void Configuration – Longitudinal Loading – Max Principal Strain – Close-up – 11 minutes

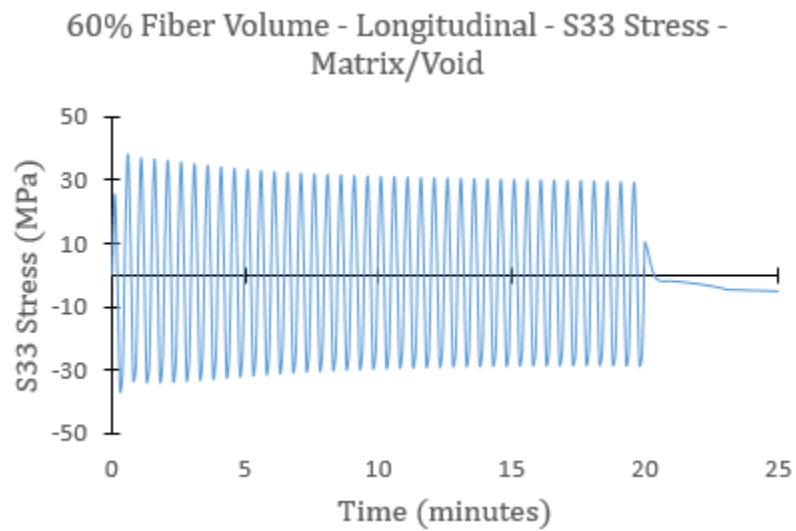


Figure A-48 60% Fiber Volume – Void – Longitudinal Loading – S33 Stress – Matrix/Void

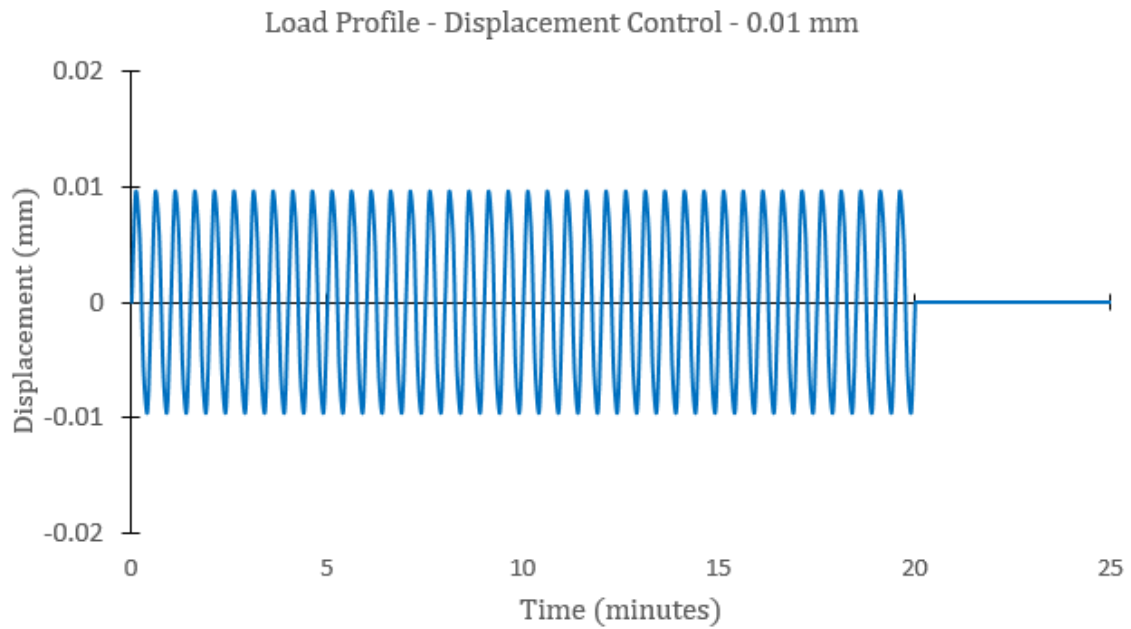


Figure A-49 Shear Loading – Load Profile

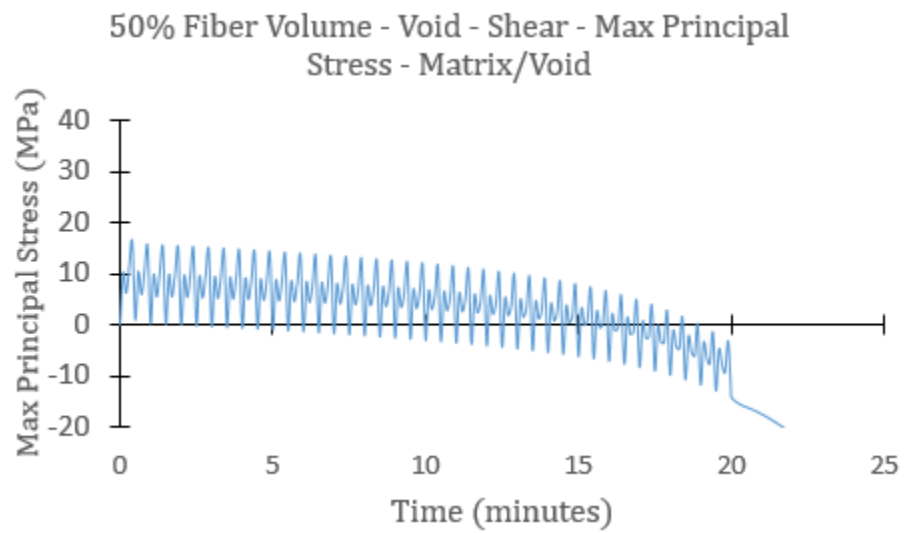


Figure A-50 50% Fiber Volume – Shear Loading – Void – Max Principal Stress – Matrix/Void

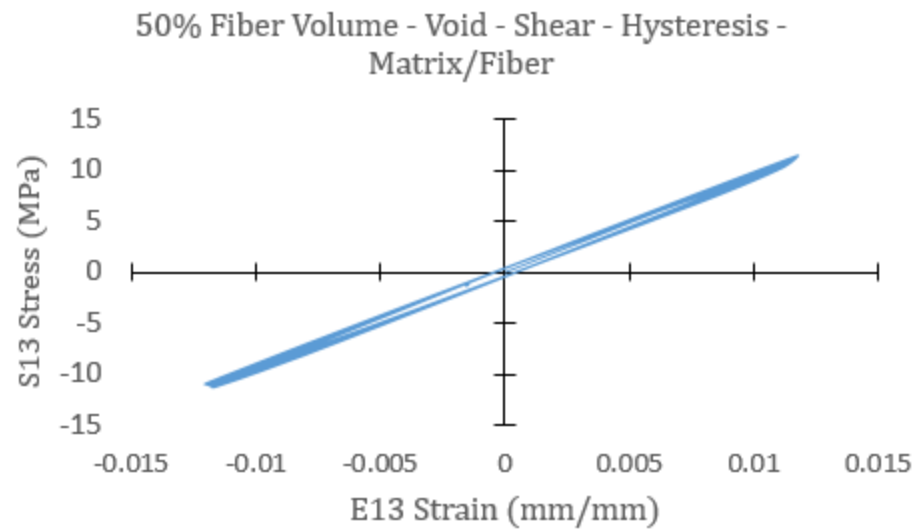


Figure A-51 50% Fiber Volume – Void –Shear Loading – Shear Hysteresis – Matrix/Fiber

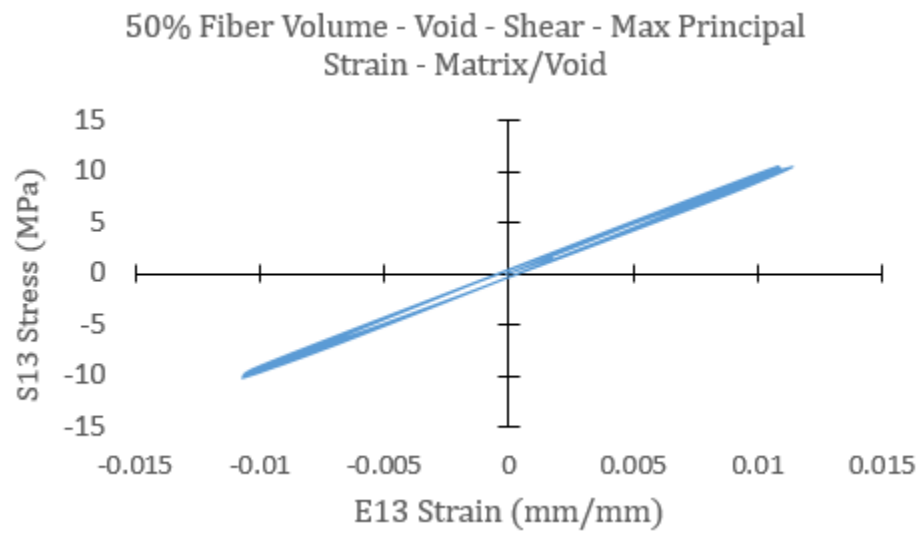


Figure A-52 50% Fiber Volume – Void –Shear Loading – Shear Hysteresis – Matrix/Void

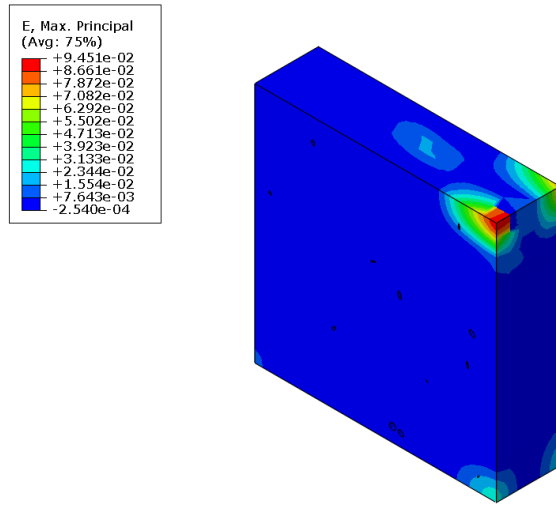


Figure A-53 – 40% Fiber Volume – Void – Shear – Principal Strain – 20 minutes

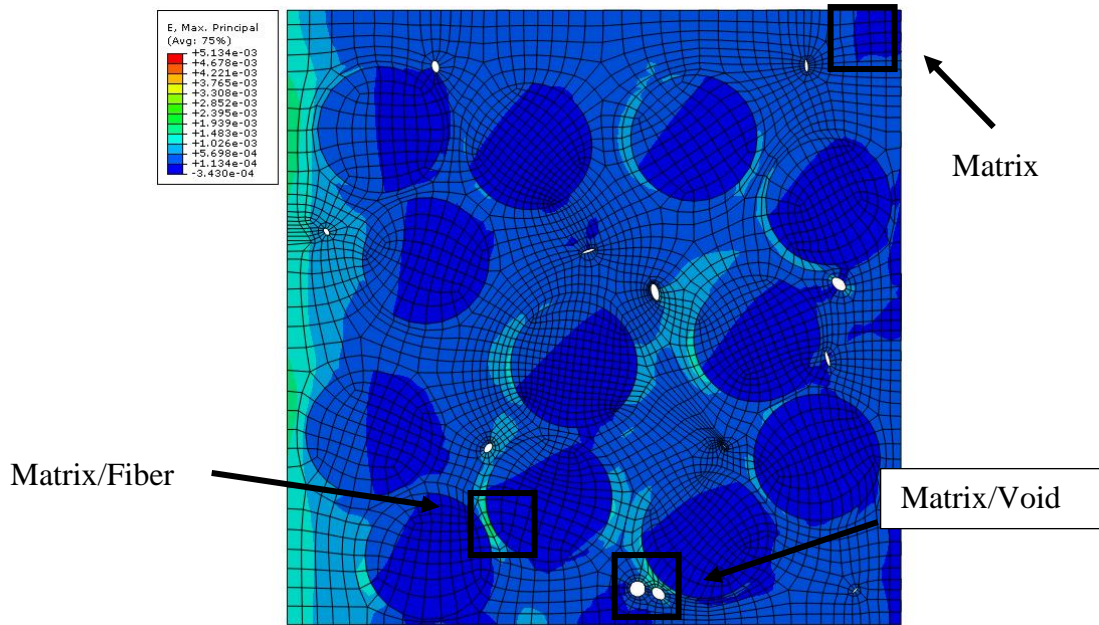


Figure A-54 – 40% Fiber Volume – Void – Shear Loading - Mesh

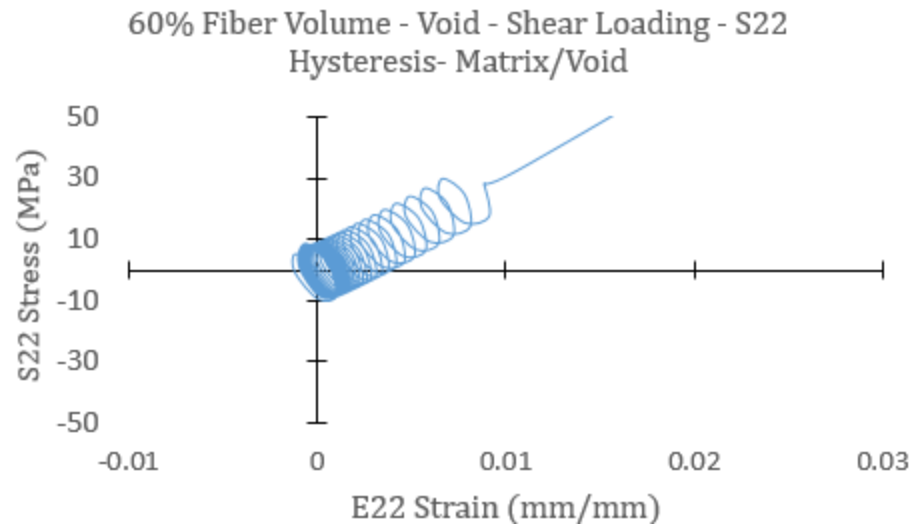


Figure A-55 – 60% Fiber Volume – Void –Shear Loading – S22 Hysteresis – Matrix/Void

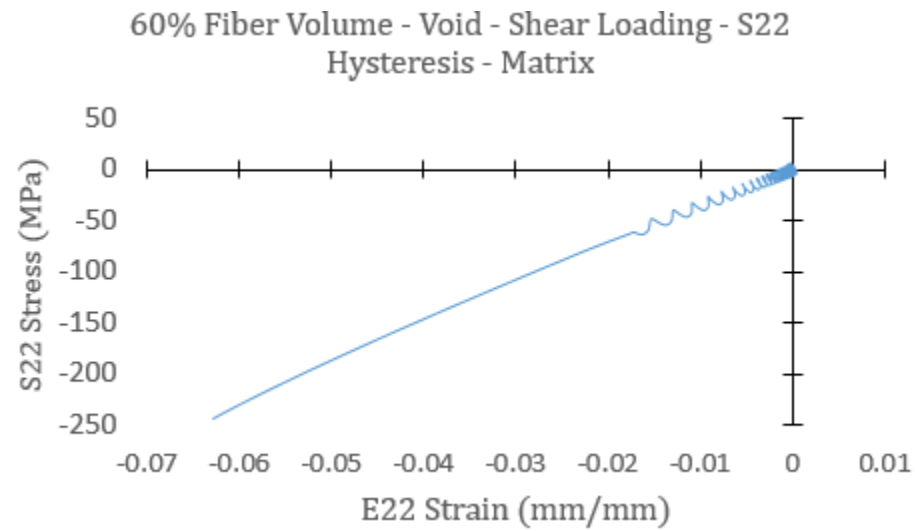


Figure A-56 – 60% Fiber Volume – Void –Shear Loading – S22 Hysteresis - Matrix

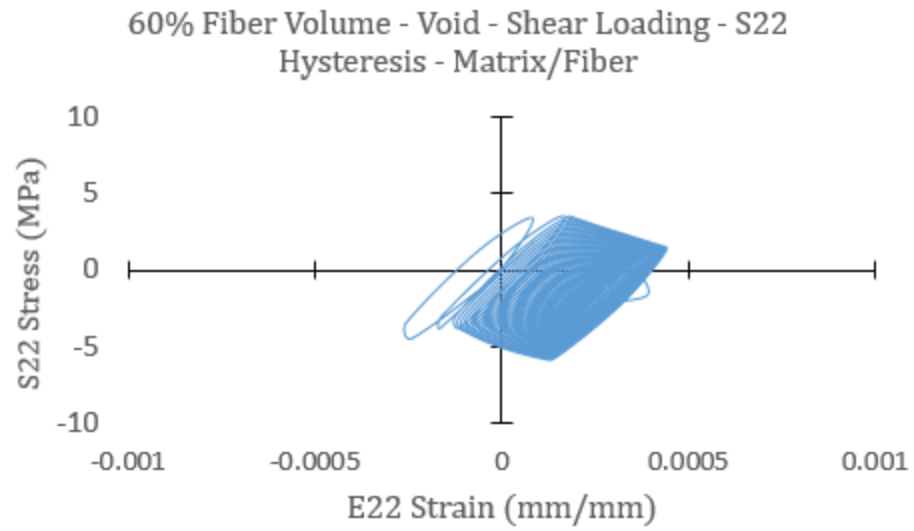


Figure A-57 – 40% Fiber Volume – Void –Shear Loading – S22 Hysteresis – Matrix/Fiber

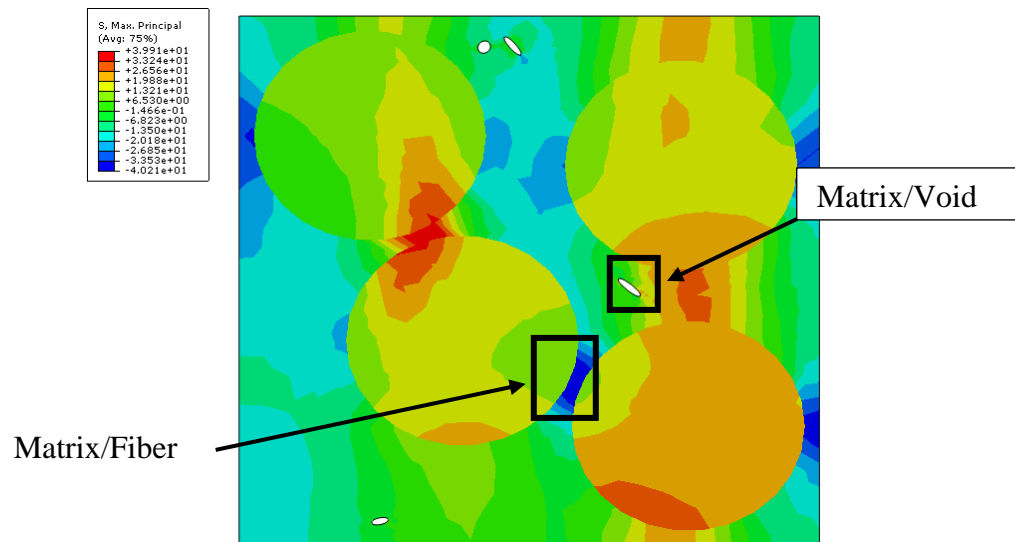


Figure A-58 – 50% Fiber Volume – Void –Transverse Loading – Regions of Interest

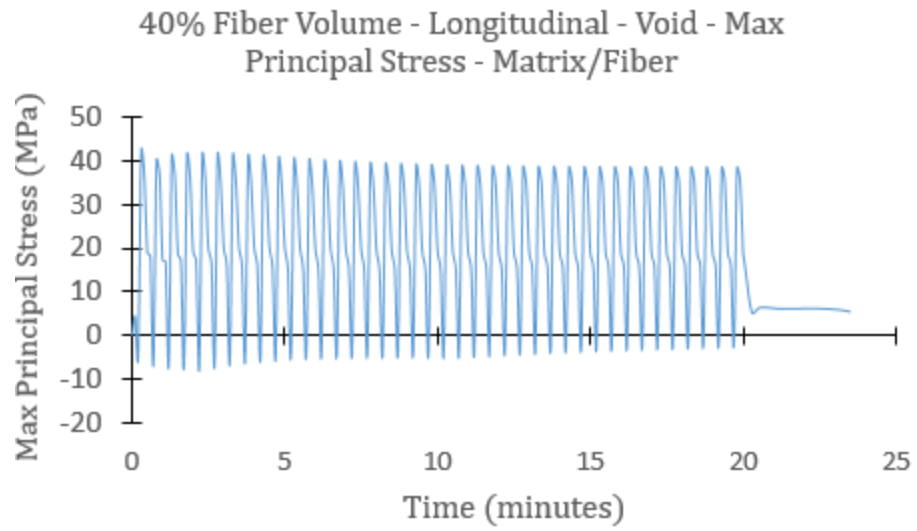


Figure A-59 – 40% Fiber Volume – Void – Longitudinal – Max Principal Stress – Matrix/Fiber

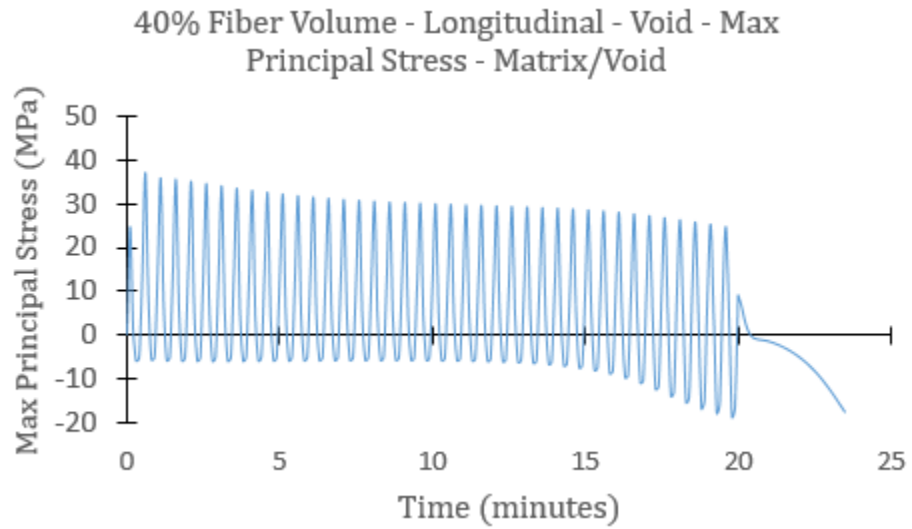


Figure A-60 – 40% Fiber Volume – Void – Longitudinal – Max Principal Stress – Matrix/Void

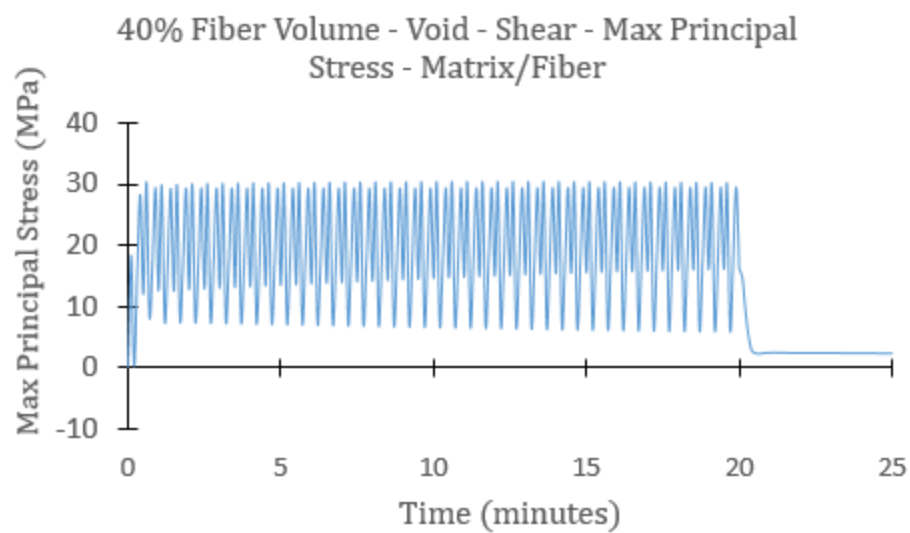


Figure A-61 – 40% Fiber Volume – Void – Shear – Max Principal Stress – Matrix/Fiber

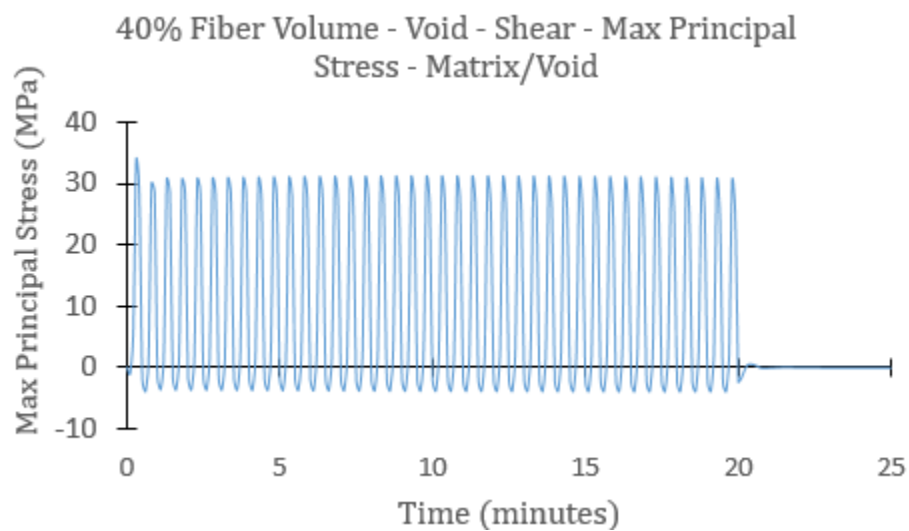


Figure A-62 – 40% Fiber Volume – Void – Shear – Max Principal Stress – Matrix/Void

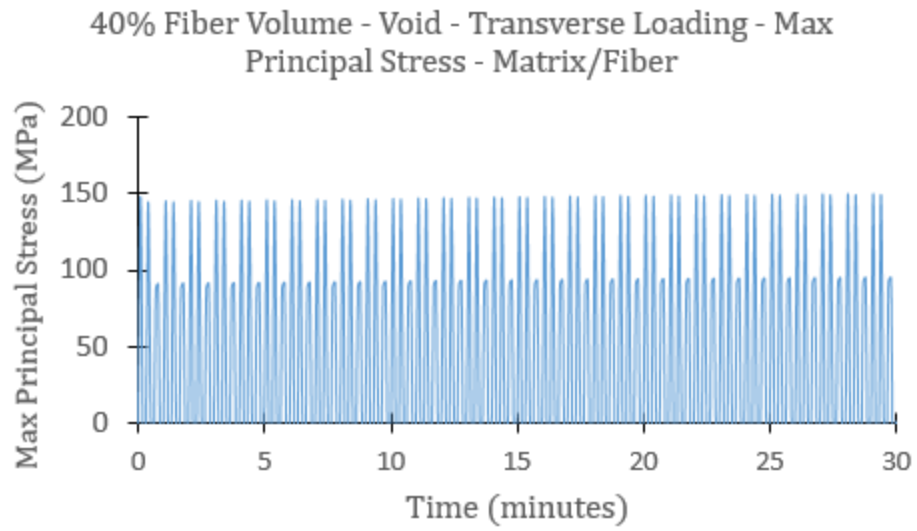


Figure A-63 – 40% Fiber Volume – Void – Transverse – Max Principal Stress – Matrix/Fiber

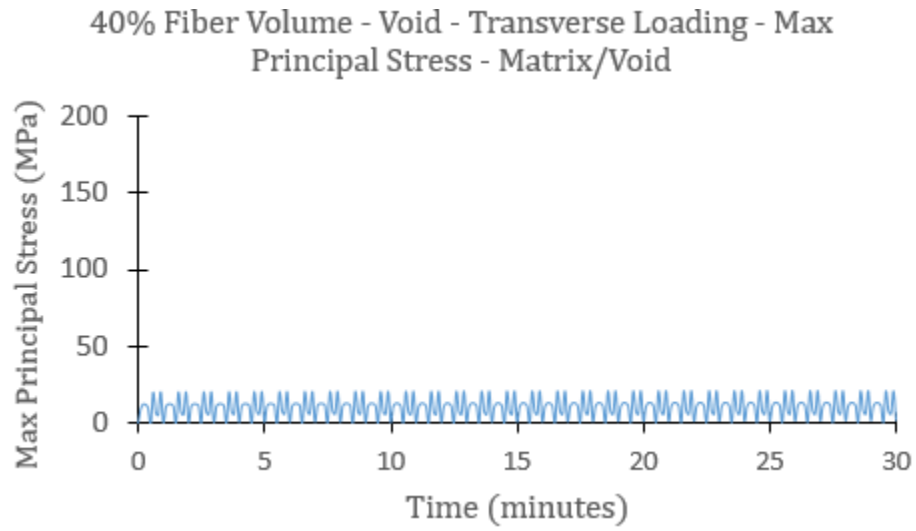


Figure A-64 – 40% Fiber Volume – Void – Transverse – Max Principal Stress – Matrix/Void

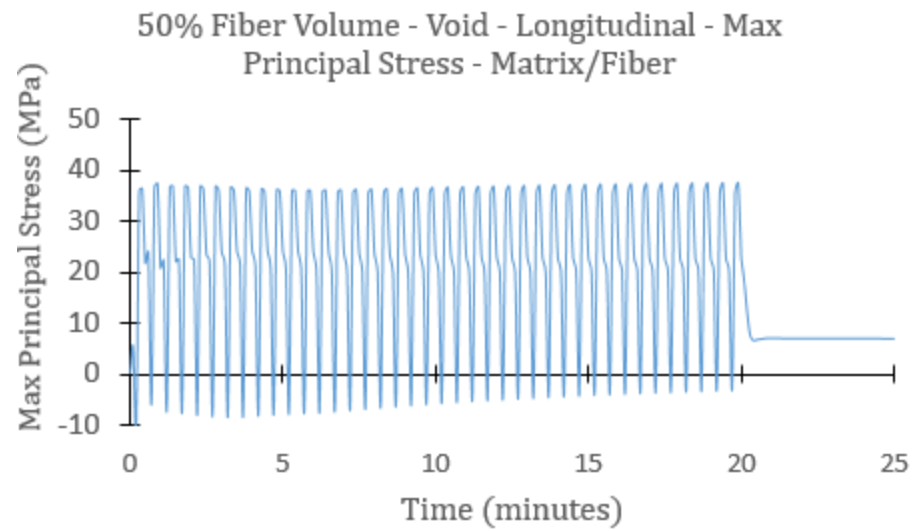


Figure A-65 – 50% Fiber Volume – Void – Longitudinal – Max Principal Stress – Matrix/Fiber

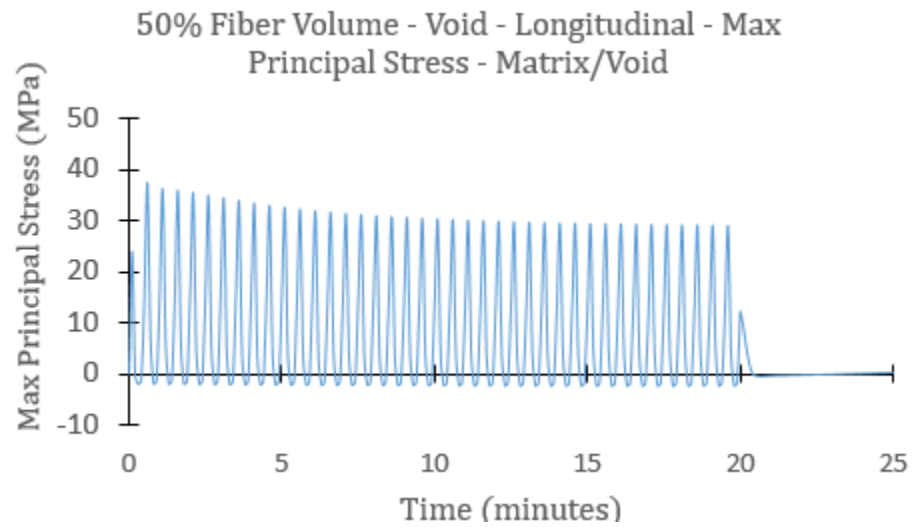


Figure A-66 – 50% Fiber Volume – Void – Longitudinal – Max Principal Stress – Matrix/Void

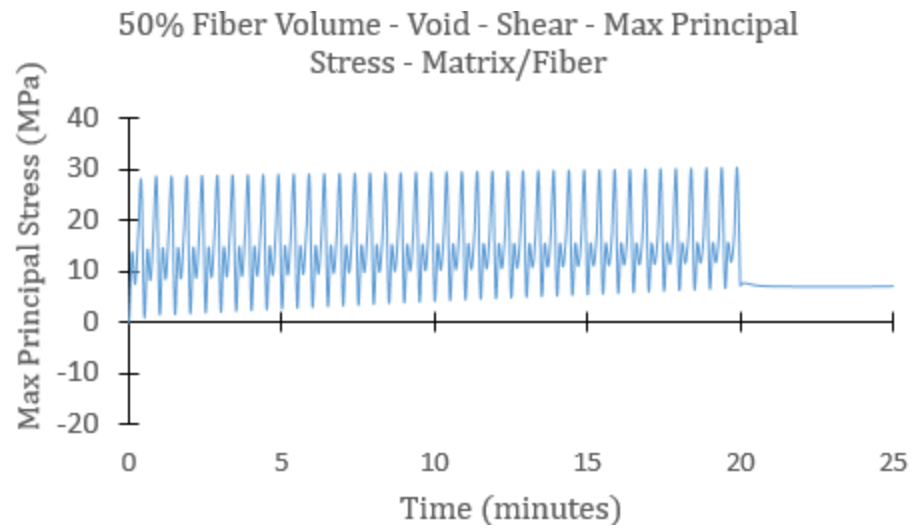


Figure A-67 – 50% Fiber Volume – Void – Shear – Max Principal Stress – Matrix/Fiber

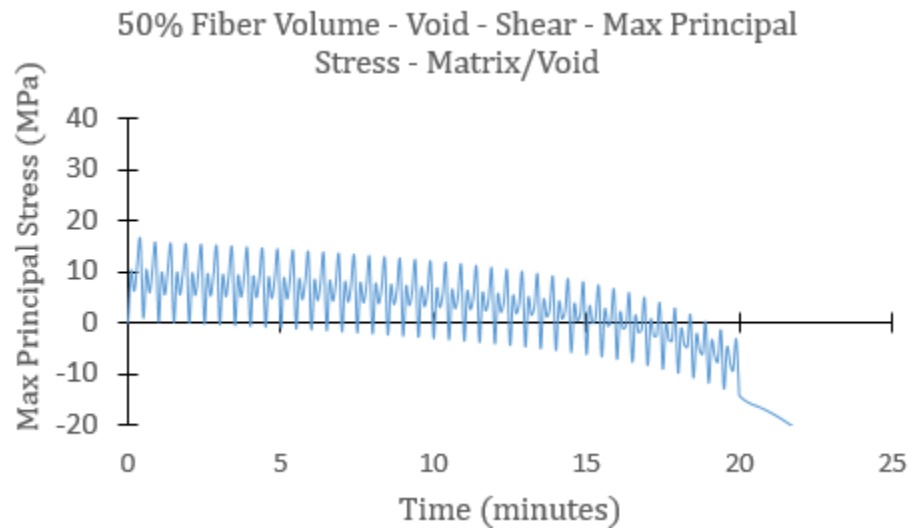


Figure A-68 – 50% Fiber Volume – Void – Shear – Max Principal Stress – Matrix/Void

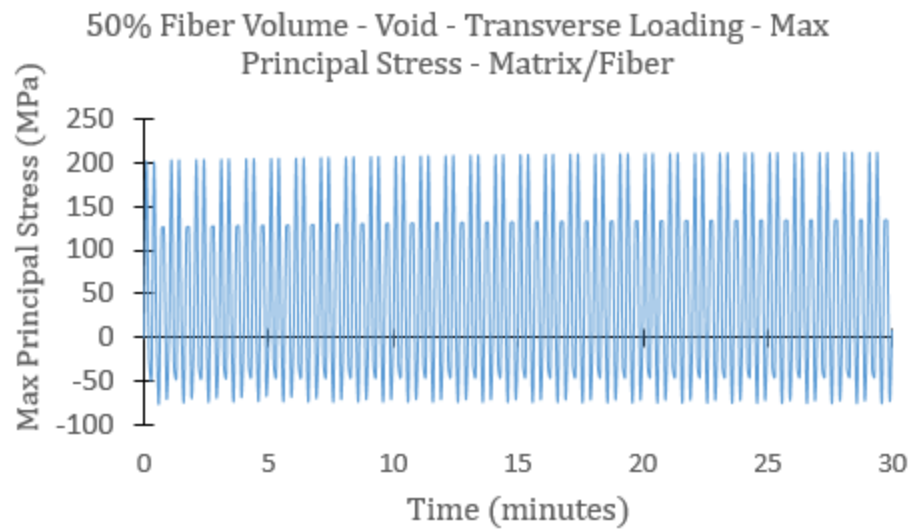


Figure A-69 – 50% Fiber Volume – Void – Transverse – Max Principal Stress – Matrix/Fiber

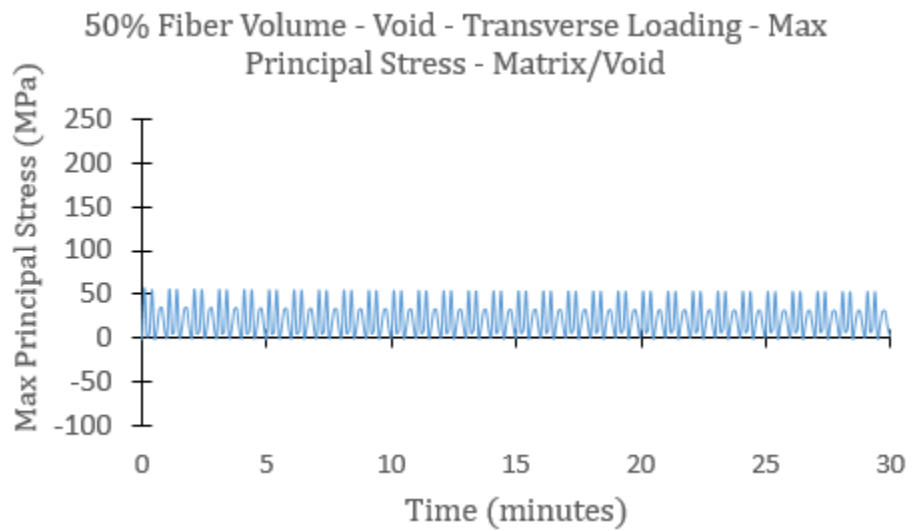


Figure A-70 – 50% Fiber Volume – Void – Transverse – Max Principal Stress – Matrix/Void

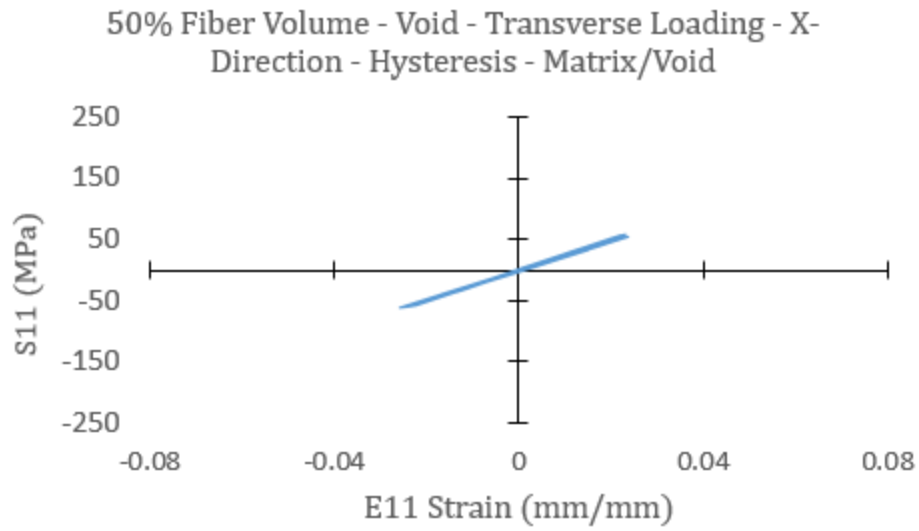


Figure A-71 – 50% Fiber Volume – Void –Transverse Loading – X-Direction Hysteresis – Matrix/Void

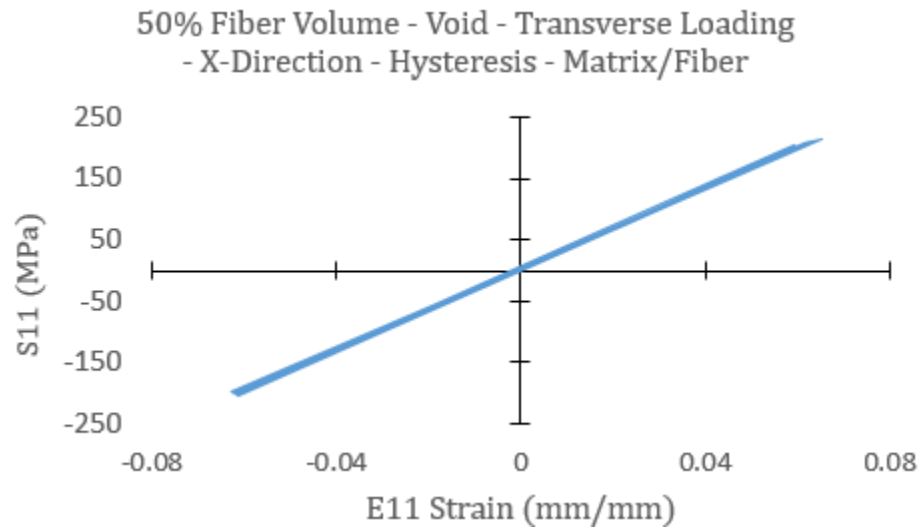


Figure A-72 – 50% Fiber Volume – Void –Transverse Loading – X-Direction Hysteresis – Matrix/Fiber

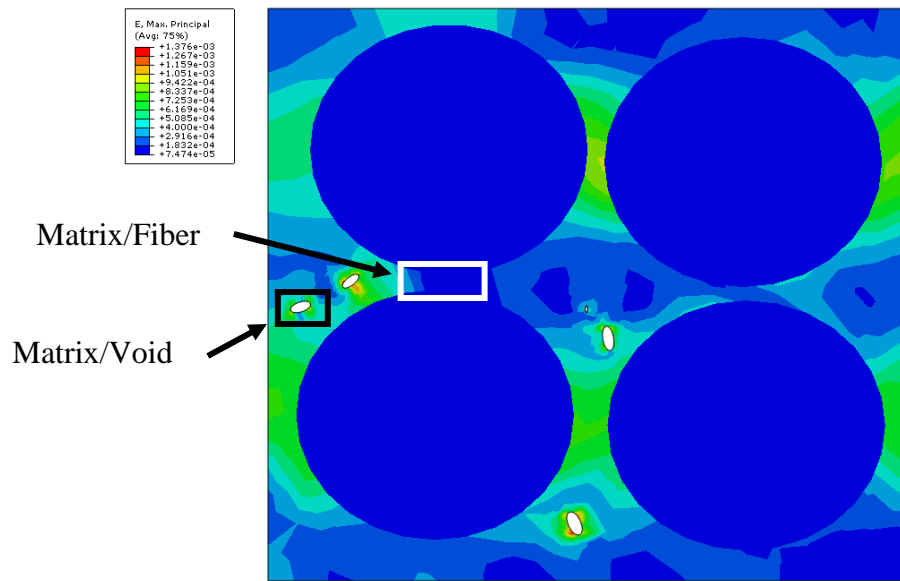


Figure A-73 – 60% Fiber Volume – Void – Transverse Loading – Regions of Interest

APPENDIX B

The appendix section summarizes the parametric study for a 60% fiber volume CFRC with a void placed between the fibers. Quasi-static loading in both transverse and shear direction is applied to the model and the effects of temperature and fiber spacing are studied. With regards to crack propagation and failure in viscoelastic materials, numerous researchers including Roy and Reddy [32] , Carpenter [33] and Yadagirz et al. [34] have predicted the viscoelastic behavior of bonded joints. Choupani [35] uses finite element models, stress intensity factors and energy release rate to characterize the fracture behavior of commonly used aerospace adhesives in bonded double-lap joints. Materials simulated include FM73. Panigrahi and Pradhan [36] also investigate the delamination damage and damage propagation in a single-lap laminated fiber reinforced composite. Needleman [37] and Tvergaard and Hutchinson [38] researched cohesive zone modeling to simulate crack propagation along a predefined interface. Tvergaard and Hutchinson assume that the adhesive layer is elastic-plastic and model the separation of the adhesive using a traction-separation law. Furthermore attention is given to the steady-state toughness of the crack and a parametric study is conducted. In addition Neto et al. [39] utilizes cohesive zone surfaces to model crack propagation for a brittle and a ductile adhesive. A linear traction-separation law is assumed to predict the onset of failure of single-lap composite joints. Neto et al. state that the linear-separation traction law models brittle adhesives well but underestimates the crack propagation resistance of a ductile adhesive. It is suggested that a trapezium traction separation behavior model is more appropriate to simulate the cohesive zone behavior of a ductile adhesive. Muliana and Khan [26] constructed Mode I (opening) time-dependent crack propagations in adhesive bonded joints by using bonded joint geometry provided by Allen and Searcy [40]. The parametric study expands on the work done by Muliana and Khan by using the same thermo-viscoelastic material model and the same material parameters. The goal of the parametric study is to investigate the temperature and fiber spacing effect on crack onset and propagation in a CFRC.

CONSTITUTIVE EQUATIONS

For Mode 1 crack propagation, the propagation can be broken into three separate processes:

1. Critical Opening Displacement
2. Release of Debonding Force
3. Propagation of Crack

Initially, cohesive surface modeling assumes that the Crack Opening Displacement (COD) has to reach a critical value before the crack begins to propagate. The crack opening distance ratio is given as

$$f = \frac{\delta_n^t}{\delta_{n,cr}} \quad (32)$$

where δ_n^t is the actual opening distance and $\delta_{n,cr}$ is the critical opening distance. f is always equal to 1. The crack opening distance ratio is determined experimentally through the following equation:

$$1 = f = \sqrt{\left(\frac{\langle t_n \rangle}{t_{cr}^n}\right)^2 + \left(\frac{\tau_s}{\tau_{cr}^s}\right)^2} \quad (33)$$

t_n is the normal stress and t_{cr}^n is the critical normal stress. τ_s is the shear stress and τ_{cr}^s is the critical shear stress. The Macaulay brackets $\langle \rangle$ indicate that compressive normal stress will not contribute to the mixed-mode stress failure initiation criterion. The COD failure criterion is only valid for 2D element formulations, therefore plane-strain conditions are assumed and plane strain element formulations used. From Muliana and Khan [26], the critical opening distance $\delta_{n,cr}$ is determined to be 0.0002 mm. Once the COD is reached, the crack begins to propagate. When debond occurs, the traction between the two crack surfaces are equal and opposite forces at the respective nodes. The forces or the debond forces have to reduce to zero once the nodes start to separate. For our purpose, we utilize a linear debond law which is shown below:

$$F_{debond,residual} = F_{initial} * \left(1 - \frac{t_{relative}}{0.015 \text{ min}}\right) \quad (34)$$

$F_{initial}$ is the initial debond force between the two nodes right when the crack tip begins to propagate. $t_{relative}$ is the time relative to the time at the start of crack propagation. Once the first node at the crack tip begins to debond and the debond force drops to zero, the process repeats until the entire crack path becomes debonded. Note that the linear debond law is not based on an analytical derivation but is an empirical relation. Figure B-1 shows the critical opening displacement diagram and highlights the critical crack opening displacement and labels initial nodes.

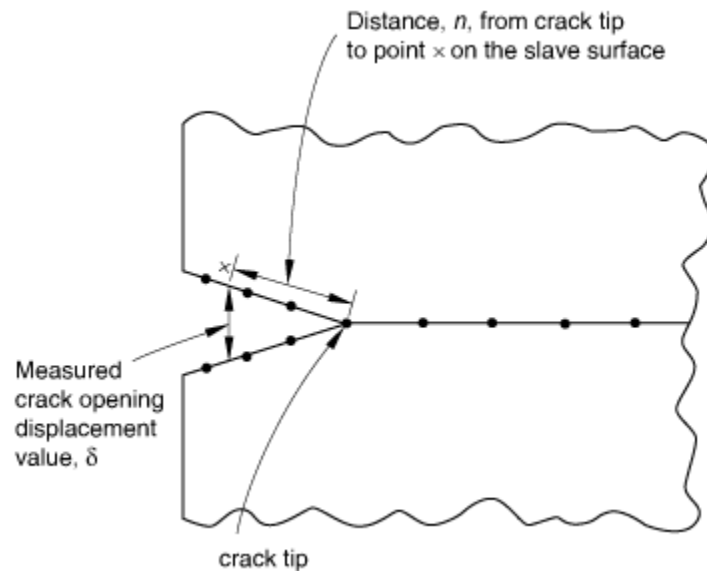


Figure B-1 – Critical Opening Displacement Diagram [41]

COHESIVE SURFACE MODELING

ABAQUS allows the use of cohesive elements, cohesive surfaces and Virtual Crack Closer Technique (VCCT). For all three types of fracture analysis, the damage initiation and damage propagation parameters have to be specified. For this analysis, we utilized cohesive surfaces to model the propagation of a predefined crack. A square plate model with 60% fiber content and containing two fibers is modeled. An ellipsoidal void is placed center of the square, at a 45° degrees with respect to the horizontal. The major axis of the void is 3% of the fiber radius (0.3909 mm) which corresponds to a major axis radius of

0.01172 mm. The minor radius of the ellipsoidal is 1% which corresponds to 0.003909 mm. Three different fiber spacing configurations are modeled to study the effect of fiber spacing on fracture propagation of a composite subjected to transverse loading. The configurations modeled are shown in Table B-1.

Table B-1 – Cohesive Element Model – Fiber Spacing

Fiber Spacing Percentage	Fiber Spacing Distance (mm)
3%	0.01173
10%	0.03909
20%	0.07818

Figure B-2 shows the cohesive element model with void oriented at 45° to the horizontal. Furthermore the coordinate system is also labeled. The fiber spacing distance is also labeled and is defined to be perpendicular to the direction of crack growth propagation. Utilizing the critical opening displacement (COD) fracture criterion requires us to predefine a fracture path. A notch was cut into the matrix material and the notch region is meshed to capture the crack opening. Figure B-3 shows the two possible fracture paths. Each fracture path has a predetermined notch cut into the polymer matrix. The fracture surfaces are initially bonded to the polymer matrix. Once the node displaces and exceeds the COD, the crack will begin to propagate. The model utilizes 4-noded, fully-integrated, plane-strain elements (CPE4).

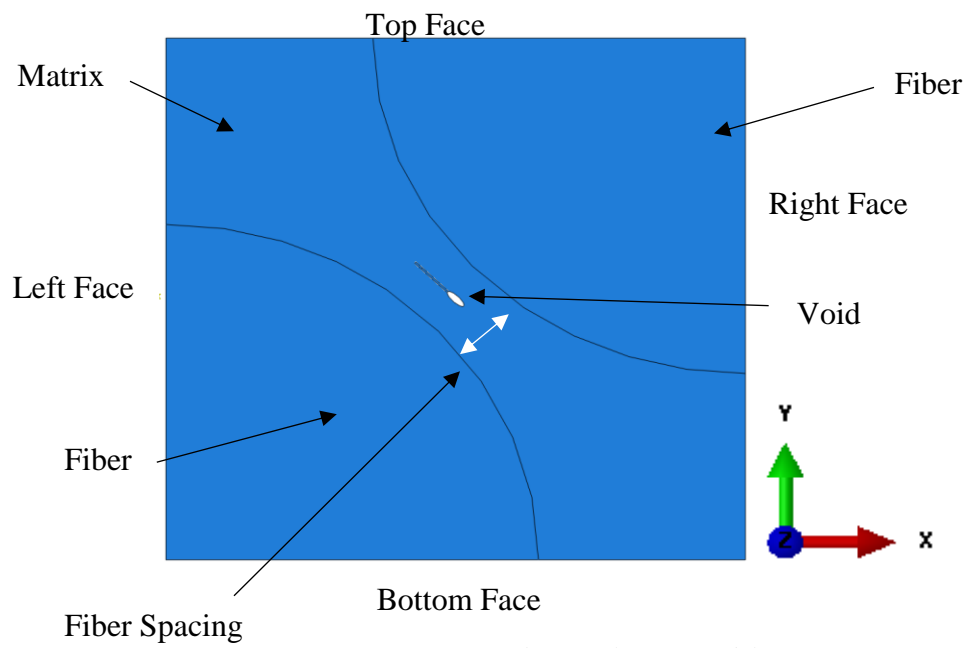


Figure B-2 – Cohesive Element Model

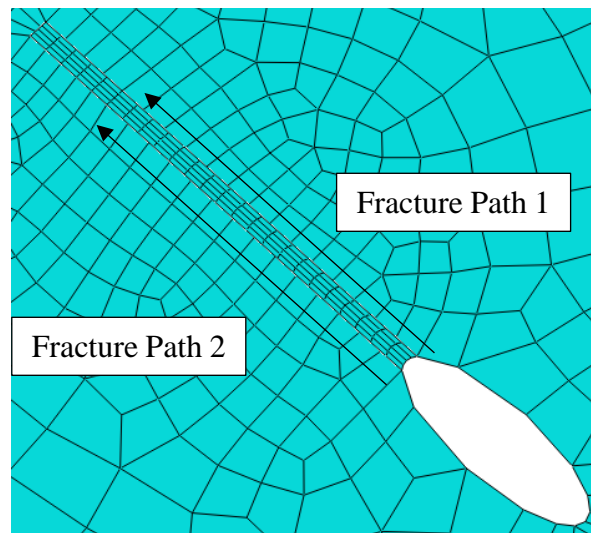


Figure B-3 – Fracture Path

COHESIVE SURFACE FRACTURE PARAMETERS

The Critical Crack Opening displacement requires two parameters to establish the debonding parameters. The initial crack length is defined as the notch cut into otherwise pristine composite. Table B-2 contains the critical crack opening parameters.

Table B-2 – Critical Crack Opening Parameters

Fracture Parameter	Parameter
Critical Crack Opening $\delta_{n,cr}$	4.16×10^{-4} mm
Initial Crack Length	2.035×10^{-3} mm

COHESIVE FRACTURE LOAD CASE

The cohesive fracture models are 2D finite element simulations and thus do not have a 3-direction or z-direction. Two load cases are considered: Transverse loading and simple shear loading. For transverse loading, a uniform traction load of 50 MPa is applied on the left face of the model. The traction vector for transverse loading is given as

$$\vec{t} = \langle -50, 0, 0 \rangle \quad (35)$$

Furthermore, equations are used so the nodes on the left face displace uniformly along the x-direction. Also, the bottom face nodes of the cohesive element model are restrained to move uniformly in the y-direction. Assuming the width of the plate is given by w and the height of the plate is given by h , the boundary conditions are expressed as

$$\begin{aligned} u_1(w, x_2, t) &= 0; 0 \leq x_2 \leq h \\ u_2(x_1, h, t) &= 0; 0 \leq x_1 \leq l \end{aligned} \quad (36)$$

For the simple shear load cases, the traction load is 50 MPa, applied on the left face of the plate model along the negative y-direction. The traction vector for simple shear loading is given as

$$\vec{t} = \langle 0, -50, 0 \rangle \quad (37)$$

Furthermore, the equations are modified to force the left face nodes to displace uniformly in the y-direction. The bottom face nodes of the cohesive element are unrestrained. In

addition the boundary conditions are changed to allow for simple shear deformation. The boundary conditions for the simple shear loading is given as

$$\begin{aligned} u_1(w, x_2, t) &= 0; 0 \leq x_2 \leq h \\ u_2(w, x_2, t) &= 0; 0 \leq x_2 \leq h \end{aligned} \quad (38)$$

The load period is 1 minute and a linear load rate is specified which means that the load rate is 50 MPa/min. Each fiber spacing configuration is run at three different initial temperature conditions: 303 Kelvin, 320 Kelvin and 330 Kelvin. There are 9 load cases total for each load direction for a total of 18 load cases. In contrast to the 3D finite element models, which uses thermos-mechanical element formulations, the plane strain models do not allow for heat conduction. The heat flux throughout the model is described through

$$\frac{\partial T(x_1, x_2, t)}{\partial x_1} = \frac{\partial T(x_1, x_2, t)}{\partial x_2} = 0; 0 \leq x_1 \leq w, 0 \leq x_2 \leq h, t \geq 0 \quad (39)$$

COHESIVE SURFACE MODELING RESULTS

An initial crack path is defined at the edge of the ellipsoidal void and each model is subjected to a linearly ramping creep load of 50 MPa along the fibers transverse direction. The load rate is 0.83 MPa/s. The load increment per step applied is 0.001 and plane strain elements are used. Nine total configurations are modeled, ranging from 7.5% fiber spacing to 20% fiber spacing. The temperature ranges are 303 Kelvin, 320 Kelvin and 330 Kelvin. The crack is defined to propagate, once the first node in contact becomes detached and the element surface becomes traction-free. Table B-3 summarizes the crack propagation load and the maximum in-plane principal strain at crack initiation.

Table B-3 – Crack Initiation Load – Principal Strain – Transverse Loading

	Crack Initiation Load (MPa)		
Temperature (Kelvin)	7.5 % Fiber Spacing	10% Fiber Spacing	20 % Fiber Spacing
303	18.00	20.01	26.00
320	16.00	17.00	23.49
330	15.00	16.50	22.49
	Max In-Plane Principal Strain (%) at Crack Initiation		
303	8.56	8.26	9.29
320	8.53	8.54	8.13
330	8.53	8.56	8.09

The table reflects that the fiber spacing and temperature have a significant effect on the onset of crack propagation. For transverse loading, the 7.5 % spacing has the lowest crack propagation load while the 20% fiber spacing has the highest crack propagation load for the same temperature band. Furthermore, increasing the temperature in the individual models reduced the crack propagation load as well. The in-plane principal strain at crack initiation varies between 8.09% and 9.29%. Figure B-4 shows the crack propagation stress versus fiber spacing. The crack propagation stress is plotted on isothermal curves which

are 303 Kelvin, 320 Kelvin and 330 Kelvin respectively. The greatest changes in crack propagation stress occur in the 10% fiber spacing sample. When the temperature is increased from 303 K to 320 K, the crack propagation stress reduces from 20.01 MPa to 17.00 MPa which is a 15% reduction in capability. Similarly, the 7.5 % and 20 % sample lose 11.11% and 9.65% in crack propagation resistance respectively.

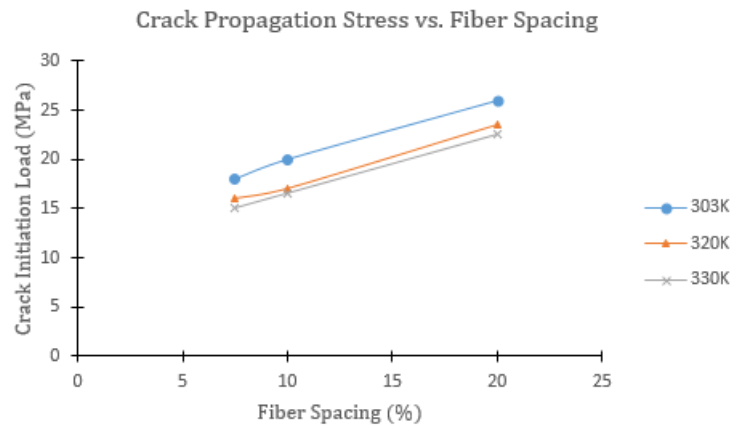


Figure B-4 – Crack Propagation Stress vs. Fiber Spacing

Comparing the results to the work done by A. Muliana and K. Khan [29], elevating the temperature reduces the crack propagation load and therefore agrees well with A. Muliana and K. Khan's simulation findings. For their case, an adhesive bonded joint, consisting of two aluminum plates and adhesive is subjected to Mode I loading. The corresponding failure load was 5 MPa which corresponds to approximately 200 N. Figure B-5 is the initial crack path in the void area. The contour plot is the max in-plane principal stress. Stress concentrations at the crack edge are apparent, however, the crack edge has not reached the critical opening displacement to propagate the crack.

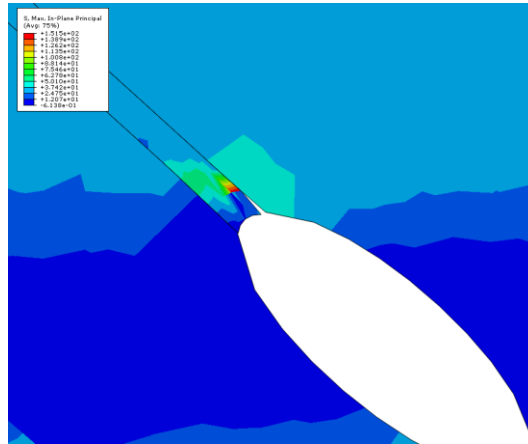


Figure B-5 – Initial Crack Path

Figure B-6 is the 7.5% fiber spacing crack length versus time for the 7.5 %. Figure B-7 and Figure B-8 are the crack length versus time plots for both 10% and 20% fiber spacing. For 303 Kelvin initial temperature, the initial crack propagation time is 20.4 seconds for the 7.5% fiber spacing and 21.6 seconds for the 10% fiber spacing. The 20% fiber spacing, 303 Kelvin, crack propagates at 31.8 seconds. Within the same fiber spacing configuration, increasing the initial temperature increases the rate of crack propagation. The 7.5%, 303 Kelvin configuration debonds fully at 47.4 seconds. At 330 Kelvin, the crack fully opens at 37.2 seconds.

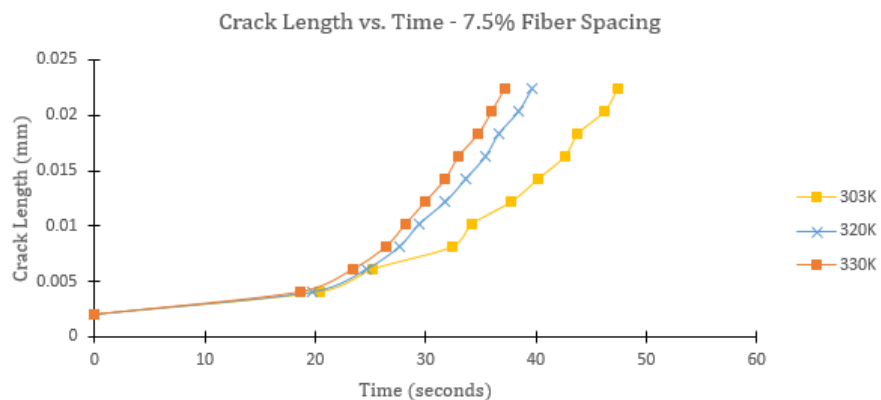


Figure B-6 – 7.5 Fiber Spacing – Crack Length

The 20% fiber spacing has the slowest crack propagation rate from all modeled configurations. At 303 K, the crack begins to propagate at 31.8 seconds. At 320 K, the crack initiation occurs at 28.8 seconds and at 330 K, the crack opens at 27.6 seconds.

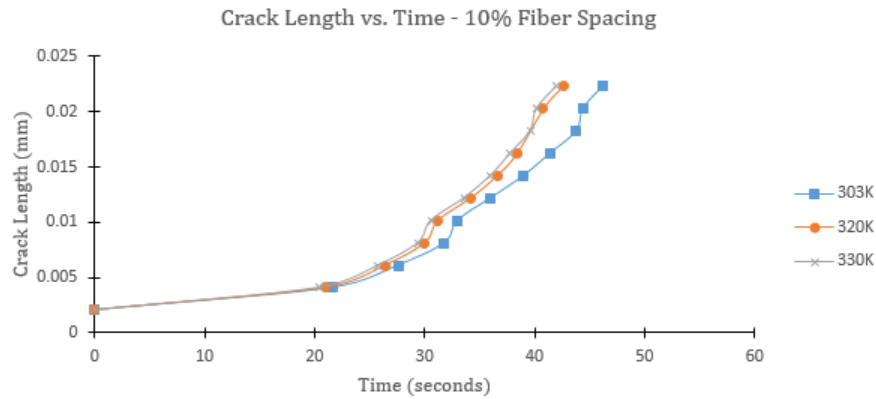


Figure B-7 – 10% Fiber Spacing – Crack Length

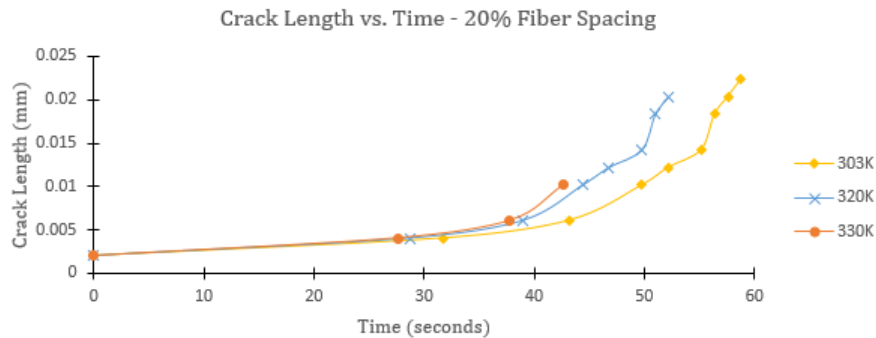


Figure B-8 – 20% Fiber Spacing – Crack Length

In addition to transverse loading of the fiber samples, the samples are also shear loaded. The shear load is 50 MPa and the linear load rate is 0.83 MPa/seconds. Three fiber spacing with three different temperature configurations are simulated. The compliance behavior for an orthotropic material is different than the compliance of an isotropic material. In simple shear for an isotropic material and with rectangular geometry, the material's edges remain parallel when loaded in shear. However, for an orthotropic

material, the polymer matrix is more compliant than the fiber and deforms more. Applying a shear traction load on the left face of the model, one can observe that the polymer matrix is compressed near the matrix/fiber interface. Figure B-9 shows the max in-plane principal strain of a 7.5% at 0.28 minutes. Visible are the strain risers in the polymer matrix in-between the fibers and the edges of the material which are no longer parallel to their opposing edges.

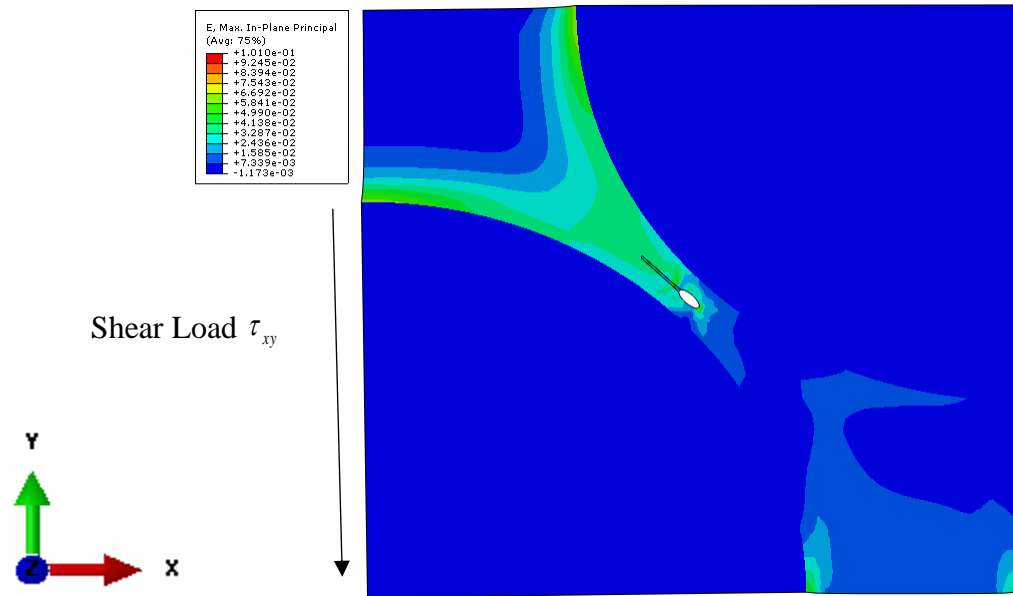


Figure B-9 – 7.5% Fiber Spacing – Max In-Plane Strain – 0.28 min

For the samples loaded in shear, both crack initiation load and crack propagation speed recorded. The crack initiation load is defined as the instantaneous shear load acting on the model as the first node of the finite element model detaches. Table B-4 summarizes the crack initiation and the maximum in-plane principal strains at the void edge at crack initiation. The crack initiation loads for shear loading vary between 7.75 MPa to 10.75 MPa. Max In-Plane Principal Strains vary between 8.24% and 10.37% for the individual finite element models.

Table B-4 – Crack Initiation Load – Principal Strain – Shear Loading

	Crack Initiation Load (MPa)		
Temperature (Kelvin)	7.5 % Fiber Spacing	10% Fiber Spacing	20 % Fiber Spacing
303	10.75	9.50	8.00
320	9.50	9.25	7.75
330	9.00	9.25	7.75
	Max In-Plane Principal Strain (%) at Crack Initiation		
303	10.00	9.03	9.29
320	10.37	10.26	8.99
330	10.03	10.24	8.24

Comparing the shear response of the finite element models to their transverse response, the crack initiation loads are lower for the shear response. A 7.5% fiber spacing model, at 303 K, loaded transversely has a crack initiation load of 18 MPa. Loaded in shear, the 7.5% fiber spacing model has a crack initiation load of 10.75 MPa. However, the maximum in-plane principal strains are comparable across the two load configurations. Figure B-10 plots the crack initiation load as a function of fiber spacing. For transverse loaded models, the crack initiation increased with increasing fiber distance. This could be attributed to a reduction in stress concentration because the fibers are spaced farther apart. However, for the shear loaded models, the crack initiation load decreases with increasing fiber spacing. For example, at 303 Kelvin and 50 MPa shear loading, the crack initiation decreases from 10.75 MPa to 9.5 MPa when the fiber spacing is increased from 7.5% to 10% fiber spacing. Also, when the fiber spacing is increased from 10% to 20%, the crack initiation load reduces from 9.5 MPa to 8 MPa.

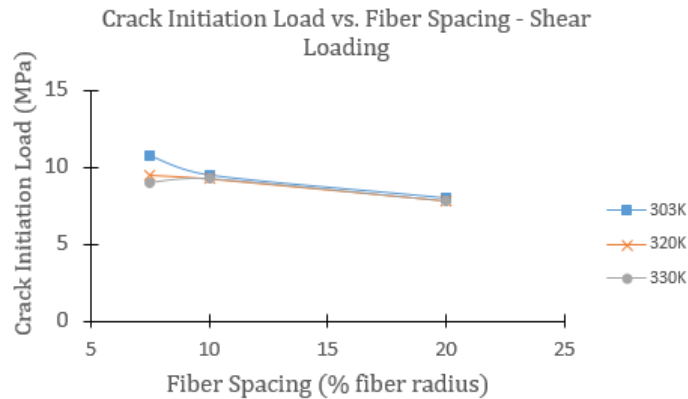


Figure B-10 – Crack Initiation Load vs. Fiber Spacing – Shear Loading

Figure B-10 also shows that the shear results, compared to the transverse loaded samples, are less sensitive to temperature changes. For example, at 10% fiber spacing, the crack initiation load changes from 9.5 MPa to 9.25 MPa when the temperature is raised from 303 Kelvin to 320 Kelvin. The change in crack initiation load is -2.63%. In contrast, the crack initiation load for a transverse loaded sample reduces by 15% when the temperature is increased from 303 Kelvin to 320 Kelvin.

Within the same fiber spacing, increasing the temperature increases the crack propagation rate. Figure B-11 are the graphs of crack length vs. time for the shear loaded samples. The 7.5% fiber spacing sample (shown in Figure B-11 a) is most sensitive to temperature changes. The temperature sensitivity decreases as the fiber spacing is increased. In fact, the 20% fiber spacing sample is minimal: Increasing the temperature from 320 K to 330 K does not produce a noteworthy increase in crack propagation rate.

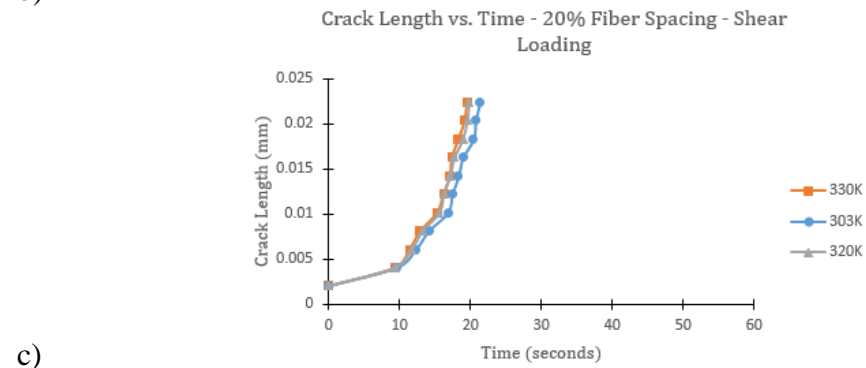
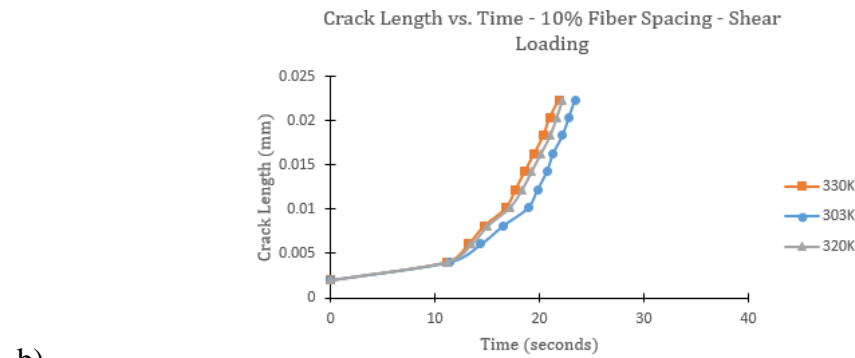
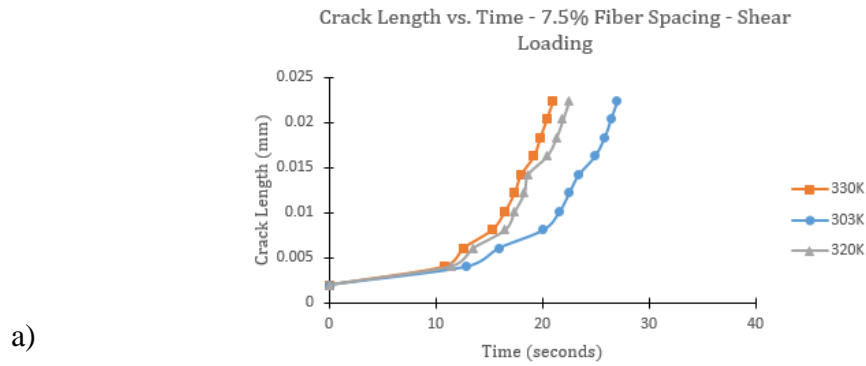


Figure B-11 – Crack Length vs. Time - Shear Loading - a) 7.5% b) 10% c) 20%

Using the cohesive surface element model proves that fiber spacing has a significant effect on the onset of crack propagation when the plane-strain model is loaded in the transverse direction. When the fiber spacing is reduced, the crack initiation load is lower and the crack propagates faster. In contrast, the shear loaded sample shows that when the fiber spacing is increased, the initial crack initiation load is lower. However, increasing the initial temperatures for all plane strain model leads to an initial lower crack

propagation load. Maligno et al. [19] varied fiber spacing within a 3D finite element model and loaded the model in both longitudinal and transverse direction. Although they used a different fiber/epoxy system, they predicted that the polymer matrix, undergoing transverse loading, would begin to fail at approximately 7% strain. The location of damage onset is predicted to be the matrix/fiber interface. Their constitutive model did not consider temperature effects.